

UC San Diego

UC San Diego Electronic Theses and Dissertations

Title

Applications of Mathematical Physics to Quantitative Biology

Permalink

<https://escholarship.org/uc/item/0bh201w4>

Author

Tyree, Timothy John

Publication Date

2023

Supplemental Material

<https://escholarship.org/uc/item/0bh201w4#supplemental>

Peer reviewed|Thesis/dissertation

UNIVERSITY OF CALIFORNIA SAN DIEGO

Applications of Mathematical Physics to Quantitative Biology

A dissertation submitted in partial satisfaction of the
requirements for the degree Doctor of Philosophy

in

Physics with a Specialization in Quantitative Biology

by

Timothy John Tyree

Committee in charge:

Wouter-Jan Rappel, Chair
Kevin King
Cory Miller
Oleg Shpyrko
Kechen Zhang

2023

Copyright

Timothy John Tyree, 2023

All rights reserved.

The Dissertation of Timothy John Tyree is approved, and it is acceptable in quality and form for publication on microfilm and electronically.

University of California San Diego

2023

DEDICATION

This doctoral dissertation is dedicated to my parents,
Robert and Mary Tyree.
Your words of encouragement and push for tenacity ring in my ears.
Your guidance and belief in my abilities
have been the driving force behind my pursuit of knowledge and
the completion of this important milestone.
This dissertation stands as a tribute to the values you have
instilled in me—the value of hard work,
the pursuit of knowledge,
and the importance
of family.
Thank
you.

TABLE OF CONTENTS

Dissertation Approval Page	iii
Dedication	iv
Table of Contents	v
List of Supplemental Files	vi
List of Figures	vii
List of Tables	x
Acknowledgements	xi
Vita	xii
Abstract of the Dissertation	xiv
Introduction	1
Chapter 1 Cell dispersal by localized degradation of a chemoattractant	10
1.1 Supplementary Information	37
Chapter 2 Annihilation dynamics during spiral defect chaos revealed by particle models	50
2.1 Supplementary Information	63
Chapter 3 Cross-modal representation of identity in primate hippocampus	80
3.1 Supplementary Information	95
Bibliography	134

LIST OF SUPPLEMENTAL FILES

1. tyree_S1.mov
2. tyree_S2.mov
3. tyree_S3.mov
4. tyree_S4.mov
5. tyree_S5.mov
6. tyree_S6.mov
7. tyree_S7.mov
8. tyree_S8.mov
9. tyree_S9.mov

LIST OF FIGURES

Figure 1.	“Life cycle of the social amoeba.”	3
Figure 2.	“Flow diagram of the human heart.”	5
Figure 3.	“Flow diagram of the primate hippocampus.”	9
Figure 1.1.	“Dispersal of cells.”	17
Figure 1.2.	“Attractant signaling of dispersing cell aggregates.”	19
Figure 1.3.	“Cell dispersal model.”	22
Figure 1.4.	“Predictions of chemical intervention.”	24
Figure 1.5.	“Effect of chemical intervention.”	29
Figure 1.6.	“Effect of chemical intervention (cont’d).”	31
Figure 1.7.	“Shape of attractant pulse.”	45
Figure 1.8.	“Dispersing cell aggregate.”	46
Figure 1.9.	“Correlation of collective cell motion and fluorescent intensity.”	47
Figure 1.10.	“Dispersing cell aggregate is source of correlation.”	48
Figure 1.11.	“Snapshot of model simulation.”	48
Figure 1.12.	“Dispersal phase diagrams.”	49
Figure 1.13.	“Minimum background attractant.”	49
Figure 2.1.	“Spiral tip properties.”	53
Figure 2.2.	“Pair-annihilation dynamics.”	54
Figure 2.3.	“Pair-annihilation power laws.”	58
Figure 2.4.	“Termination statistics”	60
Figure 2.5.	“Snapshots of spiral tip annihilation.”	68
Figure 2.6.	“Timescales are exponential.”	72
Figure 2.7.	“Forces are insensitive to domain size.”	73

Figure 2.8.	“Reaction scale of the linear particle model”	75
Figure 3.1.	“Identity neurons in primate hippocampus”	82
Figure 3.2.	“Identity neurons in primate hippocampus (cont’d)”	83
Figure 3.3.	“Single neurons in hippocampus represent multiple individuals.”	85
Figure 3.4.	“Single neurons in hippocampus represent multiple individuals (cont’d).”	87
Figure 3.5.	“Cross-modal encoding of identity.”	88
Figure 3.6.	“Cross-modal encoding of identity (cont’d).”	89
Figure 3.7.	“Cross-modal decoding of identity.”	91
Figure 3.8.	“Cross-modal representation of identity using rate and event codes.”	94
Figure 3.9.	“Additional Identity Neurons in Primate Hippocampus.”	115
Figure 3.10.	“Marmoset hippocampus neurons have high baseline firing rates.”	116
Figure 3.11.	“Match versus Mismatch Neurons.”	117
Figure 3.12.	“Identification of predictive time bins.”	118
Figure 3.13.	“Exemplar predictive neurons.”	119
Figure 3.14.	“Variability of visual behavior relative to identity-specific predictive time bins.”	120
Figure 3.15.	“Conjoined predictive populations.”	121
Figure 3.16.	“Decoder Schematics.”	122
Figure 3.17.	“Multiple individuals classified by winner-take-all model.”	123
Figure 3.18.	“Decoding improved by melding multiple recording sessions.”	124
Figure 3.19.	“Decoding performance with and without identity selective neurons averaged over preferred individuals.”	125
Figure 3.20.	“Identity network model for individual subjects.”	126
Figure 3.21.	“Separating stimulus categories at multiple probe locations.”	127
Figure 3.22.	“Low-dimensional projections of our rate code and event code.”	128

Figure 3.23.	“Separability of social categories.”	129
Figure 3.24.	“Quantification of latent activity.”	130
Figure 3.25.	“Stability of manifold projections.”	131
Figure 3.26.	“Separability of socially-agnostic categories.”	132
Figure 3.27.	“Schematic drawing of experimental setup.”	132
Figure 3.28.	“Anatomical locations of microwire bundles across animals.”	133

LIST OF TABLES

Table 1.1.	Parameters used in the simulation of radial cAMP profiles	45
Table 1.2.	Parameters used in the simulation of cAMP biosynthesis	46
Table 2.1.	Particle properties of spiral tips from the cardiac models.	62
Table 2.2.	Power law fits for annihilation rates.	63
Table 3.1.	Neural decoder hyperparameter settings	105

ACKNOWLEDGEMENTS

I would like to acknowledge Professor Wouter-Jan Rappel for his support as the chair of my committee. Through multiple drafts and many long nights, his guidance has proved to be invaluable.

I would also like to acknowledge the Cortical Systems and Behavior Laboratory, without whom chapter three would not be possible. It is their support that helped me in an immeasurable way.

Chapter 1, in full, is a reprint of the material as it appears in the Proceedings of the National Academy of Sciences of the United States of America. 2021. Tyree, TJ*; Karmakar, R*, Gomer, RH, Rappel WJ. United States National Academy of Sciences, 2021. The dissertation author was the primary investigator and author of this paper [102].

Chapter 2, in part, has been submitted for publication of the material as it may appear in the Physical Review E, 2023, Tyree, TJ; Murphy, P; Rappel WJ. American Physical Society, 2023. The dissertation author was the primary investigator and author of this paper.

Chapter 3, in full, is a reprint of the material as it appears in Science. 2023. Tyree, TJ; Metke M; Miller CT. American Association for the Advancement of Science (United States), 2023. The dissertation author was the primary investigator and author of this paper [207].

We thank Robert Kay, Peter van Haastert, and Robert Insall for helpful discussions regarding chapter one. We thank the Open Science Grid for allocation of computational resources used to generate certain results in chapters one and two [158, 191]. We thank Hristos Courellis for assistance with data collection and David Leopold for comments on a previous version of the manuscript in chapter three.

VITA

- 2017 Bachelor of Arts, Physics, Cornell University
- 2017 Bachelor of Arts, Mathematics, Cornell University
- 2017–2018 Teaching Assistant, Department of Physics
University of California San Diego
- 2018–2023 Research Assistant, University of California San Diego
- 2023 Doctor of Philosophy, Physics, University of California San Diego

PUBLICATIONS

“Thermal contraction of aqueous glycerol and ethylene glycol solutions for optimized protein-crystal cryoprotection.” *Acta Crystallographica Section D: Structural Biology*, vol. 72(6), pp 742–752, 2016

“Measuring the densities of aqueous glasses at cryogenic temperatures.” *JoVE (Journal of Visualized Experiments)*, vol. (124), pp e55761, 2017

“Density and electron density of aqueous cryoprotectant solutions at cryogenic temperatures for optimized cryoprotection and diffraction contrast.” *Acta Crystallographica Section D: Structural Biology*, 74(5), 471-479. 2018

“Cell dispersal by localized degradation of a chemoattractant.” *Proceedings of the National Academy of Sciences* 118.6, e2008126118. 2021

“Cross-modal representation of identity in the primate hippocampus.” *Science* 382, 417–423. 2023

FIELDS OF STUDY

Major Field: Physics with Specialization in Quantitative Biology

Studies in Applied Mathematics
Professors Massimo Vergassola and Melvin Leok

Studies in Mechanics
Professor Dan Dubin

Studies in Statistical Mechanics
Professor Dan Arovas

Studies in Electromagnetism
Professor Michael Fogler

Studies in Field Theory
Professor John McGreevy

Studies in Quantum Information Theory
Professor John McGreevy

Studies in Quantitative Biology
Professors Terence Hwa, Olga Dudko, David Kleinfeld, Kevin King, and Karl Willert

Studies in Data Science
Professor Yoav Freund

Studies in Business
Professor Michael Lutz

ABSTRACT OF THE DISSERTATION

Applications of Mathematical Physics to Quantitative Biology

by

Timothy John Tyree

Doctor of Philosophy in Physics with a Specialization in Quantitative Biology

University of California San Diego, 2023

Wouter-Jan Rappel, Chair

Interdisciplinary investigation has the potential to advance all fields involved. In this dissertation, three distinct fields of Quantitative Biology are discussed and advanced incrementally using the general tools of Mathematical Physics. Chapter one applies reaction-diffusion equations to explain the dispersal of cells by localized degradation of a chemoattractant, which could explain the migration of leukocytes from the thymus and be a mechanism for morphogenesis. Chapter two investigates a particle model wherein an attractive force explains the termination of atrial fibrillation. Atrial fibrillation—the most common cardiac arrhythmia in the world with approximately 30 million patients in 2010—is associated with increased morbidity and mortality. Chapter three applies machine learning to explain social recognition in primate hippocampus,

showing that cross-modal representations of identity can be achieved by at least two distinct neural mechanisms and that these representations comprise multiple social categories that reflect different relationships. Together, these chapters demonstrate the general capacity of Mathematical Physics to advance Quantitative Biology in addition to the capacity for Quantitative Biology to motivate novel analytic results and analyses within Mathematical Physics.

Introduction

Chapters 1-3 are each self-contained, and can thus be read in any order. The reader is encouraged to consult the Table of Contents on the basis of personal interest. For each chapter, this Introduction discusses the state of the field prior to our work. After which, a synopsis of the chapter is provided.

Many studies have investigated how cells can move towards the source of a chemoattractant, but relatively little is known about mechanisms that can cause cells to move *away* from a location. Collective cell migration away from a location has been implicated in various biological events including cancer cell metastasis away from a tumor [32, 121, 159, 190], and migration of leukocytes away from the thymus [5, 92, 94, 219].

Although cancer cell migration has been attributed to haptotaxis [30], localized degradation of the extracellular matrix can explain the metastasis of cancer cells [66], similar to how localized degradation of a chemoattractant can explain the dispersal of cell aggregates in Chapter 1. Furthermore, degradation of the pleiotropic sphingolipid metabolite, sphingosine-1-phosphate (S1P), by S1P lyase (SPL) explains the emigration of leukocytes from the thymus [111]. As SPL is a membrane-bound protein, the degradation of S1P is therefore localized to the maturing leukocytes, creating an outward gradient of S1P towards the blood which is rich in S1P [155]. While mathematical models have successfully described thymic emigration for given concentration fields of S1P [196], no mathematical model of localized attractant degradation has been found as has been done in Chapter 1. This suggests that the mathematical model proposed in Chapter 1 can be applied immediately to thymic emigration in addition to cancer metastasis.

Chapter 1 concerns itself with the social amoeba, *Dictyostelium discoideum*, which is

known to migrate towards cyclic adenosine 3',5'-monophosphate (cAMP) during the aggregation phase of its life cycle [37], as is shown in Fig. 1. This has been exploited in numerous microfluidic studies to show single cells can navigate complex mazes by following the chemotactic gradient prescribed by a reacting and diffusing concentration field of cAMP [206]. Similar studies have ascertained properties of the locomotion of the social amoeba [62], in addition to temporal dependence of sensitivity of the social amoeba to attractant gradient [100]. A dependence of chemotaxis on background attractant concentration has been confirmed in the social amoeba [101], which has proved to be an key component to the mechanism of dispersal proposed in Chapter 1.

In Chapter 1, we show that small aggregates of the social amoeba, *Dictyostelium discoideum*, can show dispersal behavior during which cells move *away* from the aggregate. Using a combination of experiments and modeling, we show that this dispersal can arise due to a competition between the diffusible chemoattractant and the enzyme that degrades it, and that the localized degradation of the chemoattractant may be a mechanism for morphogenesis.

Chapter 2 concerns itself with the pair-annihilation of particles. Pair-annihilation events are ubiquitous in a variety of spatially extended systems. The statistics of these events are often studied using computationally expensive simulations. Examples of such physical systems include many soft-matter and active-matter physical systems that exhibit spatiotemporal patterning. One example includes topological defects in nematic liquid crystals that migrate and annihilate when they meet [53, 123]. The existence of these nematic defects are an unavoidable consequence of the breaking of a continuous symmetry [134], and the motion of these defects are explained by continuous energy injections from internal elements [11, 130, 173]. Such nematic defects have been reported in thin films of actin filaments [223], in microtubule–kinesin bundles [187], and in *in vitro* suspensions of cyto-skeletal proteins [82].

Living systems also exhibit pair-annihilation of point-like topological defects. In biofilms composed of *Escherichia coli*, for instance, nematic ordering similarly emerges with topological defects being present in their velocity fields [215]. The annihilation of these topological defects

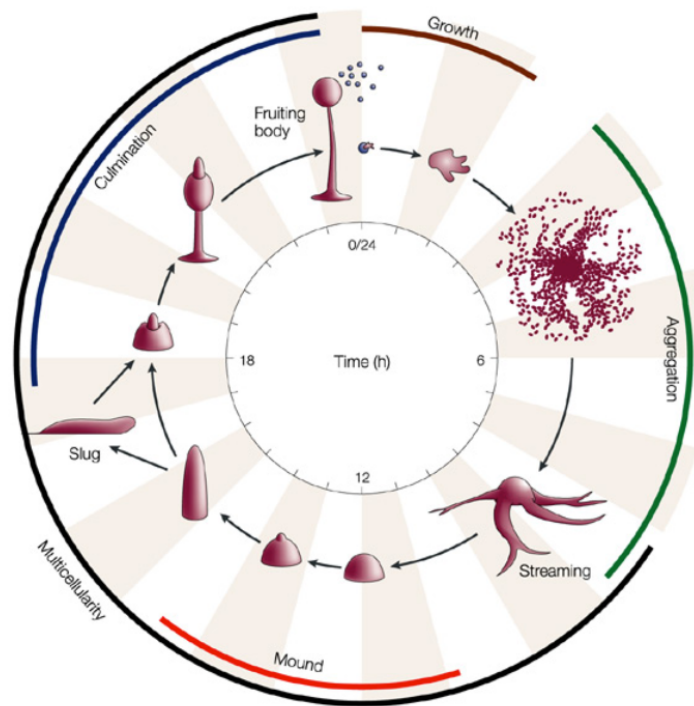


Figure 1. Life cycle of the social amoeba. Developmental morphogenesis of single cells begins approximately four to six hours after the removal of sustenance with the aggregation phase, during which the social amoeba, *Dictyostelium discoideum*, secretes cyclic adenosine 3',5'-monophosphate (cAMP), which serves as a chemoattractant for their conspecifics. After approximately six to eight hours of aggregation, quorum-sensing genes express to yield complex multicellular activity that culminates with the formation of the fruiting body at the peak of a stalk of sacrificial cells. Upon a decrease in humidity or an increase in light, spore cells are released from the fruiting body and are carried away by the wind, facilitating their spread and the continuation of their life cycle, allowing cellular growth and division to occur again at the level of single cells. Figure is from Ref. [36].

have been proposed as the mechanism for the buckling of individual layers, which lead to the formation of biofilm layers [20, 43]. Such buckling has led to mound formation in biofilms composed of neural progenitor cells [103].

A living system with topological defects of particular importance is the human heart during atrial fibrillation, which is the most common type of cardiac arrhythmia in the world and is associated with increased morbidity and mortality— affecting over 30 million people worldwide in 2010 [39, 116, 140, 144]. Atrial fibrillation is characterized by disorganized electrical activity in the upper chambers of the heart, which are responsible for filling the lower chambers of the heart with blood, as is shown in Fig. 2. When the left or right atrium fibrillates, blood is not pumped as efficiently, allowing blood to pool, stagnate, and eventually clot [71], which can lead to a pulmonary embolism in the case of the right atrium or a thrombotic stroke in the case of the left atrium [38]. Atrial fibrillation is often treated with blood thinners [162], which can have the undesirable side effect of excessive bleeding in response to wounds and fails to address the discomfort often associated with atrial fibrillation.

Other treatments for atrial fibrillation include catheter ablation procedures, which use either heat or cold to ablate portions of the atrium. Such procedures tend to be less successful for persistent atrial fibrillation compared to paroxysmal atrial fibrillation [211]. The most common kind of catheter ablation procedure is the pulmonary vein isolation procedure, which seeks to isolate electrical activity in the pulmonary veins from the left atrium [84]. Pulmonary vein isolation procedures often need to be repeated for remission of atrial fibrillation [27, 150]. Focal ablations of the pulmonary veins have proven effective for some case studies [77, 83], though such procedures can lead to stenosis of the pulmonary veins [77]. A demand therefore exists for a mechanism that can spontaneously cure atrial fibrillation, and such a mechanism is proposed in Chapter 2. One may hope that this mechanism may guide future drug discovery to cure clinically significant symptoms of persistent or paroxysmal atrial fibrillation.

During atrial fibrillation, spiral waves continuously break down to form new spiral waves, which are in turn removed from the system through collisions with other spiral waves or with

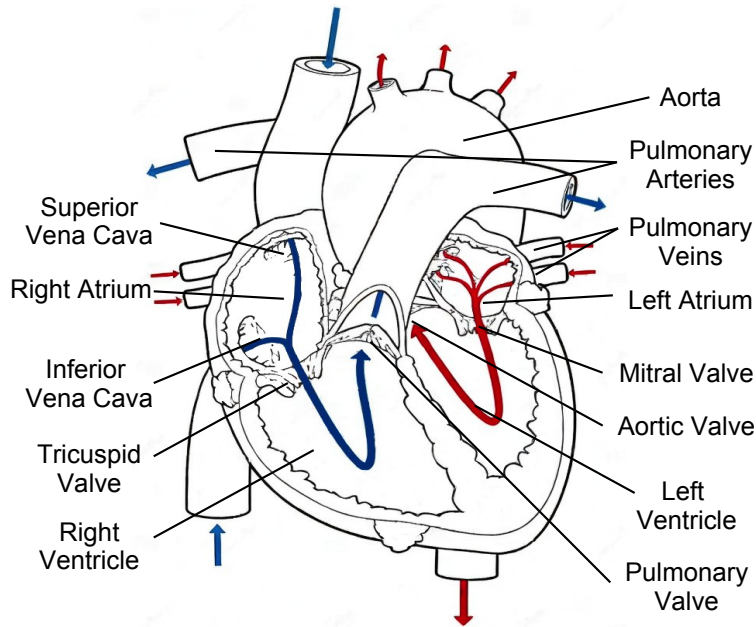


Figure 2. Flow diagram of the human heart. Blue arrows indicate flow of deoxygenated blood while red arrows indicate flow of oxygenated blood. Blood passively flows into the right atrium via the superior and inferior vena cava at a pressure of approximately 5 millimeters of mercury. Upon contraction of the right atrium, the tricuspid valve opens and the right ventricle fills with blood. Upon contraction of the right ventricle, the pulmonary valve opens and blood flows into the lungs via the pulmonary arteries. By conservation of volume, an equal amount of blood leaves the lungs and enters the left atrium via the pulmonary veins. Upon contraction of the left atrium, the mitral valve opens and blood flows into the left ventricle. Upon contraction of the left ventricle, the aortic valve opens and blood flows into the rest of the body via the aorta.

nonconducting boundaries. Studies have manipulated this process using optogenetic procedures on explanted heart tissue [19, 128]. There is even some numerical evidence showing that the chirality of spiral waves can be modified using optogenetic intervention [118].

The motion of these spiral waves has long been known to exhibit an onset of mathematical chaos [74], with a Lyapunov exponent becoming positive [208, 222], which is a well-known hallmark of the onset of chaos [1, 31, 58, 86]. In addition to cardiac tissue [41, 99, 174, 202], this spiral defect chaos is present in a variety of chemical and biological pattern-forming systems [18, 44, 49, 57, 59, 60, 88, 90, 152, 164, 177, 209]. The tips of these spiral waves undergo pair-annihilation events as if they were point-like particles [119, 120, 212]. The pair-annihilation of these spiral wave tips have been recently described by a stochastic birth-death process [212, 175]. By simulating cardiac models on various domain sizes, the creation and annihilation rates of spiral tips were determined. Using these rates, the termination time was computed and was shown to be exponentially distributed, consistent with experiments and clinical data [50, 212, 175]. This mean termination time is a quantity of interest in the context of cardiac dynamics as termination indicates the heart has transitioned into normal sinus rhythm. Thus, decreasing the mean termination time to below the characteristic time scale of blood clotting is a necessary and sufficient condition for curing atrial fibrillation. Determination of the mean termination time *in silico* required expensive simulation of rare termination events for which all spiral tips have annihilated.

In Chapter 2, we develop an alternative approach in which we simulate the annihilation of spiral wave tips in cardiac models using a simple and computationally efficient model. Spiral wave tips are represented as particles with dynamics governed by diffusive behavior and short-ranged attraction. The parameters for diffusion and attraction are obtained by comparing the motion of the particles to the trajectories of spiral wave tips in cardiac models during spiral defect chaos. We show that the particle model can reproduce the annihilation rates of the spatially extended cardiac models and can determine the statistics of spiral wave dynamics, including its mean termination time, for an arbitrary domain size. We also show that increasing the effective

attraction coefficient will result in the removal of long termination times in electrophysiological parameter regimes, making it a possible target for pharmaceutical interventions, thereby providing a mechanism for curing atrial fibrillation.

Chapter 3 concerns itself with cross-modal integration of social signals in the primate brain. Faces and voices are the dominant social signals used to recognize individuals amongst human and nonhuman primates [2, 12, 193, 204]. Yet it is not known how these critical signals are integrated into a cross-modal representation of individual identity in the primate brain.

Numerous animal studies have shown unimodal representations of conspecifics are present in the brain by studying their learned behavioral response to relevant social signals such as vision, audition, or olfaction [16, 29, 45, 54, 96, 97, 106, 172, 186, 218]. Yet there have been none that show these unimodal signals are integrated into a cross-modal neural representation of identity by studying the behavior of individual neurons.

Several interesting studies of unimodal recognition exist. For example, a behavioral study has recently shown rats were capable of discerning social categories using olfaction alone [96], and social isolation disrupted olfactory social recognition memory and impaired coupling between the olfactory bulb and the dorsal hippocampus in mouse [6]. Normal development of the olfactory bulb was observed in mice with an oxytocin knock-out, though their social cognition was severely impaired [65]. Furthermore, visual recognition of conspecifics was supported by numerous behavioral studies in macaque [80], in goat [106], and in fish [91, 104, 217]. Moreover, face-selective patches of the macaque cortex have been found [87, 221], though these studies did not consider individual neurons, as is done in Chapter 3.

Additionally, there is a plethora of behavioral studies that support cross-modal representation of identity in animals. For example, a behavioral study supported cats as being capable of cross-modal recognition of emotions of conspecifics in addition to humans [167]. Additionally, a behavioral study showed cross-modal representation of familiar human identities in cat [201]. Similar behavioral studies in horse have shown cross-modal recognition of familiar humans [114, 160] in addition to conspecifics [161]. Similar cross-modal behavioral studies

have been conducted in dog [3], in goat [157], in crows [109], and in non-human primates [2]. However, these studies made no attempt to record from neurons either at the single-cell level or at the population-level. This distinguishes the results of Chapter 3, which identifies single neurons in marmoset hippocampus that respond selectively and invariantly to the face and voice of familiar conspecifics.

Such selective and invariant representations have been found in human hippocampus with the identification of identity neurons [169]. Further study has shown human hippocampus possesses putative "concept cells" that are invariant to the modality of the stimulus [170, 171]. However, it remains to be shown in human hippocampus how these unimodal signals are integrated into a cohesive cross-modal representation of social identity.

The architecture of hippocampus is remarkably conserved between different species. The same basic structure is present in human and non-human primates alike [34]. For example, it has been suggested before that one of the functions of the CA1 synapse is to serve as a mismatch detector in human hippocampus [122] by comparing projections from the CA3/CA2 to more direct projections from the DG, as is shown in non-human primate by the solid and dashed white lines in Fig. 3, respectively. The presence of a mismatch detector has supported through olfaction in the CA1 synapse of rat hippocampus [151]. The presence of a mismatch detector is supported in marmoset by the relatively large number of match *versus* mismatch (MvMM) neurons that we found in the CA1 in Chapter 3. The hypothesized intuition is that the CA1 serves as a comparator between what is observed and what is expected, which allows the hippocampus to switch between memory encoding and memory retrieval.

The common marmoset, *Callithrix jacchus*, exhibits pro-social behavior similar to that of humans, including pair-bonding, cooperative care for their young, and imitation— a social behavior rarely seen outside of the apes [25, 135, 185, 214]. Moreover, marmosets exhibit social learning [26]. And like other social mammals [89, 129, 220], marmosets exhibit social hierarchies that are organized along familial lines [47, 51]. For these reasons, marmosets have long been regarded as the model organism for social cognition [15, 34, 69, 181, 180, 216] and

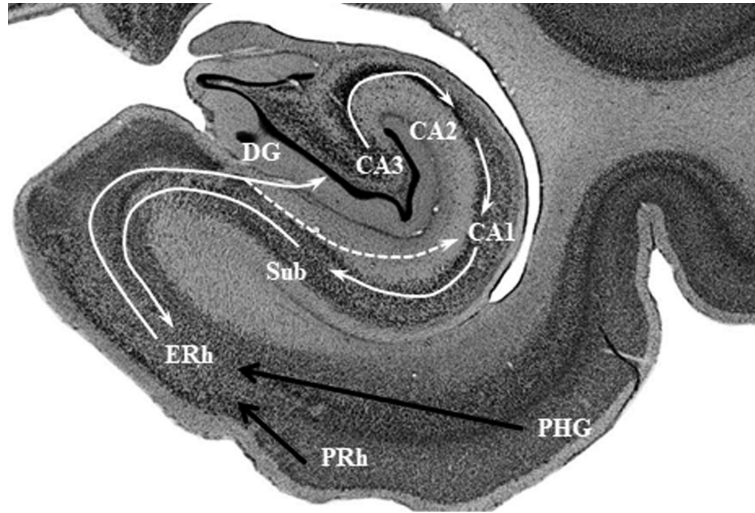


Figure 3. Flow diagram of the primate hippocampus. A thionin-stained section through the midbody of the hippocampus of a rhesus monkey. Arrows indicate information flow through the trisynaptic circuit. The parahippocampal gyrus (PHG) and the perirhinal cortex (PRh) project to the entorhinal cortex (ERh) according to the solid black arrows. The ERh projects to the *dentate gyrus* (DG), which projects to the *cornu ammonis* synapses (CA3, CA2, CA1) according to the solid white arrows, respectively. The CA1 synapse projects to the *subiculum* (Sub), which projects back to the ERh according to the solid white arrows. It has been proposed that there exists a more direct pathway from the DG to the CA1, as is indicated by the dashed white arrow. Figure is cropped from Ref. [7].

are expected to play a prominent role in the next chapter of neuroscience [14].

In Chapter 3, we show that while, like humans [169, 171, 213], single neurons in the marmoset hippocampus exhibit selective and invariant responses when presented with the face or voice of a specific individual conspecific. A parallel mechanism for representing the cross-modal identities for multiple individuals is evident both within single neurons and at a population level. Manifold projections likewise showed separability of individuals, as well as clustering for others' families, suggesting that multiple learned social categories are encoded as related dimensions of identity in hippocampus. These findings demonstrate that neural representations of identity in hippocampus are both modality-independent and reflect the hierarchical structure of the primate social network.

Chapter 1

Cell dispersal by localized degradation of a chemoattractant

Chemotaxis, the guided motion of cells by chemical gradients, plays a crucial role in many biological processes. In the social amoeba, *Dictyostelium discoideum*, chemotaxis is critical for the formation of cell aggregates during starvation. The cells in these aggregates generate a pulse of the chemoattractant, cyclic adenosine monophosphate (cAMP), every 6-10 minutes, resulting in surrounding cells moving towards the aggregate. In addition to periodic pulses of cAMP, the cells also secrete phosphodiesterase (PDE), which degrades cAMP and prevents the accumulation of the chemoattractant. Here we show that small aggregates of *Dictyostelium* can disperse, with cells moving away from instead of towards the aggregate. This surprising behavior often exhibited oscillatory cycles of motion towards and away from the aggregate. Furthermore, the onset of outward cell motion was associated with a doubling of the cAMP signaling period. Computational modeling suggests that this dispersal arises from a competition between secreted cAMP and PDE creating a cAMP gradient that is directed away from the aggregate, resulting in outward cell motion. The model was able to predict the effect of PDE inhibition as well as global addition of exogenous PDE and these predictions were subsequently verified in experiments. These results suggest that localized degradation of a chemoattractant is a mechanism for morphogenesis.

Eukaryotic cell motion guided by gradients of diffusible chemoattractants plays a crucial

role in wound healing, embryology, the movement of immune cells, and cancer metastasis [178, 141, 42, 40]. In some cell types, including neutrophils and the social amoeba *Dictyostelium discoideum*, gradient generation occurs through a relay mechanism where cells stimulated by the chemoattractant secrete additional chemoattractant [4, 113, 200]. To prevent continuous build-up of chemoattractants, many systems use enzymes to degrade the chemoattractant. These enzymes are either membrane-bound, with their active sites facing the extracellular environment, or can diffuse in the surrounding environment [8, 153]. In addition, chemoattractants may be removed by other methods, including receptor uptake or decoy receptors [95, 124].

Compared to chemoattraction, relatively little is known about chemorepulsion, exemplified by the dispersal of immune cells out of a tissue during the resolution of inflammation. Under some conditions in chamber-based assays, chemoattractant-degrading enzymes can create a local minimum in chemoattractant concentration, resulting in chemoattractant gradients that point away from areas with high cell density [52, 205, 198].

In a nutrient rich environment, *Dictyostelium* cells grow as separate, independent cells. When deprived of food, these amoebae start to secrete the chemoattractant cyclic adenosine 3',5'-monophosphate (cAMP) in an oscillatory manner [107, 126]. The secreted cAMP rapidly diffuses to neighboring cells, which, in turn, start to secrete cAMP as well. The resulting relay mechanism generates periodic waves that sweep through the cell population with a period of 6-10 min [81]. For wave periods smaller than 10 min, cells only respond to incoming waves, ignoring the “back of the wave”, and directionally move towards higher concentrations of cAMP [145, 192], form streams, and eventually aggregate into mounds of up to $\sim 100,000$ cells. Cells within the aggregate subsequently differentiate and form a fruiting body that contains the majority of the original population of cells as a mass of spores held up off the substrate by a stalk to maximize dispersal of spores [107, 126]. In addition to cAMP, *Dictyostelium* cells also secrete phosphodiesterases (PDEs), which hydrolyse cAMP and which prevents continuous build-up of cAMP [197, 8]. The presence of PDE is essential for aggregation, and mutants that cannot secrete PDE fail to form viable aggregation centers [61].

We reasoned that the competition between a time varying chemoattractant signal and an inhibitor can result in guidance that changes direction as a function of time. To test this hypothesis, we examined the aggregation of *Dictyostelium* cells at low cell densities. We present evidence that aggregates of developing *Dictyostelium* cells display dispersal behavior in which cells are “repelled” from, rather than attracted to, aggregates. This behavior was only present for small aggregates. Furthermore, we show that during this dispersal behavior oscillatory cAMP signaling is still active, but that its period is abruptly increased at the onset of dispersal. We develop a model for cell aggregation and show that periodic signaling of cAMP, together with a spatial profile of PDE, can explain the observed dispersal. Furthermore, the model predicts that the disruption of the PDE profile, either by removal of PDE or by globally adding PDE, will result in the abolishment of dispersal. These predictions were subsequently verified in experiments. Our results suggest that by modulating the frequency of cAMP signaling, small aggregates can shed their cells, potentially avoiding mounds that would form small and thus relatively ineffective fruiting bodies.

Materials and methods

Cells and chemicals

Cells of the axenic *Dictyostelium discoideum* strain AX4 were transformed to express a fusion of GFP to LimE (Δ coil LimE-GFP) and a gene encoding a fusion of RFP to Coronin (LimE GFP/corA RFP) [70]. In addition, we transformed wild-type AX4 cells with the plasmid Flamindo2 expressing Flamindo2-GFP, a marker for cytosolic cAMP levels with a fluorescent intensity that is inversely proportional to the level of cAMP [148, 149, 85].

We used cultures having a doubling time less than 8 hours, because we found that the slower growing cells were less chemotactically active. The cells were grown in submerged shaking culture in HL5 medium (35.5g HL5 powder (Formedium, Norfolk, UK) and 10mL Penicillin-Streptomycin (10,000 U/mL; Gibco, Thermo Fisher Scientific, USA) per liter of

DI water) [199]. For starvation, when cells reached their exponential growth phase ($3-4 \times 10^6$ cells/mL), they were harvested by centrifugation at 3000 rpm for 5 min, resuspended in KN_2/Ca buffer (14.6 mM KH_2PO_4 , 5.4 mM Na_2HPO_4 , 100 μ M $CaCl_2$, pH 6.4), collected by centrifugation, and re-suspended in KN_2/Ca at 10^7 cells/mL.

1,4-dithiothreitol (DTT, Sigma, St. Louis MO) was prepared by dissolving DTT in de-ionized water at a concentration of 10mM. We deposited 20 μ l directly on top of a dispersing aggregate. To test the effects of PDE1, we used 10 μ L of PDE 3',5' cyclic nucleotide activator-deficient from bovine heart (Sigma) dissolved in 50% glycerol/50% water at a concentration of 0.5mg/ml.

Experimental setup

For aggregate formation, 4 mL of KN_2/Ca buffer was added to a 32mm diameter glass bottom Petri dishes. We deposited 2×10^6 vegetative cells, obtained from the shaking culture after removing the growth media and washed twice with KN_2/Ca buffer, by placing 40 μ L drops at 5 different locations and waited for 10 min for cells to attach to the glass. Differential interference contrast (DIC) images were taken every minute for 20h on a spinning-disk confocal Zeiss Axio Observer inverted microscope using a 10X objective with a Cascade QuantEM 512SC camera (Roper Scientific, Tucson, AZ). To quantify intracellular cAMP dynamics, we captured fluorescent time-lapse images using Slidebook 6 (Intelligent Imaging Innovations, Denver, CO). Images were analyzed using custom-made scripts in Python.

Aggregate size and location calculation

Aggregate size was determined by manually tracing the aggregate perimeter with ImageJ (National Institutes of Health, Bethesda, MD), repeated at least 5 times after which the average was taken. The location of the aggregate was determined by manually identifying the center in ImageJ for at least once every 15 min. The trajectory of the aggregate was then computed by fitting a spline through these points.

Cell motion measurements and analysis

Cell motion for cells outside of the aggregate was measured using dense optical flow, which was computed using the grayscale DIC channel and the dense inverse search (DIS) algorithm, described in a previous study [110]. We used a specific DIS implementation in the OpenCV library of Python ('cv2.DISOpticalFlow_create') using the fastest available parameter settings. Inward/outward flow was computed with respect to the centroid of the aggregate, and the radial component of the velocity was temporally averaged over a window between 90 s and 5 min. Using the raw dense optical flow, we computed the total displacement and the displacement in the radial direction from which the radial chemotactic index CI was computed as the ratio of radial displacement and total displacement.

To compute net average cell motion, we averaged the radial velocity of all cells that were in an annulus centered at the centroid and with a inner radius that is approximately $10\ \mu\text{m}$ beyond the maximum radius of the aggregate and with an outer radius up to $300\ \mu\text{m}$, dependent on the apparent motion of the cells. In order to normalize net cell motion by cell area, we computed the average cell area in the relevant annulus. For this, the location of the perimeter of a cell was computed by zeroing and then normalizing the DIC channel, performing edge detection via Scharr filtration [188], and then binarizing to achieve a scalar phase field with value zero everywhere except at the edges of the cell. To compute the area of this cell, we first averaged adjacent time frames. To decrease sensitivity to signal noise, this average was blurred with a Gaussian filter. The result was binarized such that the interior of the cell took the value of unity and the area outside took the value of zero. This result was then used to compute the average cell area in the annulus. To visualize cell motion, we color-coded the dense optical flow results. Finally, the median CI was computed as the median value amongst all pixels located in the annulus described above, averaged over 2.5 min. Further details of the image analysis are provided in the Supplementary Information.

Pipette aspiration experiments

Extracellular fluid near a dispersing aggregate of cells expressing *Flamindo2* was aspirated during its dispersing phase using a micropipette tip with an inner diameter of $180\ \mu\text{m}$ (Eppendorf, USA). The aspirated fluid ($20\ \mu\text{L}$) was immediately deposited near ($\approx 50 - 100\ \mu\text{m}$) a non-dispersing aggregate. The position of the centroid of the aggregate was determined by peak detection using the python package *Trackpy*. Single cell tracking was then manually performed. Shedding angle for each dispersed cell was computed as the angle between two rays with the first ray beginning at the micropipette tip and extending towards the centroid of the aggregate and the second ray beginning at the aggregate and extending towards the initial position of the cell.

Statistics and reproducibility

P values were computed with the Wilcoxon rank sum test using MATLAB (2017b; The Mathworks). Experimental values are reported as median (interquartile 1- interquartile 3) or as mean \pm standard deviation. A p value less than 0.05 was considered to be significant.

Computer simulations

Our 2D simulations modeled radial concentration profiles of the chemoattractant cAMP in a disk-shaped domain using the phase field approach [117]. This domain consisted of a circular sub-domain of radius $r_0 = 50\ \mu\text{m}$, representing the aggregate containing a large number of cells (see also below), and 100 individual cells, randomly placed in an annulus with radii $150\ \mu\text{m}$ and $350\ \mu\text{m}$ (Fig. 1.3A). The aggregate was assumed to secrete cAMP in an oscillatory manner as described in previous studies [131] and to diffuse in the extracellular space (Supplementary Information, Fig. 1.7). At a distance far from the aggregate, taken here to be $1000\ \mu\text{m}$, the cAMP concentration was set to the constant background value $cAMP_{back}$. As initial condition, the concentration of cAMP was set equal to $cAMP_{back}$ and cell motion was determined after the first cAMP oscillation cycle. In addition, PDE was assumed to be secreted by the aggregate at a constant rate, consistent with experimental work [78]. Since aggregate dispersal occurs

many hours after the onset of the experiment, we took as initial condition the spatial PDE profile, obtained after constant secretion and degradation for 60 minutes (for details, see Supplementary Information). The lengthscale of this profile, L_{PDE} , is determined by the diffusion constant and degradation constant of PDE. cAMP was linearly degraded by PDE with a degradation constant k_{PDE} . Individual cells were assumed to secrete constant PDE and oscillatory cAMP, with amplitudes that were scaled relative to the number of cells in the aggregate. Specifically, using confocal imaging, we estimated the number of cells in a dispersing aggregate to be approximately 400 (Supplementary Information, Fig. 1.8) so that the amount of secretion from a single cell is $1/400^{th}$ of that of the aggregate. In our reduced 1D model, the cAMP concentration is computed along a radial line and where the PDE profile is given by the steady-state solution (see the Supplementary Information for further numerical details and Supplementary Information, Table 1.1 for parameter values).

We determined the movement of the cells by computing the local gradient of cAMP, $\nabla cAMP$. Cell motion was in the direction of this gradient with basal speed v_0 if the magnitude of the gradient exceeded a threshold δ^* . For absolute values of the gradients smaller than this threshold, thought to be below the detection capabilities of the cell, the cell will not move at all. Based on earlier work, the threshold was taken to be 0.1 nM across a cell body of $15\mu m$, resulting in $\delta^* = 6.67 \times 10^{-3} nM/\mu m$ [195]. This allowed us to compute the net displacement for each cell for an entire cAMP oscillation cycle. An aggregate was considered to be dispersive if cell motion during one cycle was outward for all cells.

Results

Cell aggregates display dispersive behavior

When plated at low density, we observed that developed *Dictyostelium* cells aggregated into small-sized aggregates. These aggregates grew in size by attracting nearby cells using cAMP signaling, and most subsequently merged with others to form larger ones (at least 1,000

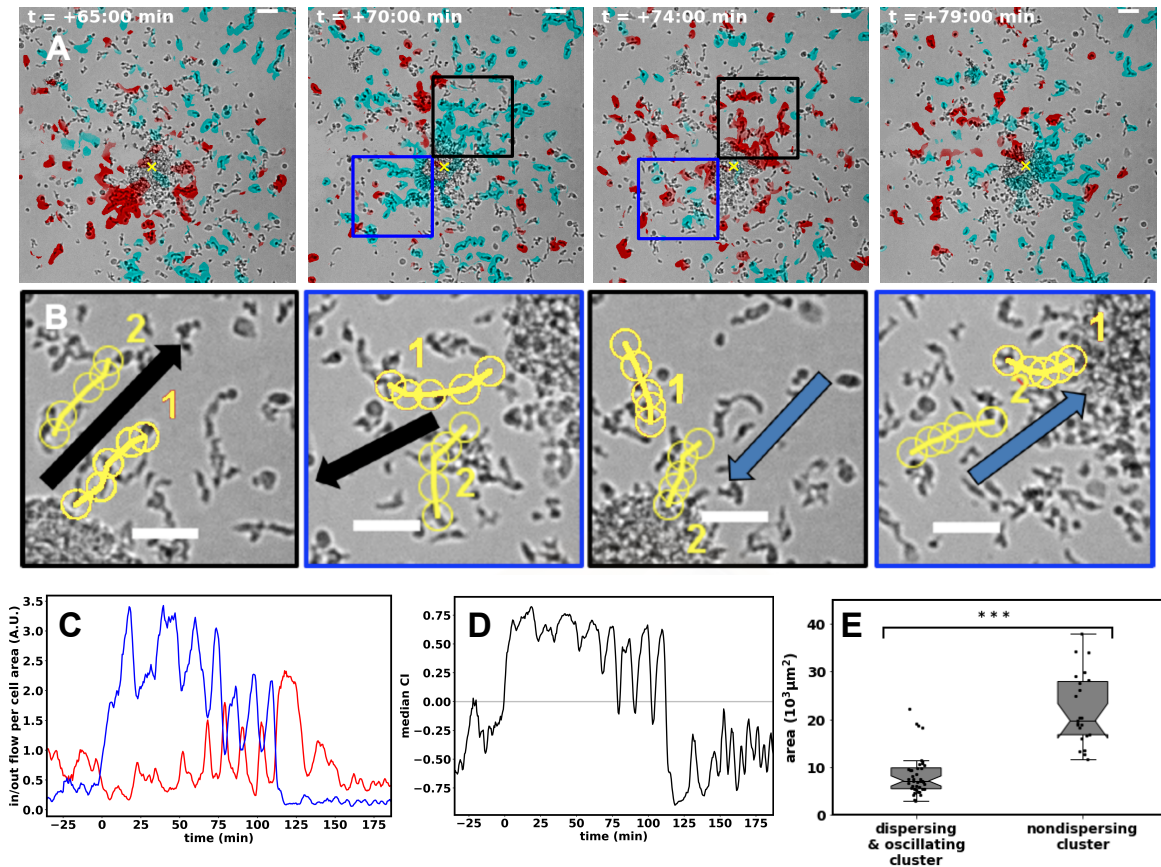


Figure 1.1. Dispersal of cells. [a] Micrographs showing dispersing cell motion, visualized using dense optical flow, near a dispersing aggregate at four different times. Dispersal started at $t = 0$ and inward/outward motion is indicated in red/blue while the aggregate center is marked by the yellow x (scalebar: $50 \mu\text{m}$). [b] Examples of single cell trajectories during inward and outward and inward motion, taken from the middle two panels in [a]. The symbols indicate the cell location at each frame (separated by 1 min). [c] Spatially averaged inward/outward motion (red/blue), normalized by total cell area, for cells within a distance of $100 \mu\text{m}$ and $300 \mu\text{m}$ from the aggregate center as a function of time. [d] Median CI for all cells within the same region as in [b]. [e] Histogram of the median aggregate size for dispersing and oscillating aggregates and for non-dispersing aggregates.

aggregates for each experiment). Surprisingly, however, some aggregates showed dramatically different behavior. Instead of acting as an attractant source, resulting in inward motion of neighboring cells, they showed distinct dispersal during which cells moved *away* from the aggregates as single cells or as a small groups of cells (Movie S1). In addition, these aggregates often displayed oscillatory dynamics, during which outward motion was followed by inward motion in a repetitive cycle.

To quantify the cell motion, we analyzed the images using dense optical flow, which calculates the motion between two image frames (see Methods). This method avoids the use of explicit cell tracking, which is challenging to implement in an automated way. An example of the results of the optical flow algorithm for two cycles of a dispersive aggregate is shown in Fig. 1.1A, where inward (outward) cell motion is displayed using red (blue) shading. Note that this shading extends well beyond the position of the cell in the snapshot since it represents the optical flow data for the entire trajectory of each cell. In the first panel, motion is primarily inward while in the second panel, taken 5 min later, the motion has reversed and is now outward. This oscillation repeats itself in panel 3 and 4. The panels in Fig. 1.1B show some examples of manually tracked cells that were present in the black/blue squares of the middle panels in Fig. 1.1A.

To further quantify the dispersal behavior, we computed the spatially averaged outward and inward flow near aggregates. For this, we averaged over all cells that were within an annulus centered at the aggregate with an inner radius of $100\ \mu\text{m}$ and an outer radius of $300\ \mu\text{m}$. The result for the aggregate in Fig. 1.1A, normalized by the total cell area (see Methods), is presented in panel (B) where we plot the inward and outward motion as a function of time in red and blue, respectively. This shows that cell motion was mainly inward before the onset of dispersal, arbitrarily set here and in all other figures at $t=0$, since the inward flow was larger than the outward flow. At the onset of dispersal, however, the outward flow was suddenly larger than the inward flow, indicating net dispersal. Furthermore, following this onset, the dynamics of the flow showed oscillatory behavior, with predominantly outward motion followed by predominantly

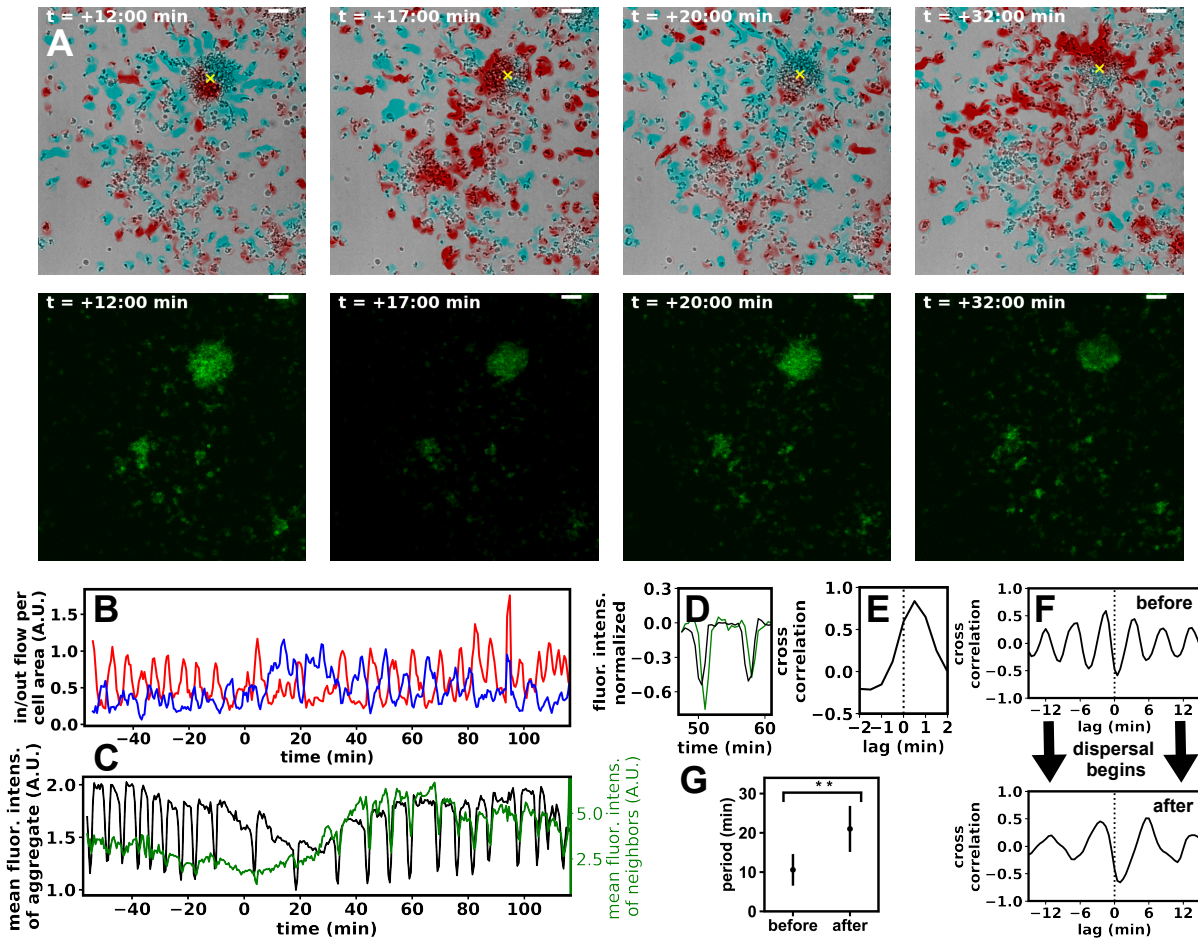


Figure 1.2. Attractant signaling of dispersing cell aggregates. [a] Micrographs of a dispersing aggregate of cells expressing Flamindo2 and the corresponding fluorescent intensity snapshots (scalebar: $50 \mu\text{m}$). [b] Inward/outward optical flow (red/blue) averaged over the ranges $60 - 120 \mu\text{m}$. [c] Mean fluorescent intensity of Flamindo2 cells, averaged over $75 - 150 \mu\text{m}$ from the aggregate center (green line) and within $20 \mu\text{m}$ from this center (black line), as a function of time. [d] As in [c], but now for $t=45-60$ min after the onset of dispersal. [e] Cross-correlation of the green and black signal in panel D, demonstrating that the change in intensity in the aggregate occurs ~ 30 s before the change in cells away from the aggregate. [f] Cross-correlation of the inward motion and the fluorescent intensity sampled $50-20$ min before the onset of dispersal (top) and $40-70$ min after the onset of dispersal (bottom). [g] Period of cAMP signaling just before and right after the onset of dispersal ($N_{agg}=14$).

inward motion (Movie S1). For this aggregate, the period of these cycles was ≈ 20 min for the first two cycles, after which it decreased to ≈ 15 min. After these cycles, at $t \approx 110$ min, dispersal ceased and inward motion became dominant again. Finally, we verified that the inward and outward motion were negatively correlated by computing the cross-correlation between the two time traces in Fig. 1.1B (Supplementary Information, Fig. 1.9A).

We next quantified the radial chemotactic index CI , defined as the ratio of radial displacement and total displacement, for all cells within the above annulus (see Methods). The results are shown in Fig. 1.1C and illustrates that the median radial CI becomes positive during outward motion. This indicates that the motion of cells during the outward cycle was overwhelmingly directed away from the aggregate. It also suggests that the observed dispersive motion is due to an outward pointing cue and not simply due to a loss of directed inward motion, which would result in randomly moving cells and a CI close to 0.

This dispersive behavior was seen for many, but not all, aggregates. Within a 1 hour time window, we found that more than half the aggregates in 6 separate experiments ($N_{aggregates} = 23$ out of 38) showed dispersal behavior after 16 hours. In 6 separate trials, we identified 38 aggregates between 16 and 17 hours after the start of the experiments. Of these aggregates, 23 showed dispersal behavior as determined using our optical flow algorithm. For the aggregates that displayed dispersal, the number of oscillations varied between 1 and 8, while maximum speeds of outwardly and inwardly moving cells were found to be in the range of $v = 16 - 22 \mu\text{m}/\text{min}$. For some aggregates, only a limited number of dispersal events was observed, after which nearby cells were moving, on average, towards the aggregate again (Movie S2). Other aggregates displayed dispersal events, after which the aggregate did not contain any more cells (Movie S3). Finally, non-dispersing aggregates displayed the usual chemotactic behavior during which cells move in a periodic fashion towards the cell aggregate.

Oscillatory dispersal is limited to small aggregates

To determine for which conditions aggregates showed oscillatory dispersal, we measured the size of aggregates that had at least three oscillations and compared this to the size of aggregates that did not show any dispersal. For this comparison, we identified movies that contained both oscillatory dispersive aggregates and non-dispersive aggregates and determined their sizes at the same time point, chosen to be the onset of dispersal. Observations at a later time point showed a decreased size of dispersing aggregates and an increased size of non-dispersing aggregates. The average size for dispersing aggregates was significantly smaller than that of non-dispersing aggregates with a median area of $7.1 (5.5-9.9) \times 10^3 \mu\text{m}^2$ vs. $20.0 (17.3-28.0) \times 10^3 \mu\text{m}^2$ ($N_{agg}=40$ vs. $N_{agg}=22$, $p<0.001$) (Fig. 1.1D).

cAMP signaling is present in aggregates

To determine whether cAMP signaling was still present during dispersal, we used cells that express Flamindo2. This marker is an indicator for cytosolic cAMP levels and the binding of cAMP to Flamindo2 causes a decrease in its fluorescence intensity [148, 149, 85]. When plated at low density, Flamindo2-expressing aggregates also showed dispersal. Specifically, 22/41 aggregates showed dispersal behavior between 16 and 17 hours after cell plating (6 separate experiments). An example is presented in Fig. 1.2A, with shows micrographs of an aggregate during two consecutive inward/outward cycles (upper row) and the corresponding fluorescent snapshots (lower row). The fluorescence intensity oscillated between high and low in a near-spatially uniform manner, indicating that the cytosolic levels of cAMP of cells in the aggregate reaches their maximum value in a near-synchronous manner (Movie S4). The dispersal is also evident from the quantification of the inward and outward flow as a function of time (Fig. 1.2B). As in Fig. 1.1B, the net motion was towards the aggregate before the onset of dispersal, after which it became overwhelmingly outwards. Here, cell motion was averaged for distances of $60 \mu\text{m}$ to $120 \mu\text{m}$ from the center of the aggregate. This outward motion clearly alternated with

inward motion for at least 8 cycles.

The fact that continued cAMP signaling was present during dispersal becomes evident when the fluorescence intensity is plotted as a function of time. This is presented in Fig. 1.2C, where we plot the average intensity for all cells that are within $20\ \mu\text{m}$ of the edge of the aggregate (black line) and for all cells at a distance between $75\ \mu\text{m}$ and $150\ \mu\text{m}$ from the center of the aggregate (green line). Clearly, periodic cAMP signaling remains present during dispersal.

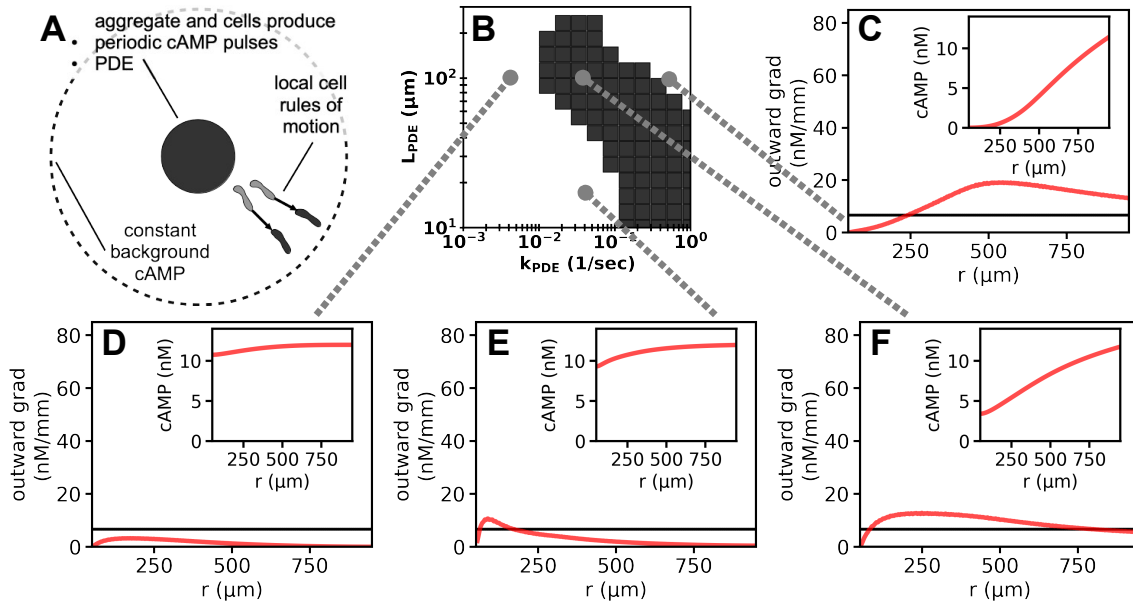


Figure 1.3. Cell dispersal model. [a] Schematic drawing of the set-up of the 2D computer simulations. A circular aggregate of fixed size ($50\ \mu\text{m}$ radius) periodically secretes cAMP signals as well as a constant amount of PDE. The computational domain had a radius of $1000\ \mu\text{m}$ and the cAMP concentration at its boundary was assumed to be constant. [b] Phase diagram for $cAMP_{back} = 12\text{nM}$ indicating parameter values for which PDE degradation resulted in dispersal. [c-f] Radial concentration gradients and corresponding profiles (inset) plotted for $LPDE = 100\ \mu\text{m}$ and $k_{PDE} = 0.6\text{s}^{-1}$ [c], $k_{PDE} = 0.04\text{s}^{-1}$ [f], and for $LPDE = 20\ \mu\text{m}$ and $k_{PDE} = 0.04\text{s}^{-1}$ [e]. The minimum gradient for direction sensing is indicated by the black line.

To determine whether it is plausible that cAMP signaling of the aggregate is driving cAMP signaling of cells outside the aggregate, we computed the cross-correlation of the fluorescent signal of the aggregate (black line in Fig. 1.2D) and the fluorescent signal of the isolated cells (green line in Fig. 1.2D). The result shows that the neighboring cells are positively correlated

with the aggregate signal with a delay of approximately 30 s (Fig. 1.2E). Computing this cross-correlation for nearby cells and for cells more distant from the aggregate shows that this delay is larger for the more distant cells, which further supports the aggregate as the driving center of signaling (Supplementary Information, Fig. 1.10). To determine whether this delay is consistent with a diffusive cAMP signal that originates at the aggregate and triggers cAMP signaling in the neighboring cells we computed the diffusive timescale. This time scale is approximately L^2/D_{cAMP} , where L is the distance to the aggregate and D_{cAMP} is the diffusion constant of cAMP. Taking $D_{cAMP} \sim 400 \mu\text{m}^2/\text{s}$ [55] and $L \sim 100\mu\text{m}$, we estimate the diffusive time delay ~ 25 s, consistent with the results from the cross-correlation.

We next determined how cAMP signaling is correlated with cell motion. For this, we computed the cross-correlation function between the fluorescence intensity and radial motion. The result reveals that the fluorescence signal was anti-correlated with inward motion, both before and after onset of dispersal (Fig. 1.2F). Specifically, the cross-correlation shows a minimum at $t \sim 30$ s, indicating that the inward motion was largest slightly after the fluorescence intensity level was lowest (corresponding to high intra-cellular cAMP levels). Since increasing intracellular levels of cAMP results in increasing extracellular levels of cAMP [76], these findings suggest that high intra-cellular cAMP leads to the formation of a gradient that is pointing towards the aggregate, resulting in directed motion towards the aggregate. We have verified that this is consistent with the cAMP signal for non-dispersing aggregates (Supplementary Information, Fig. 1.9B). This signal is clearly negatively correlated with inward motion, indicating that the cAMP signal results in significant cAMP concentration levels away from the aggregate and generates an inward-pointing gradient during high levels of intra-cellular cAMP.

The period of cAMP signaling significantly increases at onset of dispersal

Fig. 1.2C also shows that the period following the onset of dispersal is significantly increased. To determine whether this increase occurred for all dispersing aggregates, we computed the period of cAMP oscillations as a function of oscillation number. We then compared the

average period for the two oscillations preceding dispersal and the two following dispersal. The average period increased from $T=10\pm 4$ min to $T=21\pm 6$ min ($p=0.002$, $N_{agg}=14$; Fig. 1.2G) and we observed that no aggregates exhibited dispersal behavior while pulsing regularly at short periods. Furthermore, the ratio of these two periods was computed to be 2.1 ± 1.4 , corresponding to a more than doubling in cAMP signaling period and suggesting the possibility that the central oscillator somehow skips beats. This doubling of period was observed in non-dispersing aggregates, indicating that an increase of cAMP signaling period is required for dispersal.

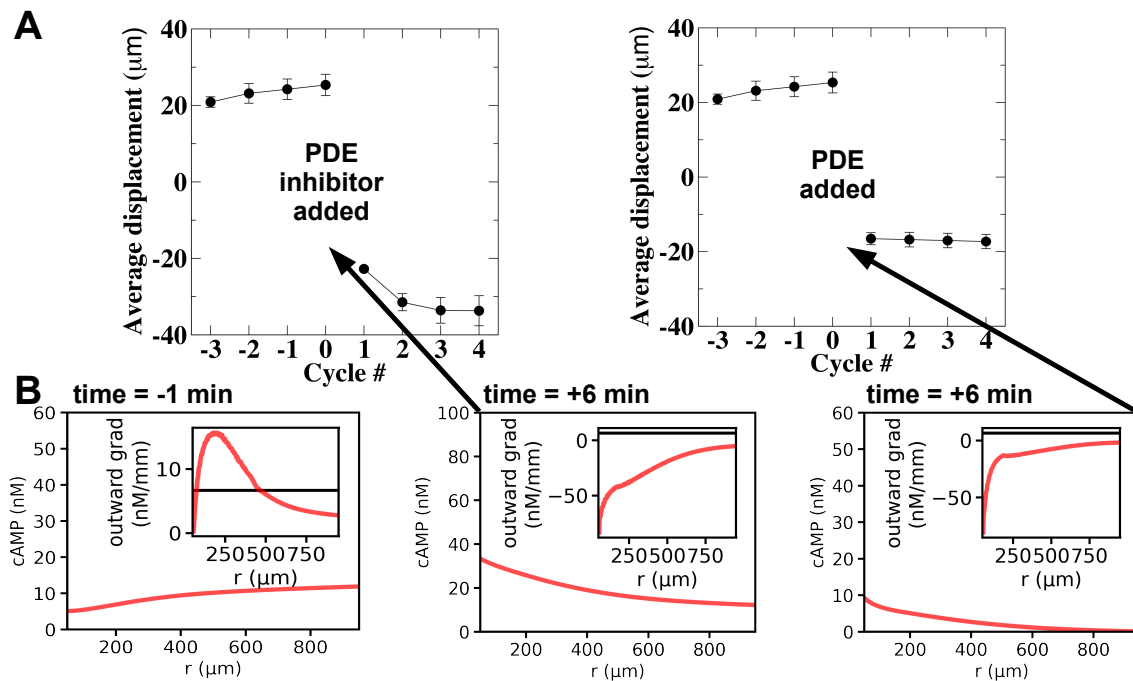


Figure 1.4. Predictions of chemical intervention. [a] Net cell motion during a cAMP cycle ($T=10$ s) in response to the global addition of a PDE inhibitor (left) and of PDE (right). [b] Radial cAMP concentration profiles and outward cAMP gradient (inset) are shown at 1 min before (left) and 6 min after the simulated addition of the inhibitor and PDE (middle/right).

Computer simulations support PDE-mediated degradation can cause dispersal

Our experimental results show that dispersal is oscillatory, can last several periods, and can affect cells as far as $400 \mu\text{m}$ away from the aggregate. Furthermore, the onset of dispersal coincides with an increase of the cAMP period. We hypothesized that the competition between

the periodic cAMP source from the aggregate and the PDE gradient that is pointing towards the aggregate may be responsible for the observed reversal in directed motion. For small values of PDE degradation and small cAMP periods, the cAMP gradient would be directed towards the aggregate. For high values of PDE degradation and large cAMP periods, however, cAMP near the aggregate could be sufficiently degraded to form an outward cAMP gradient and cause cell movement away from the aggregate.

To investigate this possible mechanism, we constructed a mathematical model that describes the production and diffusion of cAMP and PDE (see, Fig. 1.3A Methods and, for a more detailed description, Supplementary Information). The model contains an aggregate of fixed size and a variable number of individual cells randomly placed away from the aggregate. Key parameters in the model are the degradation constant of cAMP due to PDE, k_{PDE} , the lengthscale L_{PDE} of the PDE profile, and the cAMP concentration far from the aggregate, $cAMP_{back}$. Cell motion, defined as positive/negative for outward/inward radial motion, was determined by the gradient of cAMP and motion was considered possible only if cAMP gradients exceeded a threshold, based on earlier studies [195] (see Methods). In our simulations, we varied k_{PDE} , L_{PDE} and $cAMP_{back}$. Other fixed parameters are listed in Supplementary Information, Table 1.1.

Motivated by our experimental results, we determined the direction of migration in simulations in which the cAMP period abruptly increased from 10 min to 21 min. Using these results, we constructed phase diagrams in the (k_{PDE}, L_{PDE}) space, determining which parameter values resulted in dispersal. Dispersal was deemed to be present when all cells displayed net outward motion during the 21 min cAMP period (see Methods). In Fig. 1.3B we have indicated the region in phase space which resulted in dispersal for $cAMP_{back} = 12\text{nM}$. For values of parameters that are outside this region, cells did not show dispersal. A snapshot and movie of a typical simulation are presented in Supplementary Information, Fig. 1.11 and Movie S5, respectively. Dispersal also occurred when we doubled the number or changed initial distance to the aggregate of the individual cells.

To understand why certain parameter values did or did not result in dispersal, we examined

the cAMP concentration gradient 9 min after the start of the $T = 21$ min cycle. Examples of these gradients, averaged over the azimuthal direction and corresponding to parameter values indicated by dots in Fig. 1.3B, are plotted in Figure 1.3C-F. For the profile corresponding to successful dispersal the gradient ($L_{PDE} = 100\mu\text{m}$ and $k_{PDE} = 0.04\text{ s}^{-1}$, Fig. 1.3F) is clearly pointing outward and the gradient exceeds the critical threshold, indicated by a horizontal line, in a domain that extends a significant distance from the aggregate. For other values of the parameters, the gradient is too shallow either close to the aggregate (Figure 1.3C), in the entire domain (Figure 1.3D), or away from the aggregate (Figure 1.3E).

Since the number of cells in the aggregate is much larger than 1, it is possible to simplify the 2D model to a computationally more amenable 1D model. In this model, secretion of cAMP and PDE by individual cells are ignored, the cAMP concentration is computed along a radial line, and the PDE profile is given by its steady-state solution (see Supplementary Information for details). We have verified that the phase diagram obtained from the 1D model is qualitatively similar to the one from the full 2D model (Supplementary Information, Fig. 1.12A). Using this simplified model, we have determined that reducing the computational domain to $500\mu\text{m}$ and the background concentration to 6 nM also results in a qualitatively similar phase diagram (Supplementary Information, Fig. 1.12B). Furthermore, we used the 1D model to determine the dispersal domain in phase space as a function of the background concentration and found that below a minimum value of $cAMP_{back}$, approximately 4nM, successful dispersal was not possible (Supplementary Information, Fig. 1.13).

Predictions from computer simulations

The computer simulations show that a dynamic competition between PDE and cAMP signaling can result in outwardly directed motion. The model can generate several distinct and clear predictions by altering the PDE profile, and thus the cAMP concentration, in simulations. In one set of simulations, we considered the effect of globally adding a PDE inhibitor. The outcome of this simulation is shown in the left panel of Fig. 1.4A, where we plot the net displacement of

the individual cells per cAMP cycle before (cycle -4-0) and after the global addition of a PDE inhibitor (cycle 1-4) (see also Movie S6). We considered model parameters to be within the dispersal region of Fig. 1.4B ($cAMP_{back}=12\text{nM}$, $L_{PDE} = 100\mu\text{m}$, $k_{PDE} = 0.04\text{s}^{-1}$). Therefore, the cAMP gradient right before the addition of PDE was pointed away from the aggregate resulting in cell motion directed away from the aggregate (left panel Fig. 1.4B). The addition of the inhibitor was modeled by setting $k_{PDE} = 0$ at the start of cycle #1 while the cAMP signaling of the aggregate was assumed to continue (see below for experimental verification). The addition of the inhibitor changed the sign of the gradient (middle panel Fig. 1.4B), resulting in net motion towards the aggregate. Thus, our simulations predict that dispersing aggregates can become non-dispersing following the global addition of a PDE inhibitor.

Another set of simulations examined the effect of globally adding PDE. For this, we again started with the dispersing aggregate described above and set the cAMP concentration to zero everywhere after cycle 0 while the aggregate continued to secrete cAMP in an oscillatory fashion. The net displacement of the cells in this simulation is shown in the right panel of Fig. 1.4A while the resulting cAMP profile and gradient are plotted in the right panel of Fig. 1.4B (see also Movie S7). Immediately following the resetting of cAMP to 0, the concentration profile changed and the gradient points towards the aggregate, resulting in inward motion (negative CI; right panel Fig. 1.4A). Raising the PDE levels to high uniform values at the start of cycle #1 ($\sim 5 \times$ the value at the aggregate) also resulted in the abolishment of dispersal. Thus, a second prediction is that dispersing aggregates can also become non-dispersing after the global addition of PDE.

Dispersal from medium aspiration experiment shows effect of medium

Our computer simulations show that PDE, an extracellular inhibitor for cAMP, can be responsible for the observed dispersal. To test this, we identified dispersing aggregates and aspirated a small amount of medium near these aggregates during dispersal. This medium was then rapidly introduced close to a non-dispersing aggregate using a micropipette, and the shedding

angle of dispersing cells was quantified (see Methods). We found that this aspiration experiment rendered the previously non-dispersing aggregate into a dispersing one (Fig. 1.5A; $N_{agg}=3$). Furthermore, analysis of individual cell tracks revealed that cells were primarily directed away from the needle tip, according to Kuiper's test against a uniform distribution ($N_{cell}=26$, $p < 0.05$). This is shown in the inset of Fig. 1.5A, where we have plotted the frequency of cell motion in each of the 4 quadrants centered around the pipette tip. The average chemotactic index directed away from the pipette tip was computed to be $\langle CI \rangle = 0.8$. As a control, we verified that aspiration of medium far from any aggregate did not result in statistically significant motion away from the tip when this medium was deposited within $10 \mu\text{m}$ of a non-dispersing aggregate. In addition, when depositing medium obtained from a non-dispersing aggregate near another non-dispersing aggregate, it did not result in movement directed away from the tip. These experiments point to a role of the medium in the onset of dispersal.

DTT can abolish dispersal

To test our first modeling prediction, that PDE inhibition can reverse the directed motion of cells near dispersing aggregates, we identified dispersing aggregates and deposited a small amount of DTT onto them using a pipette. DTT is a known inhibitor of the activity of PDE1, which dominates extracellular cAMP degradation during the aggregation phase of *Dictyostelium* [8]. The addition of DTT ceased outward cell motion, which then was followed by inward cell motion, as shown in the snapshots of Fig. 1.5B&C. This was further quantified by computing the average inward and outward flow, which clearly shows that DTT suppressed dispersal and increased inward motion (Fig. 1.5D). These results were obtained for all analyzed aggregates ($N_{agg}=23$) and indicate that blocking of PDE activity abolished outward motion but not inward motion. Importantly, the addition of DTT did not abolish the signaling of the aggregate, as shown by plotting the Flamingo2 fluorescence intensity as a function of time before and after the addition of DTT (Fig. 1.5E). Thus, the assumption of our predictive simulations, that signaling continues after the modification, is valid.

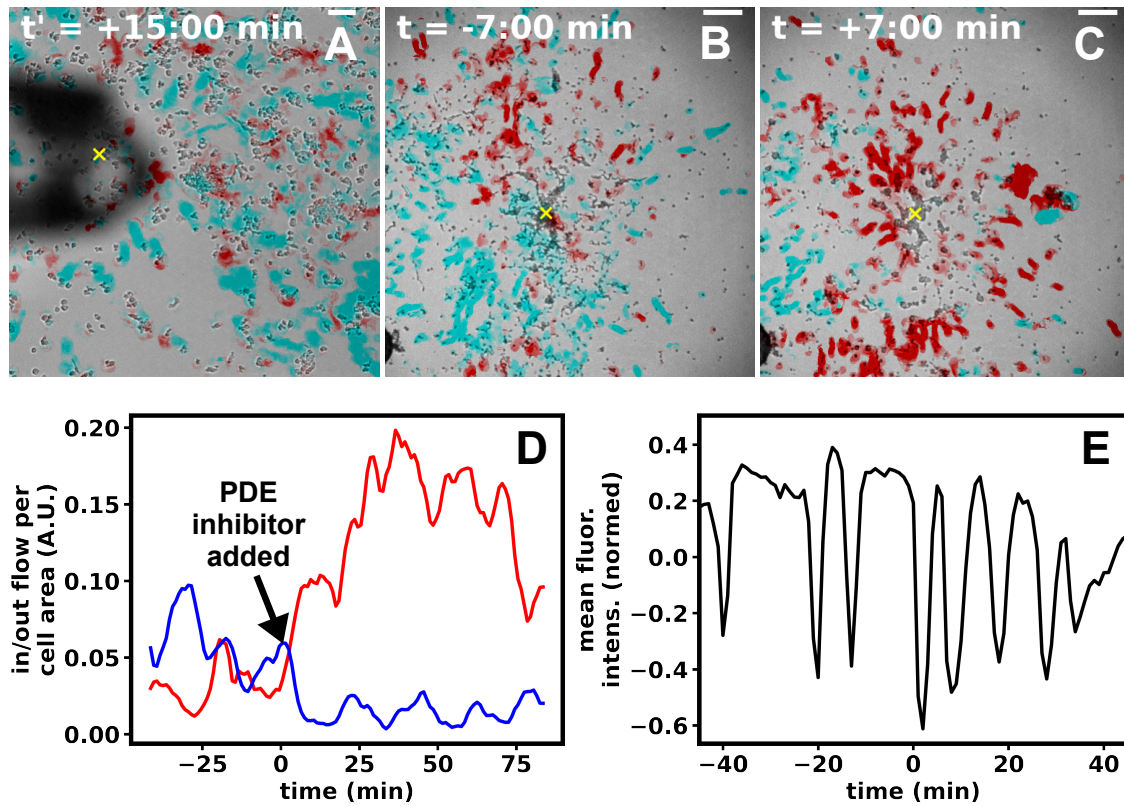


Figure 1.5. Effect of chemical intervention. [a] Micrograph of a previously non-dispersing aggregate after exposure to medium transferred from an aggregate that was dispersing. Motion is visualized using dense optical flow with blue/red corresponding to motion away from/towards the transferred fluid (yellow 'x'). The inset shows the frequency of mean radial cell directions in each of the four quadrants relative to the pipette tip. (scale bar: $50 \mu\text{m}$). [b,c] Micrographs 7 min before [b] and 7 min after [c] the addition of DTT at $t = 0$. Cell motion was calculated by dense optical flow inward/outward from the aggregate (yellow 'x'). (scale bar: $50 \mu\text{m}$). [d] Average inward/outward cell motion (red/blue) in response to DTT introduced at $t = 0$. [e] Mean Flamindo2 fluorescent intensity of the aggregate versus time in response to DTT introduced at $t = 0$.

Addition of PDE abolishes dispersal

To test the prediction that the global addition of PDE can alter the dispersing behavior of aggregates, we added PDE1 to aggregates. Fig. 1.6A&B show two micrographs before and after the introduction of PDE1 onto a dispersing aggregate. Before PDE1 introduction, at $t=0$, the aggregate shows oscillatory dispersal. After adding PDE1, dispersal was abolished and inward motion was dominant. This is quantified in Fig. 1.6C where we plot the inward and outward motion as a function of time. This behavior was consistent in all aggregates $N_{agg}=21$ we analyzed. The *Flamindo2* intensity of both the aggregate and neighboring cells increased sharply following the exposure to PDE1, indicating the intracellular cAMP concentration decreases. After a delay, cAMP signaling resumed (Fig. 1.6D), again validating our modeling assumption. We also verified that dispersal was not abolished in the control experiment, in which we deposited solution without PDE onto the aggregate.

Discussion

In this report, we showed that aggregates of *Dictyostelium* cells can display a dramatic reversal in directed motion in which cells move *away*, rather than towards the cluster of cells. This dispersal was often present in the form of cycles of alternating inward and outward motion and was only seen for small-sized aggregates. Furthermore, we established that cAMP signaling remained present during the dispersal phase and that the period of cAMP signaling approximately doubled at the onset of dispersal. Using mathematical modeling, we showed that the competition between the secretion of cAMP and a steady state profile of PDE, the inhibitor of cAMP, can be responsible for the observed dispersal. We showed that if PDE exhibits a spatial profile such that its concentration near the aggregate is higher than further away, it can create an outwardly pointing gradient capable of supporting dispersal. Our experiments showed that the medium plays an essential role in the aggregate dispersal: the introduction of an aspartate taken during the dispersal phase of an aggregate, which presumably contains little cAMP and an abundance

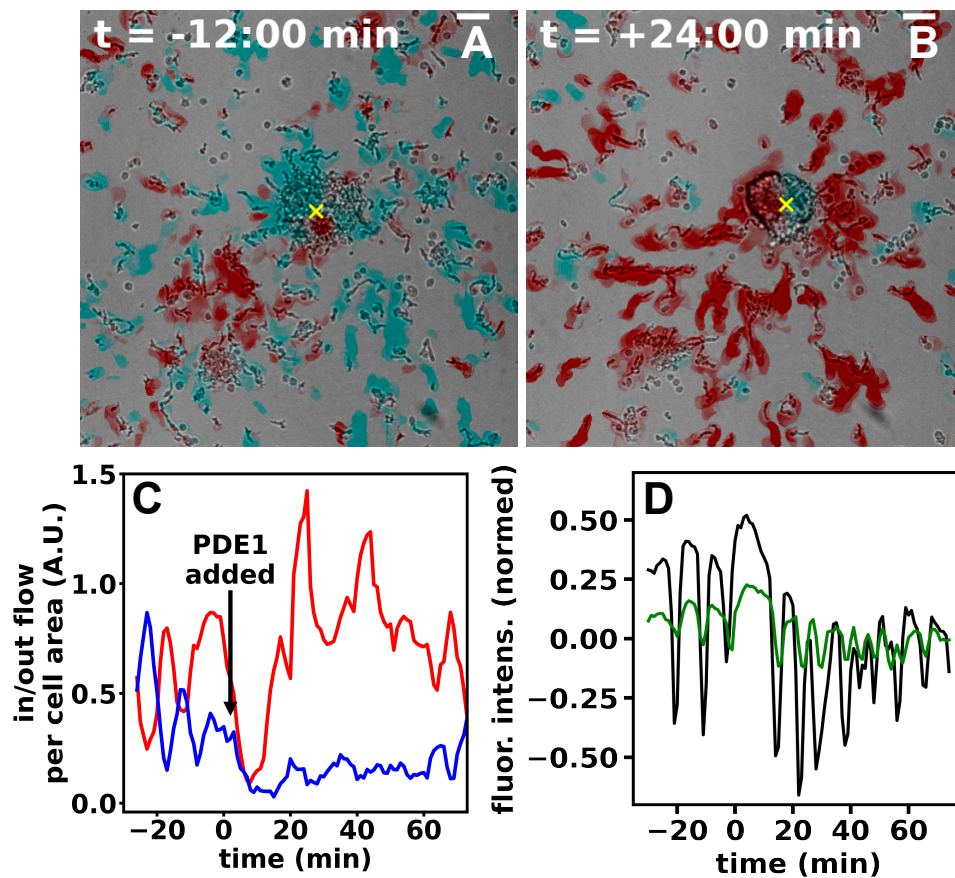


Figure 1.6. Effect of chemical intervention (cont'd). [a-b] Micrographs of an initially dispersing aggregate $t = -14$ min before the addition of PDE1 [a] and $t = +14$ min after the addition of PDE1 [b] (scale bar: $50 \mu\text{m}$). [c] Inward/outward (red/blue) optical flow averaged for cells 80-160 microns away from the aggregate center. PDE1 was added at $t = 0$. (D) Total Flamindo2 fluorescent intensity, computed using a 5 min moving average, for cells inside the aggregate (black) and cells 80-160 microns away from the aggregate center (green).

of PDE, rendered a previously non-dispersing aggregate into a dispersing one. Obviously, this experiment does not rule out the possibility that the medium contains a chemorepellent. Identifying such a repellent, however, is not feasible since the medium contains hundreds of different proteins. In addition, and predicted by our simulations, our experiments show the abolishment of dispersal following the addition of PDE or a PDE inhibitor.

Essential in the proposed mechanism is the temporal signaling of secreted cAMP of the aggregate. We found that the period of this signaling increases abruptly at the onset of dispersal from approximately 10 min to 21 min. Earlier studies have shown that *Dictyostelium* cells exhibit a cellular memory and can continue to move in the original direction, even after a gradient reversal [192, 145]. These studies showed that cells are able to respond to very shallow gradients, after having been exposed to waves with amplitudes on the order of $1 \mu\text{M}$ and that this memory is effective for cAMP waves with periods up to 10 min but that this memory breaks down for larger periods. This suggests that cellular memory before the onset of dispersal prevents outward cell motion. Following the period doubling, however, cellular memory will have dissipated and the outwardly pointing gradient can become steep enough to guide cells *away* from the aggregate, resulting in the observed dispersal. We should note that it is not clear at the moment what causes this increase in periodicity of cAMP signaling. Earlier perfusion chamber experiments have shown that the frequency of cAMP signaling increases for increasing cell density or decreasing cAMP dilution [81]. This increase, however, is gradual and not sudden. This suggests that unknown feedback mechanisms or bistabilities, perhaps through cell counting factors, may be at play during the aggregation process and are responsible for the observed sudden shift in frequency.

The critical parameters in our proposed mechanism are the signaling period, the degradation constant of cAMP, the length scale of the spatial profile of PDE, and the background concentration of cAMP. Our modeling shows that there exists a region in (L_{PDE}, k_{PDE}) parameter space for which dispersion is possible. For these parameter values, the cAMP gradient is pointing outward and exceeding the critical sensitivity threshold within a sufficiently large annulus. For

parameter values outside this region, the reversed gradient is either too small for reversed motion or is only significant close to the aggregate. For example, making the degradation constant too large will result in a very shallow gradient near the aggregate while making it too small will lead to gradients that are below the threshold for the entire domain. We should point out that in the limit of no degradation, the cAMP gradient will always point toward the aggregate as long as it continues to secrete cAMP in an oscillatory manner. Likewise, in the limit of an infinite PDE length scale, corresponding to uniform degradation, the cAMP gradient will also always point towards the aggregate throughout the entire signaling cycle. Finally, for very small PDE length scales, degradation is only significant very close to the aggregate and the gradient will not be steep enough to direct dispersal further away from the aggregate. This means that a PDE that is exclusively bound to the membrane is unlikely to be responsible for the observed dispersal.

Similar qualitative arguments can be made for the necessity of a minimum value of $cAMP_{back}$. Values for $cAMP_{back}$ that are below this minimum value will result in reversed gradients that are too small to be detected. Our model predicts that for values of $cAMP_{back}$ smaller than 4nM it is not possible to achieve dispersal. Consistent with this result, our experiments show that the introduction of PDE abolished dispersal. This can be understood by realizing that PDE will not only reduce the cAMP concentration close to but also far away from the aggregate. Therefore, the introduction of PDE will reduce $cAMP_{back}$, which means that outward gradients are no longer sufficient to generate dispersal movement.

Although the precise parameter values that allow for dispersal depend on the details of the model, it is still useful to examine whether the observed range is physiologically relevant. For the diffusion coefficient of PDE we can take $D_{PDE} \sim 10\mu m^2/s$, a value typical for a Brownian particle with an effective radius roughly 10 times larger than that of cAMP. In addition, as in a previous study, we can take as an upper limit for its decay rate the value of a typical extracellular protein: $K_{PDE} \sim 10^{-4}s^{-1}$ [132, 13]. This results in a maximal length scale on the order of $L_{PDE} = \sqrt{D_{PDE}/K_{PDE}} \sim 10^2 \mu m$. Note that the actual decay rate may be larger and the length scale smaller, since PDE is inhibited by a secreted inhibitor, PDI [75]. Furthermore, some of the

PDE is membrane bound, further reducing the length scale. Thus, our values of L_{PDE} for which the model displays dispersal ($< 100\mu\text{m}$) appear to be within the physiological range. Previously model values of the cAMP degradation rate due to the presence of PDE are in the range of $k_{PDE} \sim 0.04 - 0.2 \text{ s}^{-1}$ [131, 132]. In these studies, the PDE concentration was normalized by the Michaelis constant. The experimentally determined half-life of cAMP in a suspension of 10^8 cells/ml at a concentration of $1 \mu\text{M}$ was found to be approximately 60s, resulting in a degradation rate, normalized by the PDE concentration, of approximately 0.02 s^{-1} . Our PDE concentration is normalized by the value at the aggregate, which makes it difficult to estimate the precise degradation constant. However, assuming that this value is not significantly different from the PDE concentration in the suspension experiment or from the Michaelis constant, we can conclude that the dispersal range found in our model ($k_{PDE} > 0.01\text{s}^{-1}$) is physiologically relevant. Finally, our model shows that dispersal is only possible if the background cAMP concentration is above a critical value that we estimate to be around 3nM. This value is comparable to the estimated value found in experiments (10nM) and is thus also in the physiological range [203]. A non-zero background value can be explained in our experiments by realizing that the petri dish contains a large number of aggregates, each secreting cAMP, resulting in elevated cAMP levels away from the dispersing aggregate.

Although our 2D model is conceptually simple, it captures the salient features of cAMP signaling, diffusion and degradation and we do not expect that the qualitative findings will change in a significant manner if the details of the model are developed. In our simulations, we have taken a specific form of the secretion dynamics, based on earlier modeling studies [131]. However, we have verified that the precise dynamics of the secretion dynamics does not affect that qualitative results. For example, simulations with different pulse shapes, including sinusoidal, block-shaped and Gaussian ones, gave qualitatively identical results. Furthermore, we have implemented very simple cell motion rules requiring cells to take on one of three motility states (towards or away from the aggregate or not moving at all). In reality, the response of cells is more complicated than this ternary rule and may include randomness, speeds that depend on

the gradient steepness, and cellular memory. Implementing these more complex rules, however, are not expected to alter the qualitative conclusions. Our modeling also shows that a further simplification to a 1D model, which only considers cAMP secretion from the aggregate and assumes a steady state profile of PDE, is able to reproduce the essential features of our proposed mechanism. This can be explained by realizing that the cell density of the aggregate is much higher than the density of freely moving cells. Our model assumes a steady state profile of PDE, which is consistent with experimental work that showed that the secretion rate of PDE is constant in time [78].

The mechanism we propose is an example of a self-generated chemotactic gradient [142, 205, 206]. This type of gradient has been observed before for chemoattractant sources that are time-independent. For example, a study showed that a linear gradient can be established in the zebrafish posterior lateral line primordium through spatially asymmetric sequestration and internalization [210, 52]. In this case, the established gradient is linear, resulting in motion that is persistently directed. Another example involves vegetative *Dictyostelium* cells placed in a uniform concentration of folate. These cells can break down folate through secreted and cell-surface folate deaminase [154]. As a result, a high cell density region creates a local reduction of folate and thus a self-generated gradient, as also verified in a computational model [205]. Finally, a recent study demonstrated that *Dictyostelium* cell can create self-generated chemoattractant gradients that allow them to navigate complex paths with great efficiency [206]. Our results show that self-generated gradients can also play a significant role when the chemoattractant source is time dependent and can even result in surprising dispersal behavior.

Intriguingly, the aggregates that display dispersal are significantly smaller than aggregates that continue to accrue neighboring cells Fig. 1.1D. This raises the possibility that the dispersal mechanism is a protection against the formation of aggregates that are too small to continue along a viable developmental path, since a aggregate that is too small will not be able to form a fully developed fruiting body structure. Our dispersal can thus be considered as an example of quorum sensing, which plays a role in a large number of biological systems [183]. Quorum

sensing has also been demonstrated in *Dictyostelium* cells where, in the vegetative stage, the AprA-CfaD complex works as a chemorepellent and limits the cell proliferation by negative feedback control [22, 9] while in the developed stage the secreted protein counting factor limits the size of the aggregates [21, 23, 24]. We have verified, however, that aggregates of mutant cells lacking these quorum sensing proteins (specifically, AprA, CF50, CfaD, and CtnA) were still able to display dispersal (Supplementary Information and Movie S8). This further points towards the competition between cAMP secretion and PDE-mediated degradation as a mechanism for the observed dispersal.

1.1 Supplementary Information

Image analysis

Our measure of positive/outward/blue and negative/inward/red average cell motion was computed from differential interference contrast (DIC) microscopy. The raw DIC values were first normalized by subtracting the background and scaling the absolute remainder to unity. Then, edges were detected using a Scharr filtration. We decided against filling in the edges before computing dense optical flow, since most filling transforms proved to be unreliable in filling the same regions consistently between frames. By not filling in the edges, the stability of the resulting signals improved.

We determined the locations of cells using two consecutive binarized images that are separated by a time interval $\Delta t > 0$ such that

$$l_t(x,y) = \begin{cases} 1, & \text{if at time } t, (x,y) \text{ contains cell(s)} \\ 0, & \text{otherwise} \end{cases} \quad (1.1)$$

$$l_{t+\Delta t}(x,y) = \begin{cases} 1, & \text{if at time } t + \Delta t, (x,y) \text{ contains cell(s)} \\ 0, & \text{otherwise} \end{cases} \quad (1.2)$$

Thus, the total cross sectional area of a cell at time t is given by the integral over space of the mask $l_t(x,y)$ taken to be $\int \int l_t(x,y) dx dy$. In order to increase stability in the cell displacement field, we employed a mask consisting of a blurred average cell location given by

$$l'(x,y) = \frac{1}{\sqrt{2\pi}\sigma} \exp\left(-\frac{1}{2} \left(\frac{l_{t+\Delta t/2}(x,y)}{\sigma}\right)^2\right) \quad (1.3)$$

where $l_{t+\Delta t/2}(x,y) = \min(l_t + l_{t+\Delta t}, 1)$ and where $\sigma > 0$ is the width of the Gaussian blurring. We checked that results were not sensitive to our choice of σ as long as it is sufficiently small. We assigned a value of $\sigma = 3\mu m$ in our analyses. This blurred mask is the reason for the ‘‘blob’’

effect observed in our images highlighting the inward/outward motion of cells (Fig. 1 and 2).

We defined the displacement field, $\vec{u}(x,y) = (u_x(x,y), u_y(x,y))$, to be the one that minimizes the following sum of squared differences

$$\vec{u}(x,y) = \operatorname{argmin}_{(u_x(x,y), u_y(x,y))} \int \int [l_{t+\Delta t}(x,y) - l_t(x + u_x(x,y), y + u_y(x,y))]^2 dx dy \quad (1.4)$$

The numerical method used to compute $\vec{u}(x,y)$ in this work was the Dense Inverse Search optical flow method [110]. To avoid destroying information used in the dense optical flow procedure, this blurred mask was not applied until after the raw displacement field, $\vec{u}(x,y)$, was computed. After computing the displacement field, we computed the corresponding velocity field according to, $\vec{v}(x,y) = \vec{u}(x,y)/\Delta t$. The time interval Δt used in our analysis was determined by the frame rate and was in the range of 10-60s.

2D model

Our computational model is solved in a 2D circular domain with radius r_{max} (See Fig. 1). This domain contains a circular, fixed aggregate with radius r_0 and N_{cell} individual cells outside this aggregate. The cAMP concentration, $cAMP$, and PDE concentration, PDE , obey the reaction-diffusion equations with diffusion constants D_{cAMP} and D_{PDE} , respectively. The diffusion coefficient of cAMP was taken to be $D_{cAMP} \sim 400 \mu m^2/s$ [55] while the diffusion coefficient of PDE ($D_{PDE} \sim 10 \mu m^2/s$) was taken as a value typical for a Brownian particle with a effective radius roughly 10 times larger than that of cAMP. The aggregate secretes cAMP and PDE at a constant rate as well as cAMP in an oscillatory fashion, incorporated by imposing a time-varying flux at the boundary of the aggregate. Individual cells also secrete cAMP and PDE, further detailed below. cAMP is degraded through PDE while PDE degrades at a constant rate.

Since traditional finite difference methods are not able to handle curved boundaries, we utilized the phase-field method to numerically solve the system. This method, traditionally used

to solve a variety of free boundary problems, can also be applied to tackle diffusional problems in stationary but complicated geometries [108, 64, 117] and offers an accurate, computationally inexpensive method that can be implemented with ease. In this approach, an auxiliary field, ϕ , is introduced that locates the interface and that is coupled to the other physical fields through an appropriate set of partial differential equations. The phase field ϕ for our geometry is chosen to have the form

$$\phi(r) = \frac{1}{2} - \frac{1}{2} \tanh((r_0 - r)/\xi) \quad r < r_{max}/2 \quad (1.5)$$

$$\phi(r) = \frac{1}{2} + \frac{1}{2} \tanh((r_{max} - r)/\xi) \quad r > r_{max}/2 \quad (1.6)$$

Thus, the phase field has the value 1 inside the annular-shaped computational domain, 0 outside the domain and inside the aggregate, and varies between these two values across a diffusive boundary layer of thickness ξ , taken to be much smaller than r_0 . The aggregate boundary and the domain boundary are identified by $\phi = 1/2$. One can show that in the limit of $\xi \rightarrow 0$, appropriate boundary conditions can be recovered [108].

The cAMP concentration is obtained by solving the following reaction-diffusion equation:

$$\frac{\partial cAMP}{\partial t} = D_{cAMP} \frac{\vec{\nabla} \cdot [\phi \vec{\nabla} cAMP]}{\phi} - k_{PDE} PDE_{cAMP} + F_{cAMP} \frac{(\vec{\nabla} \phi)^2}{K\phi} \quad (1.7)$$

while the equation for the PDE concentration is written as:

$$\frac{\partial PDE}{\partial t} = D_{PDE} \frac{\vec{\nabla} \cdot [\phi \vec{\nabla} PDE]}{\phi} - K_{PDE} PDE + F_{PDE} \frac{(\vec{\nabla} \phi)^2}{K\phi} \quad (1.8)$$

In these equations, the second terms describe the degradation of cAMP by PDE (normalized as explained below) with rate k_{PDE} , and the self-degradation by PDE, with rate K_{PDE} . The last terms in the reaction-diffusion equations represent the flux boundary conditions for cAMP and PDE at the aggregate. In these terms, K is a normalization constant which depends on

the area $L = 2\pi r_0$ of the membrane: $K = \int d\vec{x} (\vec{\nabla}\phi)^2/L$ [117]. In our model, the aggregate secretes cAMP in an oscillatory fashion, with dynamics that are given by the Martiel-Goldbeter model (see below) [131]. Thus, the cAMP flux is time varying and the appropriate boundary condition at the aggregate boundary corresponds to $D_{cAMP} \frac{\partial cAMP(r_0)}{\partial r} = F_{cAMP}(t)$. The secretion of PDE is assumed to occur at a constant rate F_{PDE} . As boundary condition at $r = r_{max}$, we take $PDE(r_{max}) = 0$ and $cAMP(r_{max}) = cAMP_{back}$.

In addition to the aggregate, we also placed N_{cell} individual cells at random locations outside the aggregate. We assumed that each individual cell is secreting cAMP following the Martiel-Goldbeter model, together with a constant amount of PDE, and that each individual cell secretes the same amount as a cell within the aggregate. Therefore, the ratio of the flux parameters for the single cell and for the aggregate is identical to the reciprocal of the number of cells in the aggregate. To estimate the number of cells in an aggregate, we constructed z-stacks using confocal microscopy (Fig. 1.7). The aggregates were roughly cylindrical in shape and our measurements found that the height was $39.5 \pm 5.9 \mu\text{m}$ and the radius was $38.0 \pm 20.0 \mu\text{m}$ ($N=39$ aggregates). Therefore, the volume was estimated to be approximately $2 \times 10^5 \mu\text{m}^3$. Earlier work showed that a typical *Dictyostelium* cell has a volume of roughly $500 \mu\text{m}^3$ [28], leading to an estimate of the number of cells in an aggregate of around 400. Thus, a single cell secretes $1/400^{th}$ of the amount secreted by the aggregate.

The main text shows results where $N = 100$ particles were placed in an annulus with radii $150 \mu\text{m}$ and $350 \mu\text{m}$. These numbers were motivated by manual counting of the number of cells before dispersal in our experiments. We have verified that increasing this number by several fold or by increasing the outer radius of the annulus did not affect the qualitative results of our simulations. To mimic cAMP relay, we started the cAMP pulse for each pulse when the temporal gradient of the local cAMP concentration exceeded a critical value, chosen here to be 0.1 nM/s . However, we have verified that choosing this onset contemporaneous with the aggregate pulse did not change the qualitative picture.

Since dispersal occurs many hours into the experiments, we used as initial condition for

PDE the spatial profile obtained by solving the PDE diffusion equation for 60 minutes in the presence of the aggregate (secreting PDE at a constant rate F_{PDE}) but in the absence of individual cells. In this time period, the PDE profile has reached its equilibrium value for typical parameter values. To determine the constant secretion rate, we note that the analytic steady-state solution, given by

$$PDE(r) = PDE_{max} \frac{K_0(r/L_{PDE})}{K_0(r_0/L_{PDE})}, \quad (1.9)$$

is a good approximation of the resulting solution. Here, PDE_{max} is the concentration of PDE at the edge of the aggregate and $K_0(x)$ is the modified Bessel function of the second kind of order zero, and $L_{PDE} = \sqrt{D_{PDE}/K_{PDE}}$ is the length scale of the PDE profile. The boundary condition at the aggregate for this solution reads $D_{PDE} \frac{\partial PDE}{\partial r} = -D_{PDE} PDE_{max} \frac{K_1(r_0/L_{PDE})}{K_0(r_0/L_{PDE})} = -F_{PDE}$. For simplicity, we will set $PDE_{max} = 1$ and, thus, this condition will give us a value for the PDE flux rate F_{PDE} for each value of L_{PDE} . Using this flux value, we then solved the PDE equation and used this as our initial conditions.

The reaction-diffusion equations Eqns. 1.7 and 1.8 were solved on a 1000x1000 regular square grid using an alternating-direction method, employing a spatial discretization of $\Delta x = 2\mu\text{m}$ and a timestep of $\Delta t = 1\text{s}$. Other parameter values are given in Table 1.1. Following Dallon and Othmer [48] we model individual cell secretion by simply adding cAMP and PDE to the grid point closest to the location of the cell. For the determination of the phase diagram in Fig. 3, we computed the motion of the individual cells during the second pulse generated by the aggregate. At each timestep, the particle either moves inward, outward, or not at all. The rules of motion are given in the main text and involve a minimum steepness of the local cAMP gradient below which the particle does not move. A cluster was considered to be dispersing if, during a full cAMP period, all particles moved outwards.

Reduction to 1D

The fact that the number of cells within the aggregate is large allows us to simplify our 2D model. Specifically, since the aggregate dominates the cAMP as well as the PDE dynamics, we can safely ignore any secretion from individual cells. Furthermore, we can use the analytic steady-state approximation for the PDE given in Eq. 1.9 (with $PDE_{max} = 1$). These simplifications result in a problem with rotational symmetry and we can reduce our model to a 1D version, were solved along a line representing the radial direction:

$$\frac{\partial cAMP}{\partial t} = \frac{D_{cAMP}}{r} \frac{\partial}{\partial r} \left(r \frac{\partial cAMP}{\partial r} \right) - k_{PDE} PDE_{cAMP} \quad (1.10)$$

along with the appropriate boundary conditions. To determine the direction of motion of cells, we seeded the computational domain with virtual particles. Motion was determined by the local gradient, using the same rules as for the 2D model.

cAMP Signaling Model

The cAMP flux was computed using the Martiel and Goldbeter model for cAMP signaling, using the original parameters used to generate Fig. 2 in Ref. [131], which are reproduced in Table 1.2. Full details can also be found in the original study [131]. Briefly, the model describes the concentration of extracellular cAMP $\gamma(t)$, the concentration of intracellular cAMP $\beta(t)$, and the fraction of active chemoattractant receptors $\rho_T(t)$ by the following equations:

$$\begin{aligned} \frac{d\gamma(t)}{dt} &= k_i \rho_V \beta(t) - k_e \gamma(t) \\ \frac{d\beta(t)}{dt} &= q \sigma \Phi(\rho_T(t), \gamma(t)) - (k_i + k_t) \beta(t) \\ \frac{d\rho_T(t)}{dt} &= (1 - \rho_T(t)) f_2(\gamma(t)) - \rho_T(t) f_1(\gamma(t)), \end{aligned} \quad (1.11)$$

where

$$f_1(\gamma) = \frac{k_1 + k_2\gamma}{1 + \gamma} \quad f_2(\gamma) = \frac{k_1L_1 + k_2L_2c\gamma}{1 + c\gamma},$$

and where

$$\Phi(\rho_T, \gamma) = \frac{\alpha(\lambda\theta + \varepsilon Y^2)}{1 + \alpha\theta + \varepsilon Y^2(1 + \alpha)}; \quad Y = \frac{\rho_T\gamma}{1 + \gamma}.$$

We take the flux from the aggregate into the computational domain to be proportional to β . Specifically, we take $F(t) = F_0\beta(t)/\beta_{max}$ with $F_0 = 200$ molecules/ $(\mu\text{m s})$ and where we have normalized $\beta(t)$ by its maximum value β_{max} .

Dispersal in mutants

As mentioned in the main text, we have verified that aggregates of mutant cells lacking the quorum sensing proteins AprA, CF50, CfaD, and CtnA were still able to display dispersal. Specifically, we found that 33/43 aprA^- , 23/33 CF50^- , 22/62 cfaD^- , and 20/31 CtnA^- aggregates clearly displayed apparent outward cell motion for at least three oscillations. This data was taken from 3-7 different sets over multiple days. Examples of these dispersing aggregates are presented in Movie S8.

Acknowledgements

Chapter 1, in full, is a reprint of the material as it appears in the Proceedings of the National Academy of Sciences of the United States of America. 2021. Tyree, TJ*; Karmakar, R*, Gomer, RH, Rappel WJ., United States National Academy of Sciences, 2021. The dissertation author was the primary investigator and author of this paper.

Movie legends

- Movie S1: DIC movie (left) and corresponding optical flow (right) of a dispersing aggregate showing multiple dispersing events (scalebar: 100 μm).
- Movie S2: DIC movie of a dispersing aggregate, shown within the circle, that displays a limited number of dispersing events. After the dispersal, nearby cells are moving, on average, towards the aggregate again (scalebar: 100 μm).
- Movie S3: Example of an aggregate that disperses completely (scalebar: 100 μm).
- Movie S4: Movie of a dispersing aggregate, showing the DIC images (left) and the simultaneous Flamindo2 fluorescence intensity (right). Note that a decrease in Flamindo2 intensity corresponds to an increase in cytosolic cAMP (scalebar: 100 μm).
- Movie S5: Example of a 2D simulation showing dispersal. The particle positions are indicated by white disks and the cAMP using the displayed color scale ($L_{PDE} = 100 \mu\text{m}$ and $k_{PDE}=0.04/\text{s}$).
- Movie S6: Simulation showing the effect of adding a PDE inhibitor ($L_{PDE} = 100 \mu\text{m}$ and $k_{PDE}=0.04/\text{s}$).
- Movie S7: Simulation showing the effect of the global addition of PDE ($L_{PDE} = 100 \mu\text{m}$ and $k_{PDE}=0.04/\text{s}$).
- Movie S8: Movie of dispersing aggregates consisting of aprA^- , CF50^- , cfaD^- , and CtnA^- cells (scalebar: 100 μm).

Table 1.1. Parameters used in the simulation of radial cAMP profiles.

Parameter	Name	Value
r_0	aggregate radius	$50 \mu\text{m}$
r_{max}	domain size	1 mm
Δx	grid resolution	$2 \mu\text{m}$
Δt	time resolution	1 s
D_{cAMP}	diffusion coefficient of <i>cAMP</i>	$400 \mu\text{m}^2/\text{s}$
D_{PDE}	diffusion coefficient of <i>PDE</i>	$10 \mu\text{m}^2/\text{s}$
F_0	Amplitude of <i>cAMP</i> flux	$2 \times 10^2 \text{ molecules}/(\mu\text{m s})$
v_0	cell velocity	$5 \mu\text{m}/\text{min}$
δ^*	smallest sensible gradient	$6.67 \times 10^{-3} \text{ nM}/\mu\text{m}$

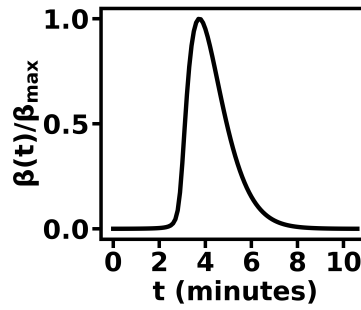


Figure 1.7. Shape of attractant pulse. Normalized intracellular cAMP concentration in the Martiel-Goldbeter model as a function of time.

Table 1.2. Parameters used in the simulation of cAMP biosynthesis. Parameters used in the calculation of cAMP flux generated by the aggregate as a function of time. For further details, see the original publication [131].

Parameter	Name	Value
k_t	cAMP secretion rate	0.9/min
k_e	extracellular cAMP degradation rate	5.4/min
k_i	intracellular cAMP degradation rate	1.7/min
k_1	basal CAR deactivation rate constant	0.036/min
k_2	CAR deactivation rate constant	0.666/min
σ	intracellular cAMP synthesis rate constant	0.6/min
q	adenylyl cyclase activity constant	4000
c	sensitivity constant of CAR to cAMP	10
L_1	relative basal CAR activation rate constant	10
L_2	relative CAR activation rate constant	0.005
λ	cAMP basal synthesis constant	0.01
θ	cAMP basal synthesis constant	0.01
ρ_V	ratio of intracellular to extracellular volumes	0.2
ε	sensitivity constant of cAMP synthesis to extracellular cAMP	1
α	intracellular ATP	3

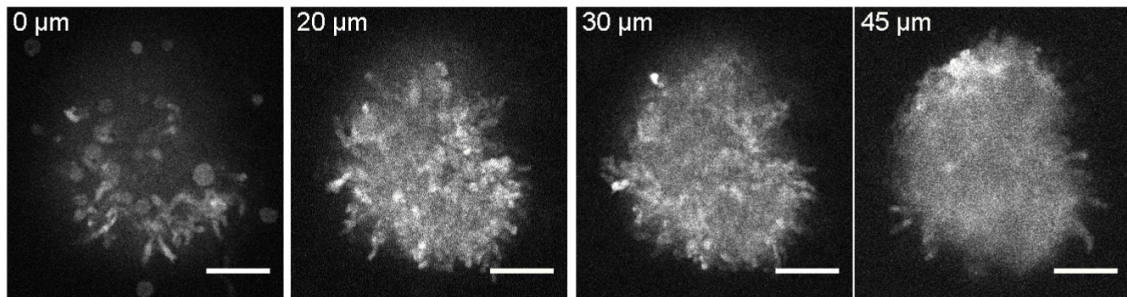


Figure 1.8. Dispersing cell aggregate. Confocal z-stacks of a dispersing aggregate, showing the extent of the aggregate using Flamindo2 fluorescent intensity (scale bar: 50 μm.)

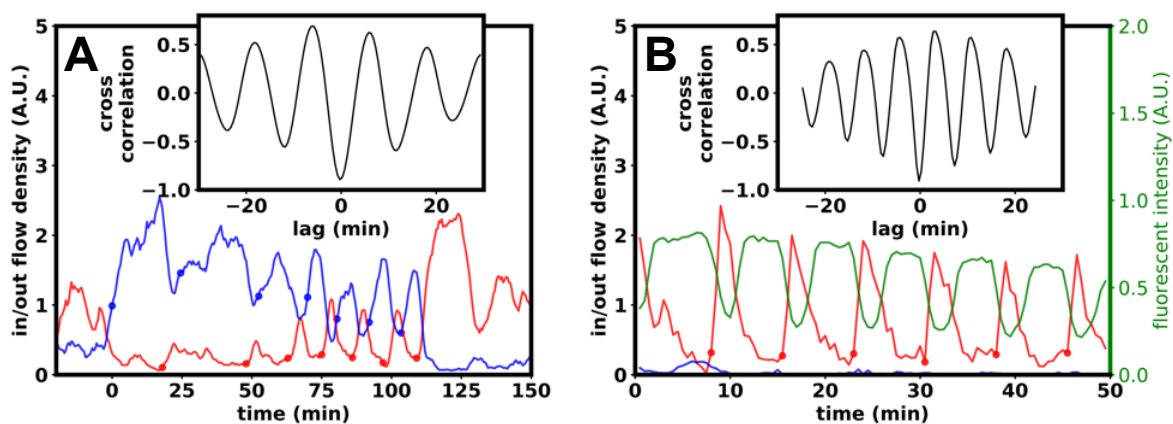


Figure 1.9. Correlation of collective cell motion and fluorescent intensity. [a] Time traces of and cross correlation function (inset) between inward (red) and outward (blue) cell motion (red) of the dispersing aggregate of Fig. 1. Inward cell motion was anti-correlated with outward cell motion near this dispersing aggregate oscillating at a period of $T = 12$ minutes and a phase shift of $(1.0 \pm 0.2)\pi$. Phase shift uncertainty was estimated from the full width half max of the relevant cross-correlation function. [b] Time traces and (inset) cross correlation function between inward cell motion (red) and Flamindo2 fluorescent intensity (green) near a non-dispersing aggregate. Fluorescence intensity was anti-correlated with inward cell motion with a period of $T = 7$ minutes and a phase shift of $(1.0 \pm 0.1)\pi$.

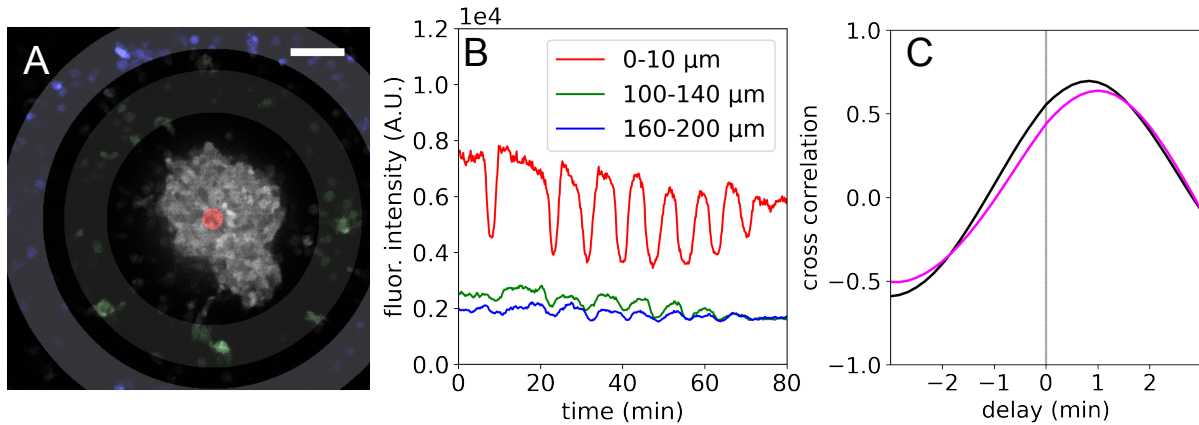


Figure 1.10. Dispersing cell aggregate is source of correlation. [a] Regions in which the Flamindo2 fluorescent intensity was recorded: within 0-10 μm from the dispersing aggregate center (indicated in red), only in neighboring cells located 100-140 μm from the center (marked as green cells), and only in the neighboring cells located 160-200 μm from the center (marked as blue cells) (Scale bar: 50 μm). [b] Raw fluorescent intensity as a function of time for the three regions indicated in panel A (time resolution: 10 s). [c] The cross correlation of the fluorescent intensity from the center of the aggregate to the nearby neighboring cells (black) and from the center of the aggregate to the more distant neighboring cells (cyan). The cross-correlation reaches a maximum for the black curve at $t \sim 50$ s and at $t \sim 70$ s for the cyan curve, supporting the idea that the diffusive signal from the aggregate is driving the cAMP signaling in neighboring cells.

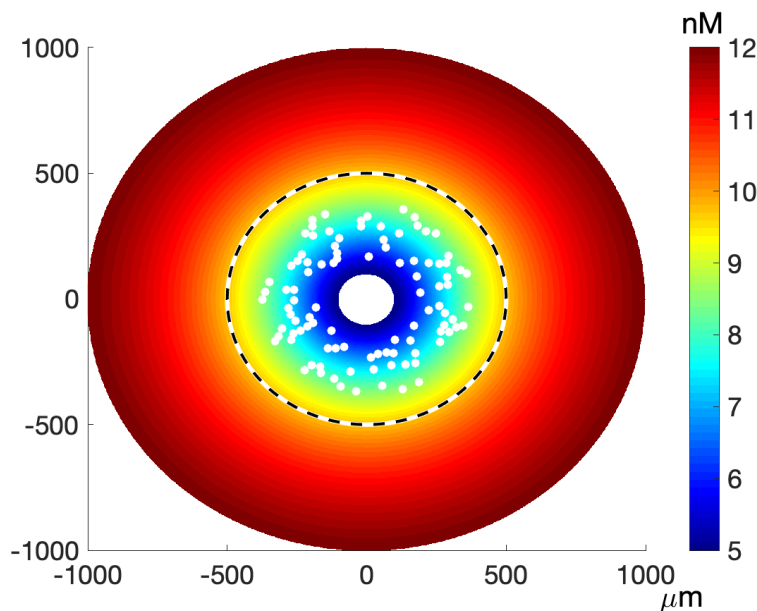


Figure 1.11. Snapshot of model simulation. Snapshot of a simulation, showing the cAMP using a colorscale. Individual cells are represented as white disks. The sub-domain with radius of 500 μm , used in the computational movies (Movie S5-7), is indicated by the dashed circle.

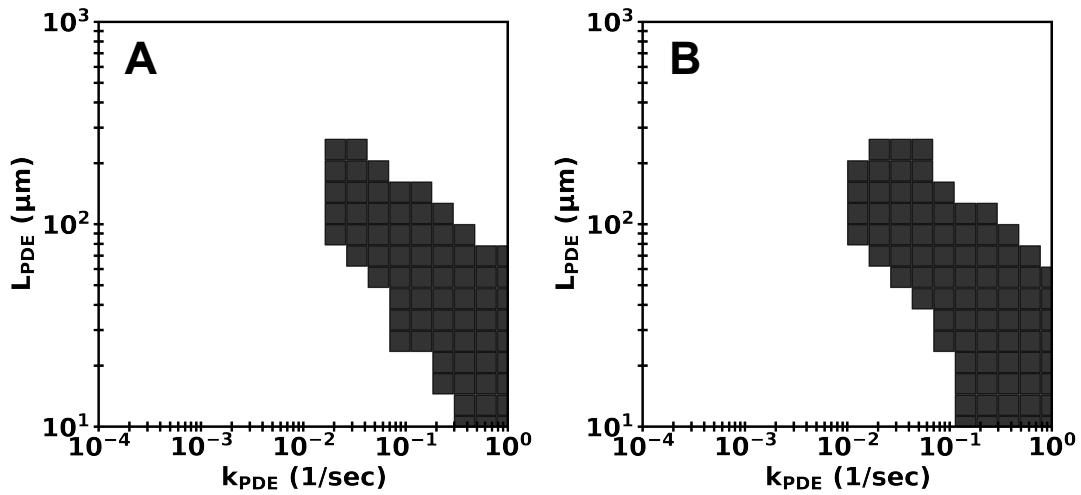


Figure 1.12. Dispersal phase diagrams. [a] Phase diagram obtained using the simplified 1D model, which ignores contributions from single cells, using the parameters corresponding to Fig. 3B. [b] Phase diagram obtained using the 1D model with $cAMP_{back}=6\text{nM}$ and $r_{max}=500\ \mu\text{m}$.

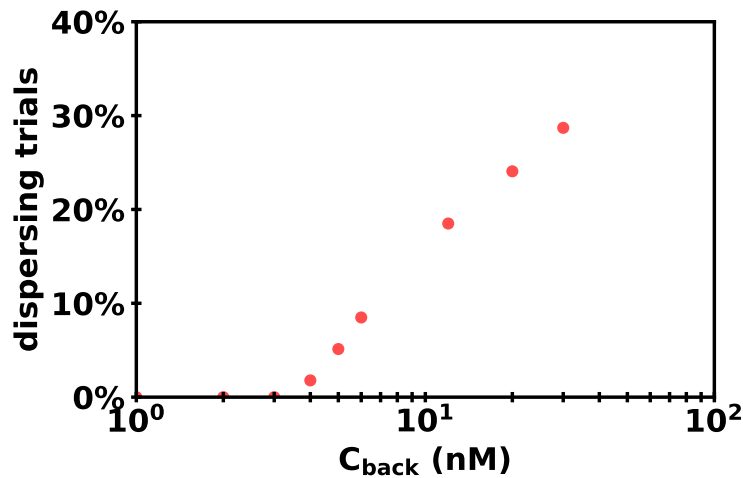


Figure 1.13. Minimum background attractant. Percentage of trials that supported dispersal as a function of C_{back} . This percentage was computed by discretizing the phase diagram in terms of L_{PDE} , k_{PDE} in the range $10\ \mu\text{m} < L_{PDE} < 200\ \mu\text{m}$ and $10^{-3}\text{s}^{-1} < k_{PDE} < 1\text{s}^{-1}$ into 400 logarithmically spaced sample points and by then numerically determining whether dispersal was present for each point. Dispersal was only present for $C_{back} \geq 5\ \text{nM}$.

Chapter 2

Annihilation dynamics during spiral defect chaos revealed by particle models

Many physical systems exhibit annihilation events during which pairs of objects collide and are removed from the system. These events occur in a number of soft-matter and active-matter systems that exhibit spatiotemporal patterning. For example, topological defects in nematic liquid crystals can develop motile topological defects that annihilate when they meet [53, 123]. Pair-wise annihilation of defects or singularities also plays a role in a number of biological systems. In bacterial biofilms, for instance, imperfect cell alignment results in point-like defects that carry half-integer topological charge and can annihilate in pairs. These topological defects explain the formation of layers and have been proposed as a model for the buckling of biofilms in colonies of nematically ordered cells [20, 43].

In this study, we focus on the pair-wise annihilation that occurs during spiral defect chaos in excitable systems. In this state, spiral waves continuously break down to form new ones and are removed through collisions with other spiral waves. While spiral defect chaos is present in a variety of chemical and biological pattern-forming systems [44, 177, 57, 88, 152, 59, 49, 209, 18, 164, 90, 60], perhaps its most studied example can be found in models of cardiac tissue [99, 202, 41, 174]. These models naturally exhibit spiral waves and the tips of these spiral waves undergo stochastic annihilation events [119, 212, 120]. Importantly, these annihilations underlie cardiac fibrillation, characterized by unorganized electrical wave propagation in the heart [174].

Fibrillation in the ventricles is lethal [93] while atrial fibrillation—the most common cardiac arrhythmia in the world with approximately 30 million patients in 2010—is associated with increased morbidity and mortality [144, 140, 39, 116].

The extinction dynamics of spiral tips in spatially extended cardiac models have been studied recently, revealing that it can be described by a stochastic birth-death process [212, 175]. By simulating cardiac models on various domain sizes, the creation and annihilation rates of spiral tips were determined. Using these rates, the mean termination time, τ , was computed and was shown to be exponentially distributed, consistent with experiments and clinical data [50, 212, 175]. This termination time is a quantity of interest in the context of cardiac dynamics as termination indicates the heart has transitioned into normal sinus rhythm. Thus, minimizing τ is of critical importance for managing cardiac fibrillation. Previous work has shown τ depends on the tissue size, A , and reducing τ can be achieved by reducing A [164, 212]. Unfortunately, decreasing the size of cardiac tissue is not practical without invasive surgery. Therefore, determining the dependence of τ on other physiological properties is desirable, especially if these properties can be drug-targeted.

In this study, we propose targeting the attraction coefficient, a , which controls the strength of attraction between spiral wave tips. We first simulate two spatially extended cardiac models and show that the spiral tip dynamics in these models is described by an attractive interaction at short distances and diffusive Brownian behavior at large distances. We then formulate a stochastic model in which tips are represented as particles and show that it can capture the attractive and diffusive properties of the tips in the cardiac models. Furthermore, we show that this particle model generates tip dynamics that reproduce both the annihilation rates as a function of the density of tips and the distribution of termination times for the two cardiac models. Finally, we show that increasing the attraction coefficient significantly decreases the mean termination time of spiral defect chaos.

To determine the dynamics of spiral wave tips in the cardiac models, we integrated the

mono-domain equations, which describe the time evolution of the membrane potential, u , by

$$\partial_t u = D_u \nabla^2 u - f(\mathbf{y}). \quad (2.1)$$

Here, the diffusion coefficient, D_u , is a constant scalar parameter, while the auxiliary variables, \mathbf{y} , encode electrophysiological trans-membrane currents according to

$$\partial_t \mathbf{y} = \mathbf{g}(u, \mathbf{y}). \quad (2.2)$$

The precise formulation of f and \mathbf{g} is provided in the Supplementary Information along with the model parameters. To stress the generality of our approach, we used two commonly-employed models for cardiac tissue: the Fenton-Karma (FK) model [63] and the Luo-Rudy (LR) model [127]. We integrated Eqns 2.1-2.2 explicitly on a square computational domain of size A and enforced periodic boundary conditions, which results only in the pair-creation and pair-annihilation of spiral tips due to global conservation of vorticity in u . We used a spatial discretization of $\Delta x = 0.025$ cm and a temporal discretization of $\Delta t = 0.025$ ms and computed spiral tip locations via the intersecting level-set method [63].

Simulations of the cardiac models started with random initial conditions that contained multiple spiral tips and continued until all spiral wave tips were annihilated. A snapshot of a simulation is shown in Fig. 2.1A for the LR model, with u visualized using a gray scale and clockwise and counterclockwise spiral wave tips are indicated by black and yellow symbols, respectively. Additional snapshots, including ones for the FK model, are shown in Fig. 2.5 of Supplementary Information. In these simulations, only pairs of counter-rotating tips that are connected by an activation front can annihilate (Fig. 2.1A). For a movie that demonstrates how spiral tips create and annihilate in pairs we refer to Movie S9.

To quantify the dynamics of the spiral wave tips, we first computed the lifetime of annihilating pairs, Γ . The distribution of these lifetimes was approximately exponential (Fig. 2.6A

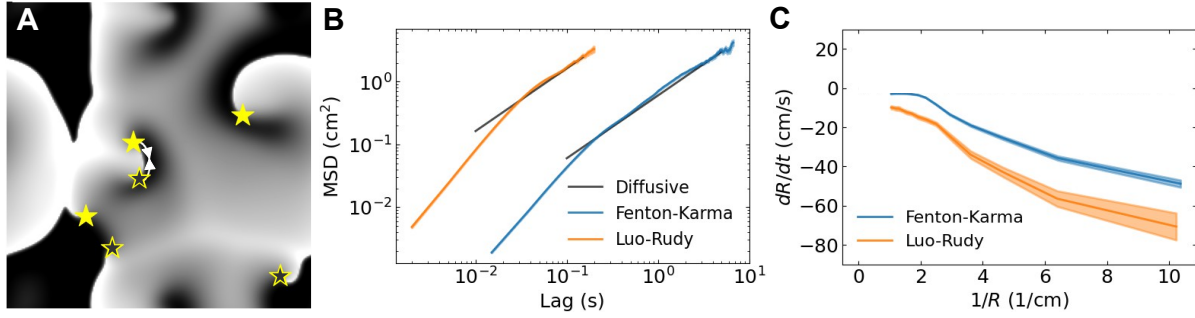


Figure 2.1. Spiral tip properties. **A** Grayscale snapshot of the membrane potential u showing spiral defect chaos in the LR model with $A = 25 \text{ cm}^2$. Indicated are the tips of clockwise (black stars) and counterclockwise (yellow stars) rotating spiral waves. Spiral tips attract and annihilate in pairs as indicated by the white arrows. **B** MSD of spiral tips versus temporal lag. Black lines indicate Brownian motion. **C** Mean radial velocity versus inverse distance between annihilating tips. Shaded bands represent 95% confidence intervals.

of Supplementary Information) with the FK model producing significantly longer-lived pairs on average (Table 2.1). By averaging over an ensemble of tip trajectories, we next computed the mean squared displacement (MSD) of the spiral wave tips as a function of time lag [163], shown in Fig. 2.1B. For a domain size of $A = 25 \text{ cm}^2$, results from both cardiac models show that the MSD is not significantly different from linear for long timescales with exponent values of 1.002 ± 0.015 (FK model for time lags $> 100 \text{ ms}$) and 0.98 ± 0.04 (LR model for time lags $> 60 \text{ ms}$). Thus, in both cardiac models, the spiral wave tips effectively undergo Brownian motion for long timescales. At short timescales, however, the tips did not exhibit diffusive behavior.

To determine the behavior of the tips at short timescales, we further analyzed the movement of spiral waves in the simulations. This analysis revealed that annihilation occurs when the activation front connecting the tip pair is blocked by a nearby polarized region. The block results in a rapid shrinking of the activation front and the removal of the pair (see also Movie S9). Thus, at short timescales, the annihilating pair of tips appear to attract, which becomes apparent from Fig. 2.1C where we plot the ensemble-averaged radial velocity dR/dt as a function of the distance between the tips, R . This velocity is not constant, but instead, becomes more negative when $1/R$ increases (and R decreases). In other words, an apparent attractive force induced the annihilation of counter-rotating pairs of spiral waves.

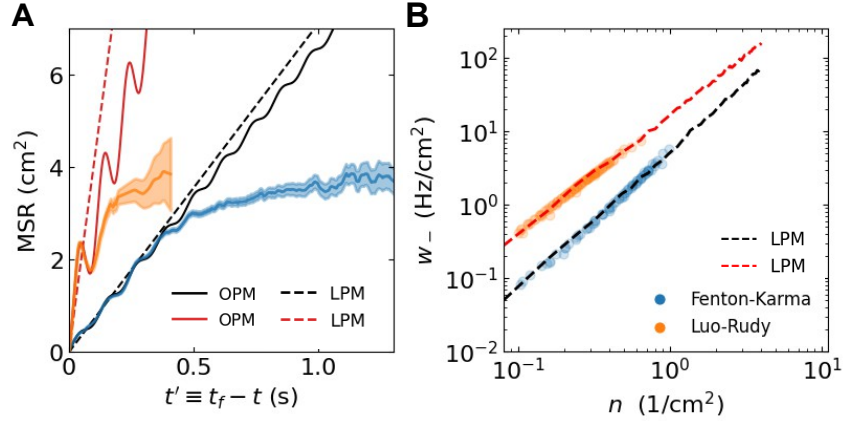


Figure 2.2. Pair-annihilation dynamics. **A** MSR between annihilating tips versus time until annihilation from simulations of the FK and LR models with shaded regions corresponding to 95% confidence intervals. Also shown are the fits of the MSR from the OPM (solid lines) and the LPM (dashed lines). **B** Mean annihilation rate versus number density for spiral tips from the cardiac models (symbols) and their linear particle model fits (dashed lines).

To quantify this attractive force, we identified more than 1.5×10^3 annihilating pairs for each cardiac model. For a given pair annihilating at time t_f , we determined R versus time until annihilation, $t' \equiv t_f - t \geq 0$. From this, we computed the mean squared range (MSR) by ensemble-averaging R^2 conditioned on a given t' . The results are shown in Fig. 2.2A as solid lines, together with the 95% confidence intervals as shaded areas. On short timescales, the MSR demonstrates oscillations, illustrating that the apparent attractive force has an oscillatory component.

To gain further insight into the annihilation dynamics of the tips using the spatially extended cardiac models is computationally expensive, especially for large domain sizes. Therefore, we developed a computationally efficient model in which the spiral wave tips are represented by moving particles subject to an oscillatory short-range attractive force and Brownian motion with diffusion coefficient, D . Such a significant simplification of a cardiac model was earlier used to describe the chaotic tip trajectories of a single spiral wave in the presence of heterogeneities [125]. Here we formulated an oscillatory particle model (OPM) in which we modeled the strength of attraction between two annihilating tips as inversely proportional to the distance between them and in which the radial component of this force was taken to be the sum of a

constant term, a_0 , and a locally precessing term with period, $T_{OPM} = 2\pi/\omega$, and amplitude, a_1 . Thus, the distance between annihilating tips can be modeled by the following Langevin equation:

$$dR_i(t') = -\frac{2}{R_i(t')} \left(a_0 + a_1 \cos(\omega t' + \phi_f) \right) dt' + \sqrt{8D} dW_{t'}, \quad (2.3)$$

where $W_{t'}$ is a Wiener process at time t' , D is estimated from the least-square slope of MSR at large ranges ($MSR > 3 \text{ cm}^2$), and ϕ_f is a final phase difference. Note that the factor of two arises from the pair-wise interaction while the factor of 8 arises from the additivity of variance.

Integrating $\mathbb{E}[d(R_i^2(t'))]$ according to the Stratonovich formulation of stochastic calculus results in

$$MSR_{OPM}(t') = 4 \left(2Dt' + a_0 t' + \frac{a_1}{\omega} (\sin(\omega t' + \phi_f) - \sin(\phi_f)) \right). \quad (2.4)$$

This result was verified by comparing this expression to the average MSR of many statistically independent simulations of Eqn. 2.3. The next step was to fit Eq. 2.4 to the MSR curves obtained from the cardiac models using simulated annealing on the last 300 ms (FK) and 100 ms (LR) before annihilation. The fits to both cardiac models for these time intervals are excellent (mean percent error (MPE) $< 4\%$), as can be seen Fig. 2.2A. The fitted parameters, a_0 , a_1 , ϕ_f , and T_{OPM} are reported in Table 2.1, together with the aforementioned estimates for D . As expected, the fitted period of the OPM matches the period of the spiral waves in the cardiac models. In Table 2.1 we also report the period of the spiral waves in the cardiac models, T , determined by computing the mean number of rotations per lifetime. A comparison between T_{OPM} and T reveals that these periods match perfectly, indicating that the oscillatory component in the MSR is due to the rotational nature of the spiral wave.

The OPM can, in principle, be used to compute annihilation rates, which can then be compared to results from the cardiac models. However, computing these rates with the OPM is challenging because annihilation only occurs when the final phase difference between the two particles takes a specific value. Thus, it requires the tedious task of keeping track of the phase

for each particle and implicitly enforcing the condition $\phi(t_f) = \phi_f$ at the time of annihilation. To circumvent this problem, we simplified the OPM to a linear particle model (LPM) by taking the attractive force between particles as linear in $1/R$. Modeling the diffusive behavior of spiral tips as before, the LPM reads

$$dR_i(t') = -\frac{2a}{R_i}dt' + \sqrt{8D}dW_{t'}, \quad (2.5)$$

which similarly results in a MSR given by

$$\text{MSR}_{\text{LPM}}(t') = 4(a + 2D)t'. \quad (2.6)$$

To relate a to the parameters of the OPM, we demanded that the MSR averaged over the exponentially distributed lifetimes of the cardiac models, $\langle \text{MSR} \rangle$, be equal for both particle models. For the LPM, we can derive

$$\langle \text{MSR}_{\text{LPM}} \rangle = \int_0^\infty \left(\frac{dt'}{\Gamma} e^{-t'/\Gamma} \right) 4(a + 2D)t' = 4(a + 2D)\Gamma. \quad (2.7)$$

while a similar calculation for the oscillatory particle model gives

$$\langle \text{MSR}_{\text{OPM}} \rangle = 4 \left(a_0 + a_1 \frac{\cos(\phi_f) - \omega\Gamma \sin(\phi_f)}{1 + (\omega\Gamma)^2} + 2D \right) \Gamma. \quad (2.8)$$

Setting $\langle \text{MSR}_{\text{LPM}} \rangle = \langle \text{MSR}_{\text{OPM}} \rangle$ results in an analytical expression for a in terms of the OPM parameters that is independent of D :

$$a = a_0 + a_1 \frac{\cos(\phi_f) - \omega\Gamma \sin(\phi_f)}{1 + (\omega\Gamma)^2}. \quad (2.9)$$

The estimates of a evaluated from Eq. 2.9 are listed in Table 2.1, and corresponding MSR_{LPM} plots are shown as dashed lines in Fig. 2.2A. Repeating the analysis for different domain sizes, A , revealed that the estimate of a was largely independent of A for both of the cardiac models

(Fig. 2.7 of Supplementary Information). Thus, the LPM can be used to simulate spiral tip annihilation in different domain sizes using a fixed set of model parameters, determined for a single value of A .

We implemented the LPM, using the obtained values of a and D , by numerically integrating Eq. 2.5 on a spatially-extended square computational domain with periodic boundary conditions. For initial conditions, we considered N uniformly distributed particles at two domain sizes ($A = 25 \text{ cm}^2$ and $A = 100 \text{ cm}^2$), and updated the particle positions every $\Delta t = 0.01 \text{ ms}$ (see also Supplementary Information). Pairs of particles were removed from the simulations, and thus annihilated, at rate κ whenever they were closer than a reaction range, r . As an estimate for this range we chose the 25th percentile of the distribution of distances between non-annihilating tips. We have verified, however, that other choices of r give similar qualitative results.

We then used the LPM to compute annihilation rates and adjusted the only free parameter (κ) to match the annihilation rates found in the cardiac models. This is facilitated by the fact that in our previous work we showed that the latter, computed for different domain sizes A , collapse onto a single curve when rescaled by A [212]. Furthermore, in this study, we report that the annihilation rate can be approximated by a power law, $w_- = M_- n^{v_-}$, where $w_- \equiv W_-(N)/A$ is the rescaled annihilation rate and $n = N/A$ is the tip density (Fig. 2B). The fitted LPM annihilation rates are shown as lines in Fig. 2.2B and the resulting LPM parameters are listed in Table 2.2. These fits demonstrate that the LPM can accurately replicate the annihilation rates of the cardiac models (MPE <4%). Importantly, as was the case for a , these fits use the same parameter values for both system sizes, and modifying the parameter κ based on domain size allows for good fits at both domain sizes. Note that simulations of the particle model are much more efficient than the cardiac models, especially for large domain sizes, as they use $\mathcal{O}((L/\Delta x)^2) \sim 10^3$ fewer degrees of freedom. For example, for $A = 100 \text{ cm}^2$, the speed-up exceeded 10^4 -fold.

By carrying out additional simulations of the LPM, we determined how the annihilation rate depends on the attraction coefficient, a , while holding the remaining parameters D , r , and κ

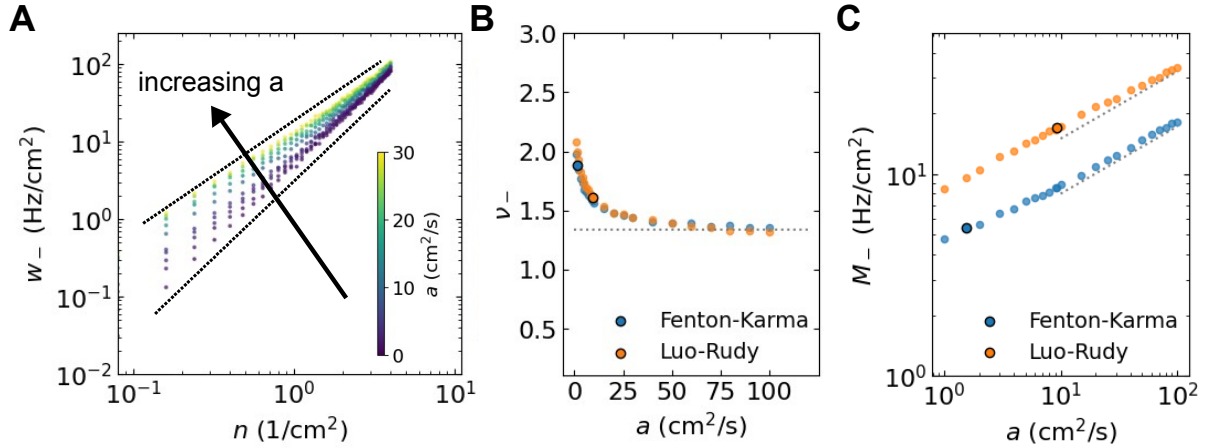


Figure 2.3. Pair-annihilation power laws. **A** Mean annihilation rate versus number density obtained from power law fits of the LPM using parameters corresponding to the FK model for different values of a (indicated by the color bar). Dotted lines correspond to power laws. **B** Power law exponent as a function of a computed using the LPM with parameters corresponding to both the FK and LR model (dotted line: $\nu_- = 4/3$). **C** Corresponding power law magnitude versus a . Black circles in B&C represent values of a corresponding to the cardiac models. Dotted line has exponent $1/3$.

fixed. Perhaps not surprisingly, since larger attractive forces result in distant particles coming together faster, this rate was found to increase with increasing values of a . Importantly, however, we found that the rate was again always fitted well by the power law $w_- = M_- n^{\nu_-}$ (Fig. 2.3A). For both models, we found that for increasing values of a the exponent ν_- became smaller (Fig. 2.3B) while M_- increased (Fig. 2.3C).

Using the fact that the annihilation rate can be fitted by a power law in the LPM, we were able to compute statistical properties of spiral defect chaos in the spatially extended cardiac models. For this, we used the creation rate in the cardiac models, which we found to be captured by a power law fit as well: $w_+ = M_+ n^{\nu_+}$ (Fig. 2.4A). In the remainder, we will keep this creation rate fixed while varying a , and thus the annihilation rate, according to Figs. 2.3B&C. Using the power laws for creation and annihilation rates, we constructed a transition matrix from which we computed the distributions of termination times [146, 212]. These distributions were found to be exponentially distributed for all values of a (Fig. 2.4B, see also Fig. 2.6B of Supplementary Information), consistent with experimental data [50]. Furthermore, the distribution tends to

smaller termination time values for increasing a .

Using these power laws, it is now straightforward to determine the mean particle number, N_{avg} , which can be estimated by solving $w_+(n) = w_-(n)$. This results in a closed expression for N_{avg} :

$$N_{\text{avg}} = An_{\text{avg}} = A \left(\frac{M_+}{M_-} \right)^{\frac{1}{v_- - v_+}}, \quad (2.10)$$

which shows that the mean particle number increases linearly with the domain size. Fig. 2.4C shows the results from this expression, using parameters corresponding to $A = 25\text{cm}^2$ for all domain sizes, which is possible since a is insensitive to A (Fig. 2.7 of Supplementary Information). The estimated value using Eq. 2.10 agrees well with the average number of tips from the cardiac models (symbols). Finally, the average number of tips computed using Eq. 2.10 decreases as a function of a (Fig. 2.4D), which can be explained by the fact that v_- decreases for increasing values of a (Fig. 2.3C).

It is now also possible to obtain an approximate expression for the mean termination time of spiral defect chaos, a property especially relevant to cardiac models and fibrillation in clinical settings. For paired birth-death processes, it can be computed using an analytic solution [73] and is a function of the initial (even) number of spiral tips, N_0 , [73]:

$$\tau(N_0) = \sum_{k=1}^{N_0/2} \varphi(2k-2) \sum_{j=k}^{\infty} \frac{1}{\varphi(2j)w_+(2j/A)A} \quad (2.11)$$

where $\varphi(2k) = \prod_{i=1}^k w_-(2i/A)/w_+(2i/A)$ and $\varphi(0) \equiv 1$. Since the termination time is dominated by $\tau(2)$, we can use the obtained power laws to derive an approximate closed expression. For large values of A , the termination time can be shown to be proportional to [212]

$$\tau \sim \exp \left[\frac{A}{2} \int_{2/A}^{n_{\text{avg}}} \ln \frac{w_{+2}(s)}{w_{-2}(s)} ds \right] \quad (2.12)$$

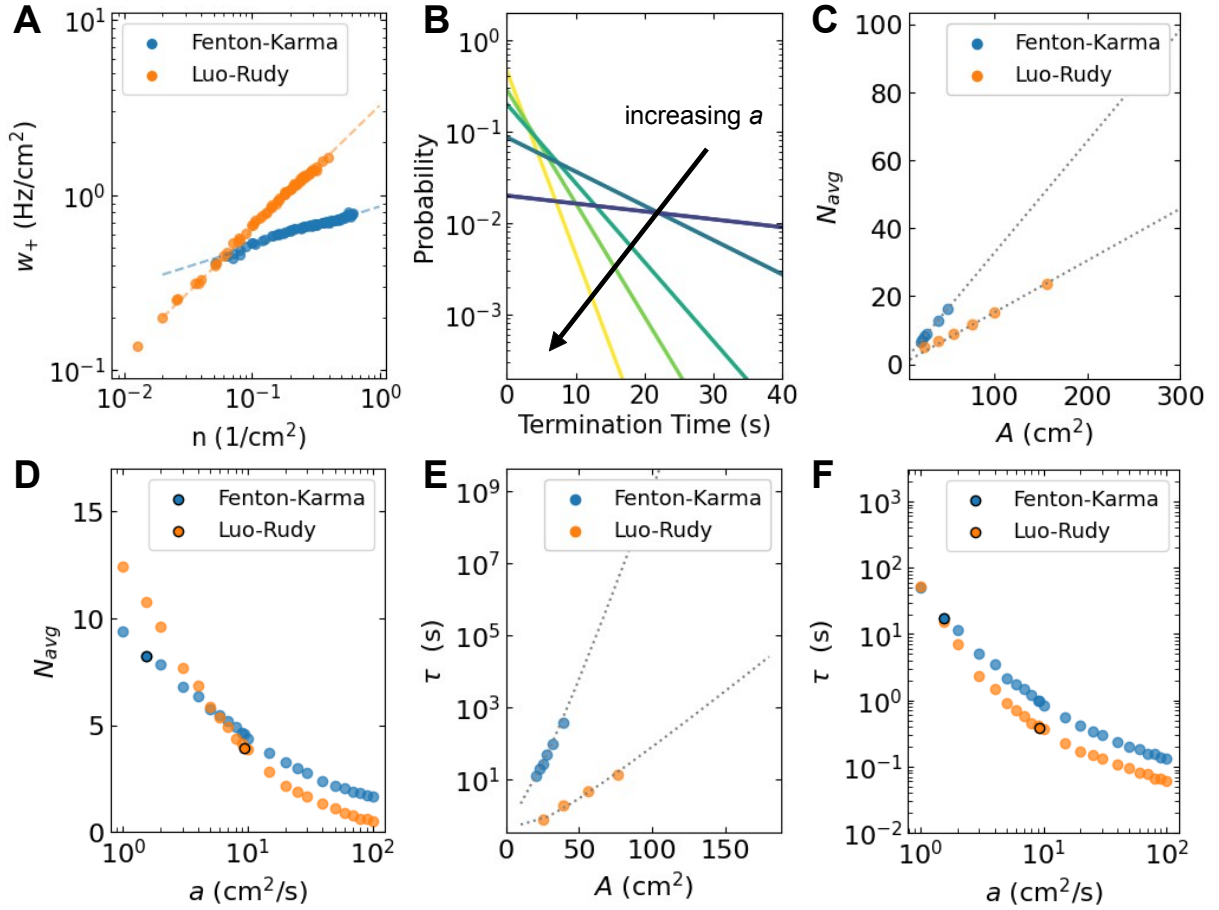


Figure 2.4. Termination statistics. **A** Mean creation rate versus number density for spiral tips from the cardiac models using different domain sizes. Dashed lines correspond to power law fits, resulting in $M_+ = 0.864 \pm 0.002$ Hz/cm² and $v_+ = 0.23 \pm 0.010$ (FK model) and $M_+ = 3.28 \pm 0.10$ Hz/cm² and $v_+ = 0.715 \pm 0.010$ (LR model). **B** Probability density of termination times of the LPM for increasing values of a equally spaced from $a = 1$ cm²/s to $a = 5$ cm²/s. Parameter values correspond to the FK model and $A = 25$ cm². **C** Average tip number as a function of A computed using the cardiac models (symbols), along with the linear prediction of Eq. 2.10. **D** Average tip number as a function of a computed using the LPM with parameter values corresponding to $A = 25$ cm². The darkened symbols correspond to the value of a representing the cardiac models. **E** Mean termination time versus A computed using Eq. 2.13 (dashed lines) and separately obtained from the cardiac models (symbols). **F** Mean termination time as a function of a (using parameter values for $A = 25$ cm²). Black circles correspond to cardiac models.

which becomes, after substituting the expressions for w_{\pm} :

$$\tau \sim \left(\frac{2}{A}\right)^{v_- - v_+} e^{An_{avg}(v_- - v_+)/2} \quad (2.13)$$

Thus, consistent with earlier work using the cardiac models [164, 212], the termination time increases exponentially with A . Furthermore, aside from a prefactor that is independent of A , this expression provides an explicit estimate for τ for any domain size, including ones that would be prohibitively expensive to simulate directly. This is shown in Fig. 2.4E, where we plot the values for τ obtained from the cardiac models as symbols together with a fit using Eq. 2.13. The former ones were, of course, only obtainable for small domain sizes while the fit can be extended to arbitrary large sizes.

We also computed τ , as given by Eq. 2.11, as a function of a with the other parameters fixed to those corresponding to the cardiac models. We found that τ decreased by a factor of $\sim 10^2$ in response to a increasing by a mere factor of 10, as shown in Fig. 2.4F. This great sensitivity of τ to a , considered together with the relative insensitivity of a to A , suggests that changing a is a potential mechanism for controlling the mean termination time for fixed domain sizes. Specifically, if modifying the electrophysiological parameters of the cardiac models increases attraction only, then τ decreases, resulting in shorter termination times. Therefore, it would be interesting to determine whether this control is achievable by altering tissue dynamics using pharmaceutical intervention.

In summary, this study reveals that the annihilation dynamics of spiral waves in spatially extended cardiac models can be captured by a computationally efficient particle model. In this model, the spiral wave tips are represented by diffusing particles, with a diffusion coefficient determined from spiral tip motion, and a local attractive force. We showed that the particle model accurately reproduced the annihilation rates of spiral tips in the cardiac models and that it can be used to efficiently model their tip dynamics. Our study shows that the parameters of the particle model were largely insensitive to domain size, suggesting they can be obtained from tip

Table 2.1. Particle properties of spiral tips from the cardiac models including parameter values corresponding to OPM and LPM.

Symbol	Fenton-Karma	Luo-Rudy
Γ (ms)	105.3 ± 1.7	33.4 ± 0.7
D (cm ² /s)	0.115 ± 0.008	0.42 ± 0.14
a_0 (cm ² /s)	1.407 ± 0.016	4.2 ± 0.3
a_1 (cm ² /s)	1.2822 ± 0.0005	12.180 ± 0.012
ϕ_f (radians)	-0.541 ± 0.004	-1.165 ± 0.003
T_{OPM} (ms)	115.94 ± 0.03	97.36 ± 0.12
T (ms)	115.9 ± 1.9	97.4 ± 0.8
a (cm ² /s)	1.552 ± 0.017	9.3 ± 0.3
r (cm)	0.457 ± 0.009	0.314 ± 0.003
κ (Hz)	15	75

motion at a single domain size. This enabled us to compute a variety of statistical properties for arbitrary domain sizes, including the mean termination time, with minimal computational effort. We also used the particle model to show increasing the strength of the apparent attraction force accelerates annihilation, thus decreasing the mean termination time. In future work, we plan to extend our study by including non-conducting boundaries and an explicit formulation of creation events. Furthermore, future work involving cardiac models can investigate the dependence of the attraction coefficient between spiral tips on trans-membrane currents. Reproducing desirable effects on these currents can then be the target of drug discovery, potentially opening a new door to noninvasive therapies for clinically significant symptoms of cardiac fibrillation.

This work was supported by the National Institute of Health (NIH) through award HL083359, HL122384, and HL149134. T.T. acknowledges the support of the NIH through the Quantitative Integrative Biology Training Grant (T32GM127235) in addition to the Open Science Grid [158, 191] for allocation of computational resources. P.M acknowledges the support of the Research Training in Mathematical and Computational Biology Grant (1148230) and the NSF Division of Mathematical Sciences award 1903275.

Table 2.2. Power law fits for the annihilation rates.

Model		A (cm ²)	v_-	M_- (Hz/cm ²)
Fenton-Karma	Cardiac	25	1.88 ± 0.03	5.6 ± 0.3
	LPM	25	1.871 ± 0.012	5.53 ± 0.16
	LPM	100	1.835 ± 0.015	4.75 ± 0.17
Luo-Rudy	Cardiac	25	1.638 ± 0.017	16.7 ± 0.8
	LPM	25	1.614 ± 0.012	16.9 ± 0.7
	LPM	100	1.611 ± 0.017	12.6 ± 0.6

2.1 Supplementary Information

Detailed Equations and Parameters of Full Cardiac Models

The time evolution of the scalar field modeling trans-membrane voltage, V_m , is described by the excitable reaction-diffusion equation,

$$\partial_t u = D_u \nabla^2 u - I_{\text{ion}}/C_m \quad (2.14)$$

where $f = I_{\text{ion}}/C_m$ is the ratio of the electric charge current density, I_{ion} , to the trans-membrane capacitance per unit area, $C_m = 1 \mu\text{F}/\text{cm}^2$. The vector field of auxiliary dynamical variables, \mathbf{y} , take values locally everywhere on the computational domain. The scalar field, I_{ion} , is locally determined by \mathbf{y} together with V_m . While increasingly detailed models exist for the term $f = I_{\text{ion}}/C_m$, the main text considers the following two relatively simple cardiac models known to exhibit spiral defect chaos.

Fenton-Karma Model

Equations for the Fenton-Karma model used in this study are Eqn. 2.14 together with

$$I_{\text{ion}} = I_{\text{fi}} + I_{\text{so}} + I_{\text{si}},$$

where the fast inward current density is

$$I_{\text{fi}}(u, v) = -\frac{v}{\tau_d}(1-u)(u-u_c)\Theta(u-u_c),$$

the slow outward current density is

$$I_{\text{so}}(u) = u\frac{\Theta(u_c-u)}{\tau_0} + \frac{\Theta(u-u_c)}{\tau_r},$$

and the slow inward current density is

$$I_{\text{si}}(u, w) = \frac{w}{2\tau_{\text{si}}}\left(1 + \tanh(k(u-u_c^{\text{si}}))\right),$$

with parameter values $\tau_d = 0.45\text{ms}$, $\tau_0 = 12.5\text{ms}$, $\tau_r = 33.25\text{ms}$, $\tau_{\text{si}} = 29\text{ms}$, $k = 10$, and $u_c^{\text{si}} = 0.85$. We used $V' = 90\text{mV}$ and $V'' = 150\text{mV}$ to define the dimensionless trans-membrane voltage field $u = (V_m + V')/V''$.

The trans-membrane electric diffusion coefficient for the Fenton-Karma model was $D_m = 0.0005\text{cm}^2/\text{ms}$, and the time evolution of the auxiliary vector field, $\mathbf{y}(t) = (v(t), w(t))$, was locally described for the fast variable,

$$\frac{dv}{dt} = (1-v)\Theta(u_c-u)\left(\frac{\Theta(u-u_v)}{\tau_{v1}^-} + \frac{\Theta(u_v-u)}{\tau_{v2}^-}\right) - v\frac{\Theta(u-u_c)}{\tau_v^+} \quad (2.15)$$

and for the slow variable,

$$\frac{dw}{dt} = (1-w)\frac{\Theta(u_c-u)}{\tau_w^-} - w\frac{\Theta(u-u_c)}{\tau_w^+}, \quad (2.16)$$

where the parameters were taken to be $u_c = 0.13$, $u_v = 0.04$, $\tau_{v1}^- = 1250\text{ms}$, $\tau_{v2}^- = 19.6\text{ms}$, $\tau_v^+ = 13.03\text{ms}$, $\tau_w^- = 40\text{ms}$, and $\tau_w^+ = 800\text{ms}$.

The parameter set we used was taken from parameter set 8 of Ref. [56]. The conduction

velocity was $c_v = 51\text{cm/s}$, which is within the electrophysiological range.

Luo-Rudy Model

Equations for the Luo-Rudy model used in this study are Eqn. 2.14 together with

$$I_{\text{ion}} = I_{\text{Na}} + I_{\text{si}} + I_{\text{K1T}} + I_{\text{K}},$$

where the current density from sodium is

$$I_{\text{Na}} = (V_m - E_{\text{Na}})G_{\text{Na}}jhm^3.$$

with parameter values $G_{\text{Na}} = 16\text{mS/cm}^2$ and $E_{\text{Na}} = 54.4\text{mV}$. The slow inward current density is

$$I_{\text{si}} = G_{\text{si}}(V_m - E_{\text{si}})fd,$$

where $G_{\text{si}} = 0.052\text{mS/cm}^2$ and $E_{\text{si}} = -82.3\text{mV} - 13.0287 \log([Ca^{+2}]_i/(1\text{mM}))$.

The current density attributed to potassium is $I_{\text{K1T}} + I_{\text{K}}$, computed using the equations and parameters of Ref. [166, 165]. We have used $[K^+]_o = 5.4\text{mM}$. $G_{\text{K}} = 0.423\text{mS/cm}^2$ and $[K^+]_i = 145\text{mM}$, $[Na^+]_i = 18\text{mM}$, and $[Na^+]_o = 145\text{mM}$. We supposed a fixed homeostatic body temperature of $T = 37^\circ\text{C}$. The trans-membrane diffusion coefficient for the Luo-Rudy model was $D_m = 0.001\text{cm}^2/\text{ms}$, and the time evolution of the auxiliary vector field, $\mathbf{y}(t) = ([Ca^{+2}]_i(t), m(t), h(t), j(t), d(t), f(t), x(t))$, was locally described by

$$d[Ca^{+2}]_i/dt = -\left(10^{-7} \frac{\text{mM}}{\mu\text{A}}\right)I_{\text{si}} + (0.07\text{ms}^{-1})(10^{-7}\text{mM} - [Ca^{+2}]_i)$$

for intracellular calcium and for the dimensionless gating variables, $y = m, h, j, d, f, x$, by

$$dy/dt = (y_\infty - y)/\tau_y. \quad (2.17)$$

Furthermore, we used

$$y_{\infty}(V_m) = a_y(V_m)\tau_y(V_m)/1\text{ms}$$

and

$$\tau_y(V_m) = \frac{1\text{ms}}{a_y(V_m) + b_y(V_m)},$$

where a_y, b_y , were dimensionless, strictly monotonic functions, which we evaluated in constant time using a lookup table based on the equations and parameters of Qu et al. in Ref. [166, 165]. Additional parameters a and b can be found in these references. We have the potassium current density,

$$I_{K1T} = I_{K1}(V_m) + (1\mu\text{A}/\text{cm}^2) \frac{(V_m + 87.95\text{mV})/54.6448\text{mV}}{1 + e^{(7.488\text{mV} - V_m)/5.98\text{mV}}} + (1\mu\text{A}/\text{cm}^2) \frac{V_m + 59.87\text{mV}}{25.5037\text{mV}},$$

where

$$I_{K1}(V_m) = \frac{(1\mu\text{A}/\text{cm}^2) \frac{V_m + 87.95\text{mV}}{1.62129\text{mV}} \sqrt{\frac{[K^+]_o}{5.4\text{mM}}}}{\left(1 + e^{\frac{V_m + 28.735\text{mV}}{4.19287\text{mV}}}\right) \left(\frac{e^{\frac{V_m - 506.36\text{mV}}{16.1943\text{mV}}} + 0.49124e^{\frac{V_m + 93.426\text{mV}}{12.4502\text{mV}}}}{1 + e^{-\frac{V_m + 92.703\text{mV}}{1.94439\text{mV}}}} + \frac{1.02\text{mV}}{1 + e^{\frac{V_m + 28.735\text{mV}}{4.19287\text{mV}}}}\right)},$$

and where we have taken $[K^+]_o = 5.4\text{mM}$. We computed I_K using $I_K = I_1x$, where

$$I_1 = \left(2.837G_K \sqrt{\frac{5.4\text{mM}}{[K^+]_o}}\right) \frac{V_m - E_1}{V_m + 77\text{mV}} \left(\exp\left(\frac{V_m + 77\text{mV}}{25\text{mV}}\right) - 1\right) / \exp\left(\frac{V_m + 35\text{mV}}{25\text{mV}}\right),$$

where we have used the values $G_K = 0.423\text{mS}/\text{cm}^2$ and

$$E_1 = (10^3\text{mV}) \frac{RT}{F} \log\left(\frac{[K^+]_o + 0.01833[Na^+]_o}{[K^+]_i + 0.01833[Na^+]_i}\right) \approx -77.61\text{mV}.$$

where we took $[K^+]_i = 145\text{mM}$, $[Na^+]_i = 18\text{mM}$, $[Na^+]_o = 145\text{mM}$, $R = 8.3145\text{J}/(\text{mol}^\circ\text{K})$ as the universal gas constant, and $F = 96485.3321233100184\text{C}/\text{mol}$ as Faraday's constant. We

supposed a homeostatic body temperature of $T = 37^\circ\text{C}$ fixed. We have similarly approximated

$$E_{K1} = (10^3\text{mV}) \frac{RT}{F} \log \left(\frac{[K^+]_o}{[K^+]_i} \right) \approx 87.95\text{mV}.$$

To avoid numerical overflow when time evolving these gating variables, we treated time scales as zero, $\tau_y = 0$, whenever they took a value $\tau_y \leq 5 \cdot 10^{-4}\text{ms}$. Additionally, we evaluated I_1 using L'Hospital's Rule in the 10^{-6}mV neighborhood of $V_m = -77\text{mV}$. The conduction velocity was $c_v = 33\text{cm/s}$, which is within the electrophysiological range.

Generation and Observation of Chaotic Trajectories

The full cardiac models were simulated using finite difference methods on a spatially extended square computational domain with periodic boundary conditions. Numerical integration of Eqn. 2.14 was achieved using the body-centered forward-time explicit Euler method with the Laplacian operator discretized using a five point stencil. As stated in the main text, initial conditions contained spiral tips. Observations of spiral tip motion began 100 ms after the simulation began at time $t = 0$ so as to allow periodic boundaries enough time to become smooth. Spiral tip trajectories were determined via nearest neighbor tracking of locations determined using the following protocol based on intersecting level sets. Spiral tip positions were recorded every 1 millisecond.

The locations of spiral tips were determined from the intersection points of the level sets of constant voltage V_m using a constant threshold of $V_{\text{threshold}} = -30\text{mV}$. Level sets were determined from two frames evaluated at frames 1 millisecond apart.

Spiral tips attracted and annihilated in pairs, as is shown by the snapshots in Fig. 2.5 for both of the full cardiac models (left to right) $t' = 8\text{ms}$, $t' = 4\text{ms}$, and $t' = 0\text{ms}$ before an annihilation event. For both full cardiac models, an activation front connects two spiral tips of opposite chirality before they annihilate. A depolarized region acts as a wave block, causing the activation front to shrink in length before spontaneously dissipating.

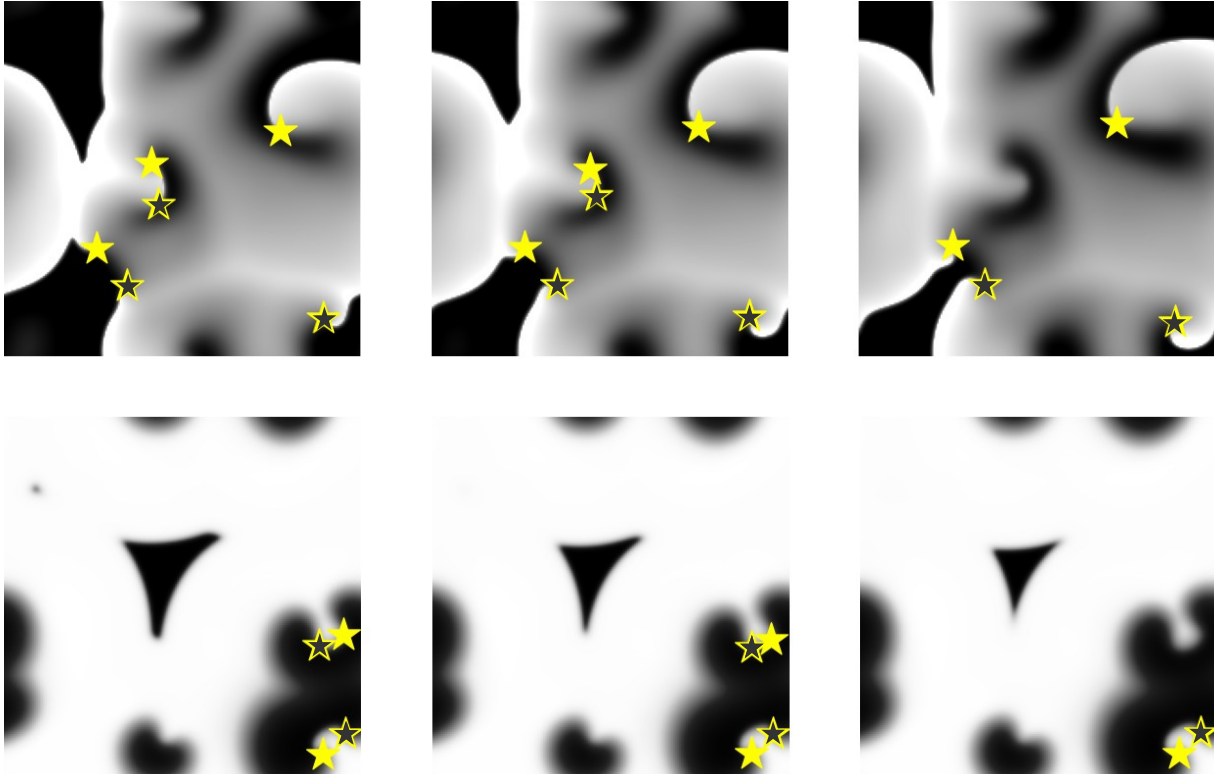


Figure 2.5. Snapshots of spiral tip annihilation. Grayscale snapshots of membrane voltage, u , showing spiral defect chaos in (top) the LR model and (bottom) the FK model with $A = 25 \text{ cm}^2$. Indicated are the tips of (black stars) clockwise and (yellow stars) counterclockwise rotating spiral waves. Snapshots were taken at (left) $t' = 8\text{ms}$, (middle) $t' = 4\text{ms}$, and (right) $t' = 0\text{ms}$ before an annihilation event. Annihilation can be explained by a wave-block resulting from a depolarized area acting as a wall to spiral tip motion.

Exponentially distributed extinction timescales

Spiral tip trajectories were generated at a fixed domain size, $A = 25 \text{ cm}^2$, and pair-annihilation events were determined by ordinary nearest-neighbor particle tracking subject to periodic boundary conditions. We defined the lifetime of a pair of annihilating particles, Γ , as the maximum temporal duration where the distance between annihilating particles was computable, as described in the main text. Repeated simulations revealed Γ was exponentially distributed for the LR model and bi-exponentially distributed for the FK model, as is shown in Fig. 2.6A. We approximated both as exponentially distributed when estimating the attraction coefficient, a , from the mean minimum lifetime reported in Tab. 1 of the main text.

Bootstrapping repeated observation of termination events demonstrated the mean termination times similarly exhibited exponential distributions, as is shown in Fig. 2.6B. Also shown are the exponentially distributed termination times predicted by the paired birth-death model. The black traces were determined by time evolving the quasistatic distribution of particle numbers according to the aforementioned master equations described in the main text. The transition rates were determined from the power law fits to $w_{\pm}(n) = M_{\pm}(n \cdot 1 \text{ cm}^2)^{\nu_{\pm}}$ reported in the main text evaluated at the same $A = 25 \text{ cm}^2$ domain size.

Detailed equations for extinction dynamics

The universal power laws reported in the main text describe the mean pair-creation rates, $W_{+2}(N)$, and the mean pair-annihilation rates, $W_{-2}(N)$, as a function of the number of particles or spiral tips. For clarity, those power laws are written explicitly as

$$W_{\pm 2}(N)/A \equiv w_{\pm}(n) = M_{\pm}(n \cdot 1 \text{ cm}^2)^{\nu_{\pm}}. \quad (2.18)$$

For periodic boundary conditions, the dynamics of extinction consists only of the creation and annihilation of spiral tips in pairs because vorticity is globally conserved. As described in Reference [212], the extinction dynamics of spiral defect chaos can be accurately modeled

through the paired birth-death process over $N = 0, 2, 4, 8, \dots$ with the master equation

$$\begin{aligned} \frac{dP(N,t)}{dt} = & W_{-2}(N+2)P(N+2,t) - W_{-2}(N)P(N,t) \\ & + W_{+2}(N-2)P(N-2,t) - W_{+2}(N)P(N,t), \end{aligned} \quad (2.19)$$

where $W_{+2}(0) = 0$ accounts for absorbing boundary conditions at $N = 0$. Due to the absorbing boundary condition at $N = 0$, no nontrivial steady state solution exists to Eqn. 2.19. However, setting the left-hand-side of Eqn. 2.19 to zero and normalizing allows us to explicitly compute the quasistationary distribution of particle numbers, $P_{qs}(N)$, in terms of the power law fits to $W_{\pm 2}(N)$. We caution the reader that an incorrect formula for this quasistationary distribution has been published previously in Ref. [212]. The correct solution is found as described in the preceding paragraph.

For both of the full cardiac models, the mean of the correct quasistationary distribution discussed here (FK: 8.1, LR: 4.3) was not significantly different from the apparent mean number of spiral tips computed directly by time averaging direct simulations of the full cardiac models, (FK: $N_{\text{avg}} = 8.1 \pm 0.7$, LR: $N_{\text{avg}} = 5.0 \pm 2.4$). Exponentially distributed termination times result from explicitly evolving Eqn. 2.19 with $P_{qs}(N)$ as initial conditions. Predicted exponential distributions of termination times are shown as black lines in Fig. 2.6B. The mean of these termination time distributions predicts a mean termination time, τ . When using directly observed birth-death rates instead of their powerlaw fits, there is not a significant difference between the predicted τ and the τ computed directly from the full cardiac models [212].

Exponential dependence of mean termination time on domain size

The mean termination time conditioned on an initial number of particles, N_0 , is written in terms of A , by substituting the power law fits directly into Eqn. 10 of the main text, resulting in

$$\tau(N_0, A) = \frac{(\tilde{A}/2)^{v_+}}{M_+ A} \sum_{k=1}^{N_0/2} \left(\frac{M_+}{M_-} \left(\frac{\tilde{A}}{2} \right)^{v_- - v_+} \right)^{k-1} \frac{k!^{v_- - v_+}}{k^{v_- - v_+}} \sum_{j=k}^{\infty} \frac{(j-1)!^{v_+}}{j!^{v_-}} \left(\frac{M_+}{M_-} \left(\frac{\tilde{A}}{2} \right)^{v_- - v_+} \right)^j, \quad (2.20)$$

where $\tilde{A} \equiv A/1 \text{ cm}^2$. Computing the mean termination time, τ is achieved by averaging $\tau(N_0)$ with respect to $P_{q_s}(N)$. Results are shown in Fig. 4E. At $A = 25 \text{ cm}^2$, the predictions (FK: 25.9s, LR: 0.51s) compared reasonably well to the apparent mean termination times (FK: $\tau = 27.8 \pm 6.5 \text{ s}$, LR: $\tau = 0.74 \pm 0.06 \text{ s}$). At $A = 100 \text{ cm}^2$, the predictions were remarkably larger (FK: $1.68 \times 10^9 \text{ s}$, LR: $8.16 \times 10^1 \text{ s}$). This is because Eqn. 2.20 increases exponentially as A is increased for both of the full cardiac models. This behavior appears independent of the initial number of particles, which is shown by taking the ratio of $\tau(N_0 = 20)/\tau(N_0 = 2)$ versus A , as is shown in Fig. 2.6C. This suggests in the limit of large domain sizes, Eqn. 2.20 can be approximated by $\tau(N_0 = 2)$ for any choice of N_0 . We remark $\tau(N_0 = 2, A)$ is a rapidly converging Dirichlet series that can be expressed in terms of the generalized hypergeometric function, ${}_pF_q$, via analytic continuation of parameters, p and q , according to

$$\tau(N_0 = 2, A) \sim \frac{(\tilde{A}/2)^{v_+}}{M_+ A} {}_{(v_+ + 1)}F_{v_-} \left(1; 2; \frac{M_+}{M_-} \left(\frac{\tilde{A}}{2} \right)^{v_- - v_+} \right) \sim \tau_0 e^{A/A_0} \quad \text{as } A \rightarrow \infty,$$

which indeed increases exponentially with A for the full cardiac models, as shown in Fig. 2.6D. As a result of this exponential dependence, a characteristic area scale, A_0 , emerged independent of any choice of A . Exponential fits for the FK model were $A_0 = 3.827 \pm 0.007 \text{ cm}^2$ at both $N_0 = 2$ and at $N_0 = 20$. For the LR model, the characteristic area was $A_0 = 13.3 \pm 0.3 \text{ cm}^2$ at both $N_0 = 2$ and at $N_0 = 20$. Also at both $N_0 = 2$ and at $N_0 = 20$, the fitted characteristic time scale was approximately $\tau_0 = 2.44 \pm 0.02 \text{ ms}$ for the FK model. For the LR model, $\tau_0 = 13.1 \pm 0.4 \text{ ms}$ for $N_0 = 2$ and $\tau_0 = 14.7 \pm 0.5 \text{ ms}$ for $N_0 = 20$.

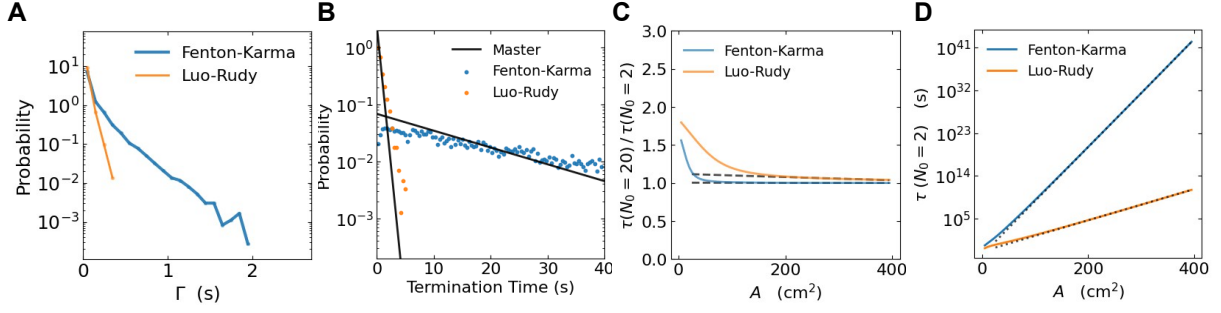


Figure 2.6. Timescales are exponential. **A** The probability density of the lifetime of annihilation events from the full cardiac models at $A = 25 \text{ cm}^2$. **B** The probability density of termination times. Black lines indicate the prediction of the paired birth-death equations for a paired birth-death process. **C** Graph of the analytic solution for mean termination time conditioned on an initial number of particles, $N_0 = 20$ divided by the same solution evaluated at $N_0 = 2$ versus domain size using the universal power laws fit to the full cardiac models. Dotted lines indicate linear fits. **D** Graph of the analytic solution for mean termination time conditioned on an initial number of particles, $N_0 = 2$ versus domain size using the universal power laws fit to the full cardiac models. Dotted lines indicate exponential fits.

Marginal dependence of force magnitudes on domain size

Spiral tip trajectories were generated at various domain sizes, A , and the attraction coefficient, a , was estimated from the apparent MSR of pairs from the full cardiac models as described in the main text. Examples of the MSR are shown at $A = 25 \text{ cm}^2$ in Fig. 2.7A and at $A = 39.0625 \text{ cm}^2$ in Fig. 2.7B. An apparent strengthening in diffusion can be seen in Fig. 2.7A-B, where increasing the domain size increases the slope of the MSR at long ranges where the attractive force becomes weak.

We observed the apparent value for a decreased, though only marginally, as A was increased as is shown in Fig. 2.7C. For the FK model, increasing A by 178% decreased a by -21%, while for the LR model, increasing A by 300% decreased a by -24%.

The sum of attractive and diffusive forces is quantified by $a + 2D$, which approximates the mean squared distance between annihilating particles divided by the quantity four times the mean lifetime of annihilation events, as discussed in the main text. We observed the apparent value for $a + 2D$ increased as A was increased, though also only marginally, as is shown in Fig. 2.7D. For the FK model, increasing A by 178% increased $a + 2D$ by 9%, while for the LR model,

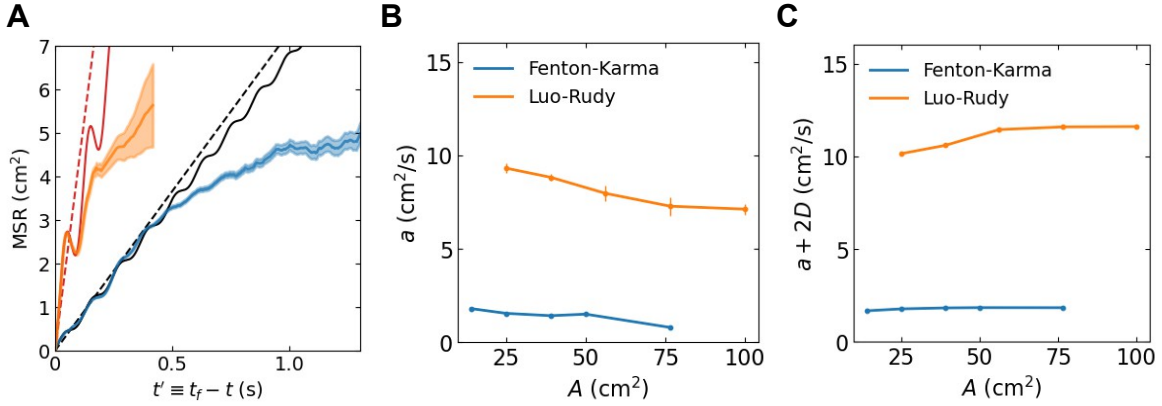


Figure 2.7. Forces are insensitive to domain size. **A** Apparent MSR *versus* time until annihilation for the full cardiac models simulated at a side length of 250 pixels ($A = 39.0625 \text{ cm}^2$). The distance between two adjacent pixels was $\Delta x = 0.025 \text{ cm}$ fixed. Symbols indicate the average of 10^3 statistically independent simulations. **B** Apparent attraction coefficient versus domain size. **C** Apparent sum of attractive and diffusive forces versus domain size.

increasing A by 300% increased $a + 2D$ by 14%. This increase in apparent force magnitude is explained by diffusion becoming effectively stronger as the domain size is increased.

This relative insensitivity of effective force magnitudes to domain size can be explained by the average distance between annihilating particles being set by local properties that are intrinsic to the full cardiac models. Therefore, it makes perfect sense that increasing an extrinsic property of the system, such as A , should have minimal effect on an intrinsic property, such as a . If attraction was somehow able to be increased by modifying the electrophysiological parameters of the full cardiac models, then the mean termination time could be decreased at larger domain sizes that might otherwise correspond to a pathological state.

Detailed Equations for Stochastic Particle Model

Let $X(t) = (X_1(t), \dots, X_N(t)) \in ([0, L] \times [0, L])^N$ be the positions at time t for N particles that move in a spatially extended square with domain size, $A = L^2$, with periodic boundary conditions. We denote $X_{ik}(t)$ as the k^{th} coordinate of the i^{th} particle at time t . The initial distribution of particles, $X(0)$, is drawn randomly from the uniform distribution over the entire domain. The points time evolve forward by $\Delta t = 10^{-2} \text{ ms}$ independently for each spatial coordinate, $k = 1, 2$,

by using the formula,

$$X_{ik}(t + \Delta t) = \left[X_{ik}(t) + \mu_{ik}(X(t), \Phi(t)) \Delta t + \sqrt{2D\Delta t} Z \right]_{\text{pbc}},$$

where $[\cdot]_{\text{pbc}}$ denotes enforcement of periodic boundary conditions, $D > 0$ is the diffusion coefficient, $Z \sim \mathcal{N}(0, 1)$ is a value both randomly and independently drawn from the normal distribution with zero mean and unit variance, and $\Phi = (\phi_1, \phi_2, \phi_3, \dots, \phi_N)$ is a vector of local phase variables that can be used to represent the oscillatory component of the attractive force between annihilating spiral tips. In the linear particle model (LPM), the k^{th} component of the impulse factor acting on the i^{th} particle is μ_{ik} , which was summed synchronously over all particles according to

$$\mu_{ik}(X(t)) = \sum_{j=1}^N \left[-\hat{a} \frac{(X_j(t) - X_i(t))_k}{|X_j(t) - X_i(t)|^2} \right]_{\text{pbc}}.$$

A key benefit to the simplicity of the LPM is that it is independent of any choice of $\Phi(t)$. Our implementation of the oscillatory particle model was the same, except we added a similar term to μ_{ik} by multiplying by an additional factor of $\cos(\phi_i(t) - \phi_j(t))$ in order to explain the distance between pairs of annihilating spiral tips in the mean square.

Annihilation was modeled by removing pairs of particles with probability, $\kappa\Delta t$, whenever they were closer than the reaction range, r . In the main text, r was fixed to the 25th percentile of the minimum ranges between non-annihilating tips. The value of r can alternatively be systematically varied with the reaction rate, κ , to fit the LPM to the mean pair annihilation rates of the full cardiac models. This is shown in Fig. 2.8A, which visualizes the likelihood of the fit for the FK model. The shape of this likelihood is explained by the following analysis.

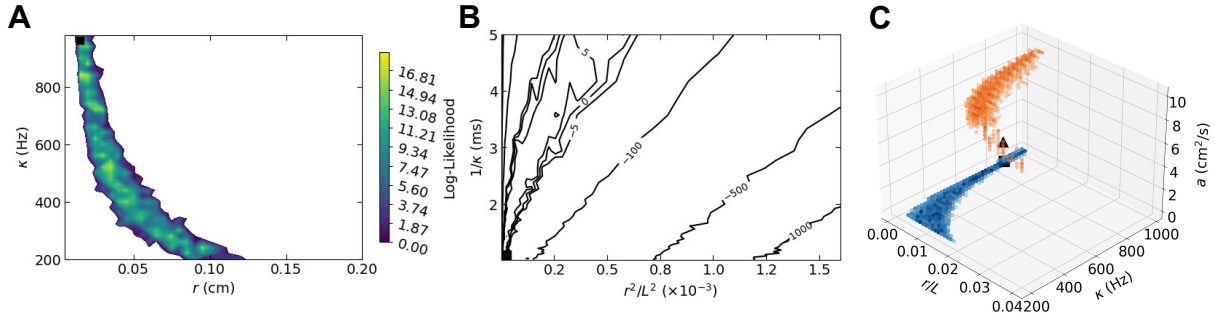


Figure 2.8. Reaction scale of the linear particle model fit to the mean pair-annihilation rates of the full cardiac models. **A** Heatmap showing log-likelihood. **B** Contour plot showing isolines of constant log-likelihood. **C** Scatter plot showing parameters supporting strictly positive log-likelihood for (blue) the Fenton-Karma model and (orange) the Luo-Rudy model. Color deepens with increasing likelihood. Indicated are maximum likelihood parameter settings for (black square) the Fenton-Karma model and (black triangle) the Luo-Rudy model.

Estimation of annihilation rate for multiple reactions

To estimate global reaction rates from local reaction rates, we first estimate the mean time until the first reaction between any two particles conditioned on an initial configuration $x = X(0)$, which we denote $\tau(x)$. Let $\kappa_{i,j}(X) > 0$ denote the rate that the i^{th} particle reacts with the j^{th} particle in the pair-annihilation reaction $X_i + X_j \rightarrow \emptyset$. We denote the overall rate of any pair of particles reacting by $\bar{\kappa}(X) \equiv \sum_{i < j} \kappa_{i,j}(X)$, where the sum considers all pairs of particles. The following expectation is computed by averaging over all paths $X = X(t)$ conditioned on the initial configuration $x = X(0)$. The expected likelihood that no reaction has occurred by time t is computed according to

$$u(x, t) \equiv \mathbb{E}_{X(0)=x} \left[\exp \left(- \int_0^t ds \bar{\kappa}(X(s)) \right) \right], \quad (2.21)$$

which has boundary conditions $u(x, 0) = 1$ and $u(x, \infty) = 0$. The expected time until the first reaction, conditioned on an initial spiral tip distribution x , is then computed by integrating by parts,

$$\tau(x) = \int_0^\infty dt u(x, t) = - \int_0^\infty dt \partial_t u(x, t). \quad (2.22)$$

The aforementioned is applicable regardless of whether the motion is deterministic or stochastic. As the prior case can be considered a special case of the latter, it suffices to estimate annihilation rate for general stochastic paths— as is done in the following for the general Langevin equation,

$$dX(t) = \mu(X, t)dt + \sigma(X, t)dB(t), \quad (2.23)$$

where $B(t)$ is standard Brownian motion in the same basis as X . Here, μ is a general drift while σ is a correlation matrix accounting for the strength of the noise. Parameters μ and σ can be found through fitting based on particle trajectories and interactions, and are intended to capture the effective forces that act on the particles. We average over paths of X using path integrals, which we compute using the Feynman-Kac formula [17, 98], which tells us that u satisfies the partial differential equation (PDE),

$$\partial_t u = -\partial_x(\mu(x, t)u) + \frac{1}{2}\partial_x^2(\sigma(x, t)^2 u) - \bar{\kappa}(x)u. \quad (2.24)$$

We will now assume that the drift μ and noise level σ exhibit no explicit dependence on t . By integrating both sides of Eqn. 2.24 from $t = 0$ to $t = \infty$, we arrive at the following time-independent PDE describing $\tau(x)$:

$$-1 = \mu(x)\nabla\tau(x) + \frac{1}{2}\sigma^2(x)\nabla^2\tau(x) - \bar{\kappa}(x)\tau(x) \quad (2.25)$$

The average first reaction time for N particles is then computed by averaging over the initial particle configurations, denoted by $\bar{\tau}_N = \mathbb{E}_x[\tau(x)]$. Using Eqn. 2.25, we can explain the linear scaling relation between M_- and $\kappa r^2/L^2$ in the large domain limit.

To study the scaling dependence of W_{-2} on κ and r , we consider the following test case where forces may be neglected. Let $\mathcal{C}(x; r)$ be the set of all pairs of particles within range, r , conditioned on initial particle configuration, x . Conditioning further on a constant number of reacting particles, $|\mathcal{C}(x; r)| = M$, the value of τ is then a constant in terms of x , $\tau(x) = (\kappa M)^{-1}$,

which implies $\nabla\tau(x) = 0$. Substituting into Eqn. 2.25 results in $\tau(x) = 1/\bar{\kappa}(x)$. The average over all initial conditions is then computed according to

$$\bar{\tau}_N = \mathbb{E}_x[1/\bar{\kappa}(x)] = \kappa^{-1} \mathbb{E}_x \left[\left(\sum_{i < j, j} \Theta(r - R_{ij}) \right)^{-1} \right],$$

which can be estimated numerically for a given N and r/L .

Consider the limiting case where x is conditioned on all N particles not being within a distance r of another particle. Randomly placing an additional particle in the domain with a uniform probability increases M to unity with constant probability, $N\pi r^2/L^2$. This probability will decrease only marginally if a few particles come within range, as the total area available to react decreases only marginally. Thus, the sensitivity of W_{-2} to N includes a factor of $\kappa r^2/L^2$. This suggests the mean annihilation rate scales according to

$$W_{-2}(N) = 1/\bar{\tau}_N \sim \kappa(N\pi r^2/L^2) f(N, L) \quad \text{as } r/L \rightarrow 0.$$

where $f(N, L)$ is a function insensitive to perturbations in r and κ . Consistency with the apparent power-law behavior requires a power law of the form, $f(N, L) = CN^{\nu-1} (1 \text{ cm}^2/L^2)^{\nu-1}$ for some constant, $C > 0$. Substituting $W_{-2}(N) = M_- L^2 N^{\nu} (1 \text{ cm}^2/L^2)^{\nu-}$ reveals the identification, $\nu = \nu_-$. Simplifying predicts the desired length-scale invariant scaling relation, $M_- \propto \kappa r^2/L^2$, which explains the linear shape of Fig. 2.8B.

Importantly, we only found good maximum likelihood fits when a was within a narrow band of values. To show this, we systematically varied the attraction coefficient, a , to find the solution set of maximum likelihood fits forms manifolds embedded in three dimensions. These manifolds are visualized in Fig. 2.8C for various choices of D overlaid. The annihilation rates were generally insensitive to the choice of D , which further underscores the importance of spiral tip attraction in describing the extinction of spiral defect chaos.

Chapter 2, in part, has been submitted for publication of the material as it may appear in

the Physical Review E, 2023, Tyree, TJ; Murphy, P; Rappel WJ. American Physical Society, 2023.

The dissertation author was the primary investigator and author of this paper.

Movie legends

- Movie S9: Grayscale movie of spiral tip motion from the Luo-Rudy model. Yellow symbols represent spiral wave tips, which create and annihilate in counter-rotating pairs. Domain size is $A = 25 \text{ cm}^2$.

Chapter 3

Cross-modal representation of identity in primate hippocampus

Navigating the complex societies that typify primates relies learning the identity of each individual in the group and their respective social relationships through observation [189]. Although evidence shows that neurons in the brains of primates and other mammals selectively respond to the identity when viewing the face or hearing the voice of a specific individual as unimodal signals [12, 156, 194, 184, 182, 33], data showing that single neurons are responsive to both the face and voice of an individual – a cross-modal representation of identity – is limited to ‘concept cells’ in human hippocampus; a sparse population of highly-selective neurons responsive to well-known individuals and locations across different views and modalities learned through observation [169, 171, 213]. These neurons are significant for several reasons including their putative role in memory functions [170] and potential uniqueness to humans [168]. Here we tested whether cross-modal representations of identity are evident in the hippocampus of marmoset monkeys by recording single hippocampal neurons [46] while presenting subjects with multiple exemplars of individual marmoset faces - from different viewpoints - and voices as unimodal stimuli, consistent with previous work [194] as well as concurrently by presenting the faces and voices from the same (identity match) or different individuals (identity mismatch): i.e. Match versus Mismatch (MvMM). Visual stimuli were presented from a monitor directly in front of the animal while a speaker positioned directly below the screen broadcasted the

acoustic stimuli. Subjects were only presented with familiar conspecifics housed in the same colony that differed in their respective social relatedness (e.g. family members and non-family members [213]).

To first test whether cross-modal representations of identity are evident in the hippocampus of a nonhuman primate, we performed the same ROC selectivity analysis described previously in humans [169, 171, 213] and revealed a population of cross-modal invariant neurons for individual identity when observing marmoset faces or voices (Figure 3.1A, 3.9A), as well as neurons selective for individual identity when viewing only their faces (Figure 3.1B, 3.9B), or hearing only their voices (Figure 3.1C, 3.9C). These identity neurons were confirmed in all hippocampal subfields (Figure 3.2A). Overall, we observed $N=148$ (9.2%) of $N=1,602$ qualifying neurons demonstrated selectivity for a single preferred individual (Figure 3.2B) with different neurons selective for faces ($N=52$), voices ($N=39$) or both faces and voices ($N=57$; Figure 3.2C). The mean area under the ROC curve (AUC) of identity neurons ($AUC=0.902\pm 0.014$) was significantly above chance ($p<0.001$, Figure 3.2D). Although these neurons in marmosets were overall less selective than in humans [169, 171, 213], this disparity may reflect species differences in the baseline hippocampus activity (Figure 3.10) that affect neural coding mechanisms for identity.

Analysis of eye-movements (Figure 3.2E) revealed marmosets' visual behavior and neural activity were differentially affected by modality and identity. Marmosets exhibited significantly shorter fixations ($p<0.001$, $N_{fixations}=18,965$; Figure 3.2F) and significantly more saccades ($p<0.001$, $N_{saccades}=2,203$) during trials with face-only relative to the voice-only trials (Figure 3.2G). These monkeys were also highly focused on faces during stimulus presentations, with faces accounting for 77.9% of viewing time and eyes specifically accounted for 37.6% of viewing time. The firing rate of identity neurons was significantly greater than the remaining neurons when subjects were looking at the eyes or face (both $p<0.001$; Figure 3.2H) suggesting that this class of neurons was particularly sensitive to faces and facial features regardless of identity. This was not, however, a broad attentional effect [138], as the firing rate of simultaneously recorded non-identity neurons did not show the same increased firing rate when gazing at faces or eyes.

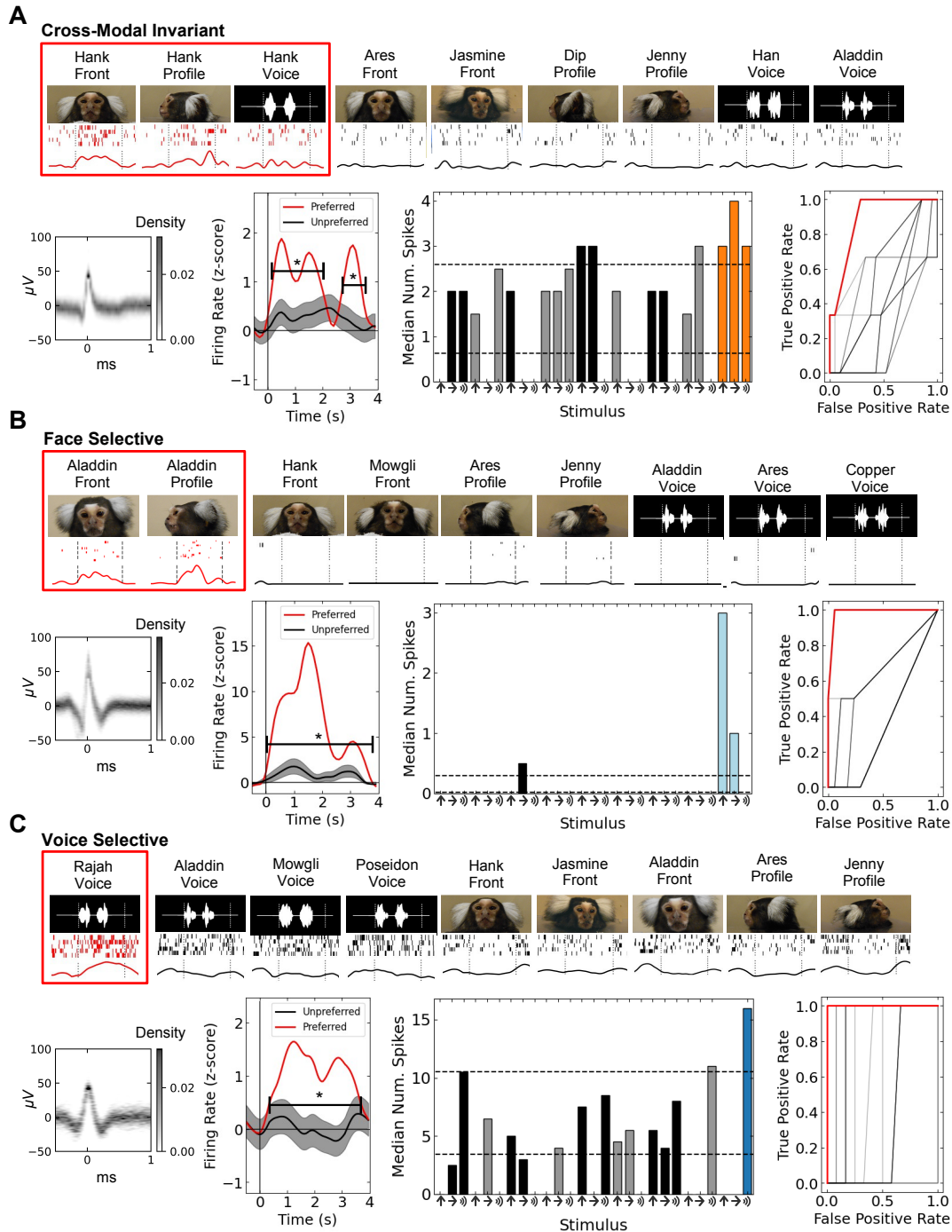


Figure 3.1. Identity neurons in primate hippocampus. [a-c] Top row: subset of stimuli shown above raster and PSTH. Bottom row: spike waveform density; normalized PSTH to all stimuli (preferred: red, nonpreferred: black), indicated are time points that show significant difference ($p < 0.05$); median number of spikes for unimodal stimuli (grey/black indicate non-preferred individuals); ROC curve (shuffled controls shown in black). Exemplar identity neurons responding selectively to [a] the face and voice of a preferred conspecific (red), [b] the face only, and [c] the voice only.

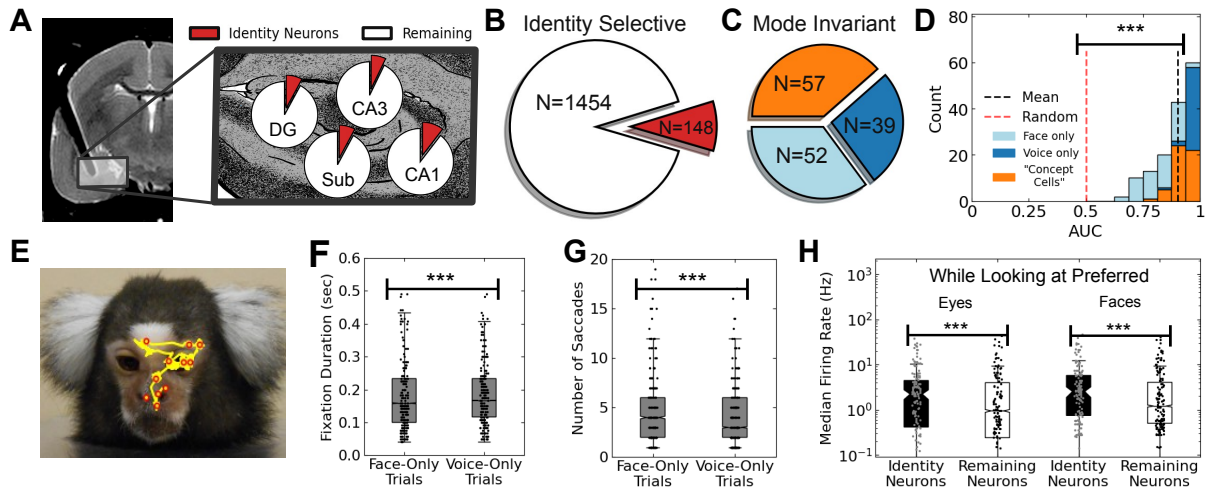


Figure 3.2. Identity neurons in primate hippocampus (cont'd). [a] Anatomical distribution of identity neurons (red) in hippocampal subfields relative to neurons remaining that responded to any stimulus (white). Black shadow indicates the electrode array track with MRI distortion artifact. [b] Pie chart showing the abundance of identity neurons in black with the number of remaining neurons that qualified for the ROC selectivity analysis in white. [c] Pie chart showing the mode distribution of identity neurons. Modes included face (light blue), voice (dark blue), and both (orange). [d] Histogram showing the distribution of areas under ROC curves comparable to red ROC curves in Figure 3.1. Colors are as in [c]. Black dotted line is the mean, while red dotted line is the mean of 10,000 random shuffles of the labels. [e] Exemplar eye-movements (yellow) with fixations indicated (red). [f] Distribution of eye fixation durations for unimodal trials. [g] Distribution of apparent saccade number for unimodal trials. [h] Distribution of median firing rates while observer was looking at eyes (left) and face (right) for identity neurons (black) versus remaining neurons (white). Three asterisks indicate a significant median difference ($p < 0.001$).

A potential parallel mechanism to highly-selective “concept cells” is for individual cells to contribute to multiple functions [179, 136], such as single neurons being sensitive to the cross-modal identity of multiple conspecifics. Previous studies show that hippocampal neurons are sensitive to mismatches between the features of a particular stimulus and previously learned category [112, 72]. To test whether a similar mechanism is evident for the learned social identities of conspecifics in marmoset hippocampus, we next analyzed whether neurons would respond differently when simultaneously observing the face and voice from the same (identity match) or different (identity mismatch) individuals. By presenting a face and voice in all MvMM trials, we controlled for the potential effects of multi-modal integration (Figure 3.11A) and instead tested whether a subordinate category– identity– elicited changes in neural activity. Analyses revealed that indeed a subpopulation of units– MvMM neurons– exhibited a significant firing rate preference for either match trials (Figure 3.3A) or mismatch trials (Figure 3.3B), with some neurons modulated only by this category distinction (Figure 3.3A) and others more generally stimulus drive (Figure 3.3B).

Overall, 21.7% of neurons (N=511 of 2,358) exhibited a significant response during MvMM trials, with significantly more units exhibiting a higher firing rate during match (N=401) than mismatch (N=110) trials ($p < 0.001$; Figures 3.4A, 3.11B). MvMM neurons were largely distinct from the identity neurons described above (Figure 3.4B). Interestingly, 56% of the neurons observed in both populations whose anatomical location could be confirmed were recorded in CA1. In contrast to identity neurons, MvMM neurons were biased to CA1 (Figure 3.4C), with N=155 (44.3%) out of 350 neurons confirmed in the CA1 qualifying as MvMM neurons. In CA1, significantly more MvMM neurons (N=129/155, 83.2%) preferred match trials to mismatch trials ($p < 0.001$). Analysis of visual behavior revealed that the MvMM neurons exhibited significantly higher median firing rate while the subject was looking at the eyes or face ($p < 0.001$, N=511; Figure 3.4D) indicating that these neurons were likewise sensitive to these socially-relevant features. Further analysis indicated that marmosets exhibited significantly more saccadic eye movements during mismatch trials (Figure 3.4E) and that this difference in behavior was most

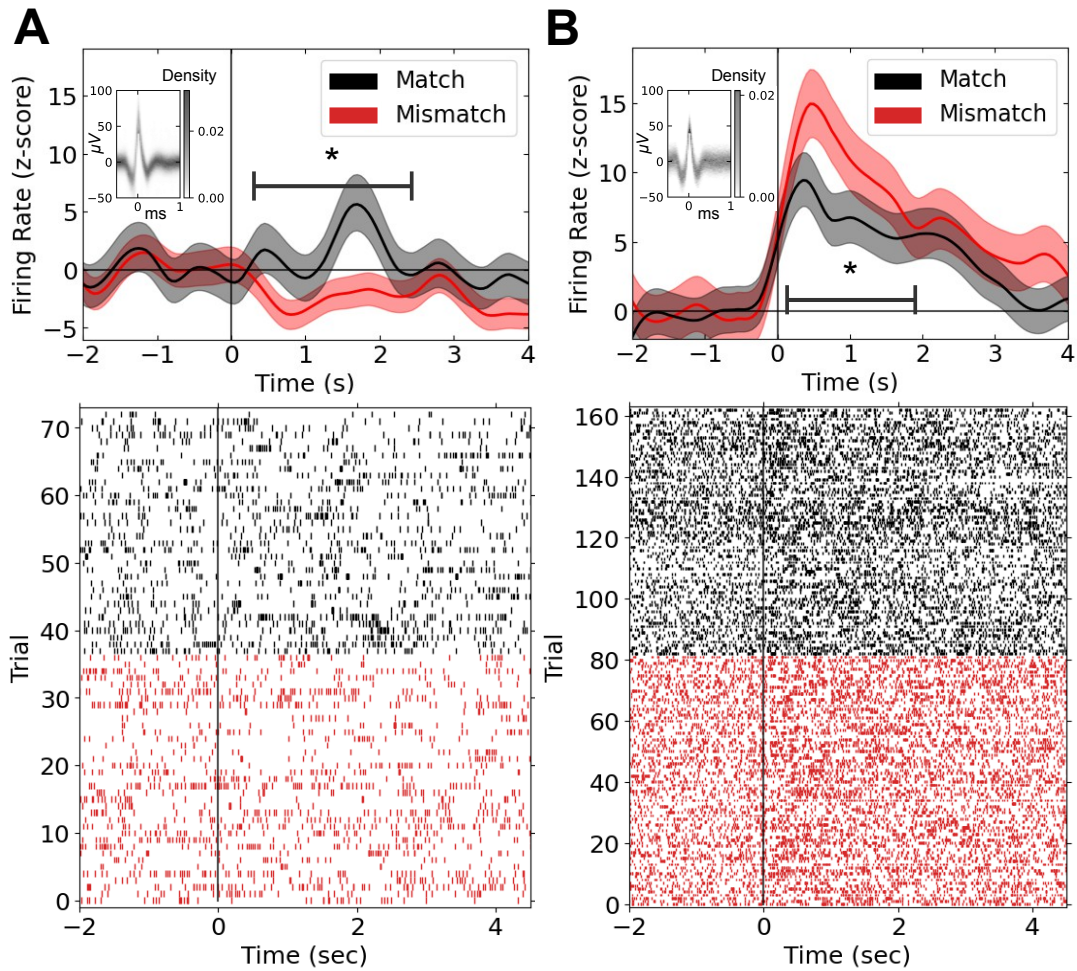


Figure 3.3. Single neurons in hippocampus represent multiple individuals. [a,b] The PSTH normalized by the pre-stimulus baseline (top) and spike raster (bottom) for two exemplar MvMM neurons. Black indicates match and red indicates mismatch trials. Vertical line indicates stimulus onset. Inset shows spike waveform density. Asterisk indicates significant time points ($p < 0.05$). Exemplar neuron with higher firing rate for [a] match and [b] mismatch trials.

prominent 1-2s after stimulus onset ($p < 0.05$, $N_{saccades} = 4,603$; Figure 3.4F) suggesting that the monkeys were perceptually sensitive to the incongruence in the subordinate category– identity– shared between cross-modal signals, consistent with the pattern of neural responses to these stimuli.

These findings suggest two seemingly distinct mechanisms for representing cross-modal identity are evident in primate hippocampus. We conjectured that more temporally selective coding mechanisms in hippocampus may inform how these two processes for encoding identity are integrated at a population level. To test this, we developed an algorithm to identify intervals of time during which individual neurons exhibited significant differences in median firing rate for a specific category ($p < 0.05$), which we labeled as predictive time bins (Figure 3.12). Importantly, this algorithm was applied to all neurons in the population, not only those classified as identity selective or MvMM neurons (e.g. Figures 3.1-3.4). We first implemented this analysis to test whether predictive time bins were selective for specific individuals when observing their face or voice. Figure 3.5A and Figure 3.13 show a pair of exemplar neurons that exhibited separate predictive time bins for two different individuals. Analyses revealed that $N = 1,634$ out of 2,358 hippocampal neurons (69.3%) exhibited at least one identity-specific predictive time bin, with the majority comprising predictive time bins for two or more individuals (Figure 3.5B).

Identity-specific predictive time bins exhibited a mean AUC ($AUC = 0.802 \pm 0.003$) that was significantly above chance ($p < 0.001$, $N_{bins} = 3,958$; Figure 3.6A). Analysis of visual behavior showed that neurons possessing identity-specific predictive time bins exhibited a significant increase in median firing rate when subjects were looking at the face of the preferred individual (Figure 3.6B). Notably, instances of face and eye viewing were highly variable and not limited to the timing of predictive time bins suggesting that attentional effects from visual behavior were not likely driving neural activity during these periods (Figure 3.14). We applied the same algorithm to test for predictive time bins that distinguished MvMM trials and found a similar result (Figure 3.6C) with 1,455 neurons exhibiting MvMM predictive time bins. Furthermore, the firing rate of neurons with predictive time bins for MvMM exhibited a significantly higher firing

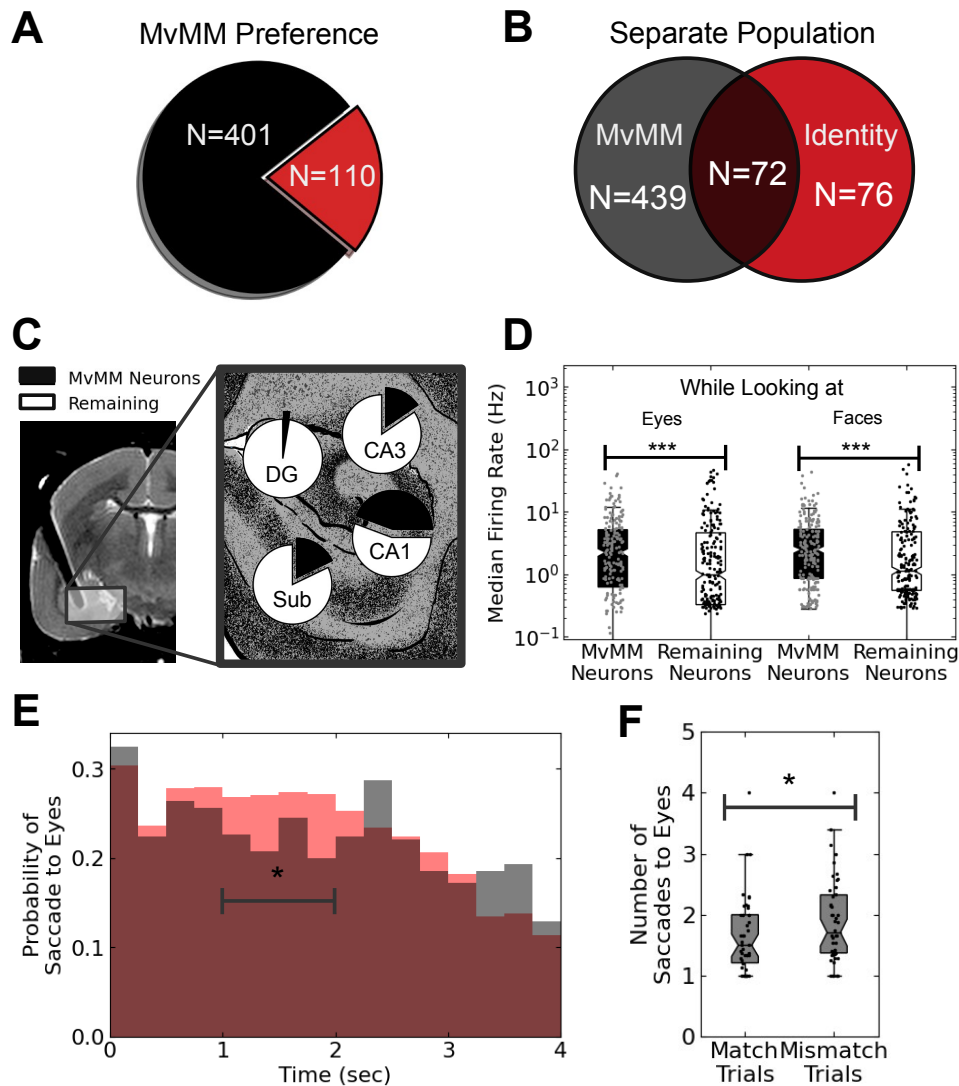


Figure 3.4. Single neurons in hippocampus represent multiple individuals (cont'd). [a] Pie chart showing the number of neurons that responded significantly more for match (black) or mismatch (red) trials. [b] Venn diagram showing the number of MvMM neurons (black) in common with identity neurons (red). [c] Relative abundance of MvMM neurons in each hippocampal subfield. [d] Distribution of median firing rate while looking at the eyes (left) and face (right) for MvMM neurons (black) versus remaining neurons (white). [e] Probability density of saccadic eye movements directed towards the eyes for match (black) and mismatch (red) trials. Indicated are the time points in [f]. [f] Distribution of apparent number of saccades to eyes. Asterisk indicates significant median difference ($p < 0.05$).

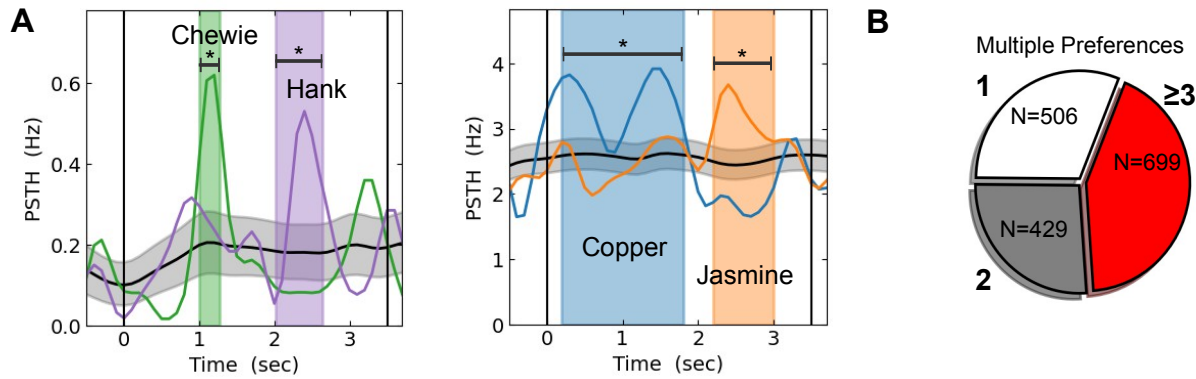


Figure 3.5. Cross-modal encoding of identity. [a] PSTH of two exemplar predictive neurons. Colored traces average over trials involving preferred individual while the gray shaded regions indicate 95% confidence intervals of the session mean. Colored regions indicate identity-specific time bins. One asterisk indicates statistical significance ($p < 0.05$). [b] Pie chart showing number of identity-specific predictive neurons that prefer one individual (white), two individuals (gray), and three or more individuals (red).

rate than other neurons when subjects looked at the face than the remaining neurons ($p < 0.001$; Figure 3.6D). We observed considerable overlap between neurons with identity-specific and MvMM predictive time bins, as 82.2% ($N = 1,196$, Figure 3.15A) exhibited predictive time bins in both analyses. These results demonstrate that information about specific identities is evident in the activity of hippocampal neurons using this more temporally refined predictive-time bin analysis.

Encouraged by these findings, we developed a stable neural decoder by combining the firing rates of predictive time bins using an ensemble of gradient-boosted decisions trees [35]. When using identity-specific time bins, we could reliably decode the identity of all marmosets when subjects observed their face or voice (accuracy: 77.4%; Figure 3.7A). Likewise, the same approach could successfully decode MvMM trials when using MvMM time bins (accuracy: 75.7%; Figure 3.7B). Interestingly, the two kinds of decoders used mostly different time points, with only $24.6\% \pm 1.5\%$ of identity-specific time bins overlapping with MvMM time bins within the same neurons (Figure 3.15B).

To test whether the same population could represent multiple cross-modal identities, we developed the identity network model (INM) that integrates these two decoding approaches.

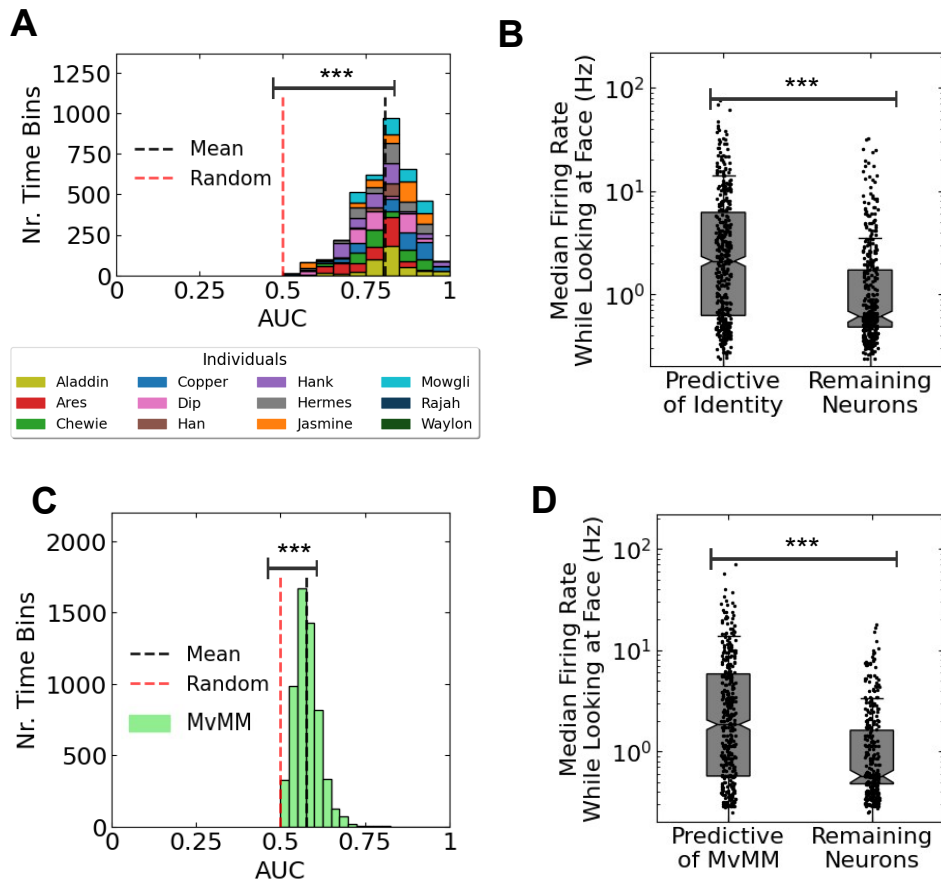


Figure 3.6. Cross-modal encoding of identity (cont'd). [a] Histogram showing AUC distribution of identity-specific time bins with colors indicating preferred individuals in legend. Dotted lines indicate the mean (black) and the control with shuffled labels (red). [b] Distribution of median firing rates while the observer was looking at the face for the identity-specific predictive neurons compared to the remaining neurons. [c] Histogram showing AUC distribution of MvMM time bins. Dashed lines indicate the mean (black) and the control with shuffled labels (red). [d] Distribution of median firing rates while the observer was looking at the face for the MvMM predictive neurons compared to the remaining neurons. Three asterisks indicate statistical significance ($p < 0.001$).

The first approach was identical to the identity-specific decoder described above, resulting in accurate decoding for each individual's face or voice. The second approach classified MvMM trials as either match or mismatch but was blind to individual identity. Our INM combined these two approaches to achieve cross-modal decoding of individual identity (Figure 3.16). This combination was critical because the identity-specific predictive population was only accurate for individual identity but performed poorly for classifying MvMM (Figure 3.7A), while the MvMM predictive population was the inverse (Figure 3.7B). When combined across individuals, the INM successfully decoded the cross-modal identity of all twelve individuals (accuracy: 84.5%; Figure 3.7C). Notably, decoding performance was at least $5\times$ above chance when distinguishing all individuals (Figures 3.7D, 3.17). Together, these results demonstrate cross-modal representations for the individual identities of multiple conspecifics are evident at the population-level in primate hippocampus [176].

Because identity neurons were included in decoding, we investigated whether their explanatory contribution was disproportionate to their sparse distribution. We compared INM performance when these neurons were removed from the analysis and separately used only in the analysis versus an equal number of other neurons, and we observed no significant effect on decoding performance despite the consideration of only individuals preferred by identity neurons (Figure 3.7E, 3.19-3.20) suggesting that these highly-selective neurons are no more significant for decoding the cross-modal identity of familiar individuals than other neurons in the population.

The success of the INM provided compelling evidence that an individual within a marmoset's social network can be decoded from their face and/or voice, but an individual's identity is also coupled to their social relationships, such as their family. To test whether hippocampus encodes categorical attributes of social identity, we applied nonlinear dimensionality reduction techniques shown to be powerful tools for revealing elements of brain functions [133], including in studies of hippocampus [147]. Using mean firing rates consistent with studies of face and voice processing in the primate brain [68], we first verified these reduction techniques were capable of

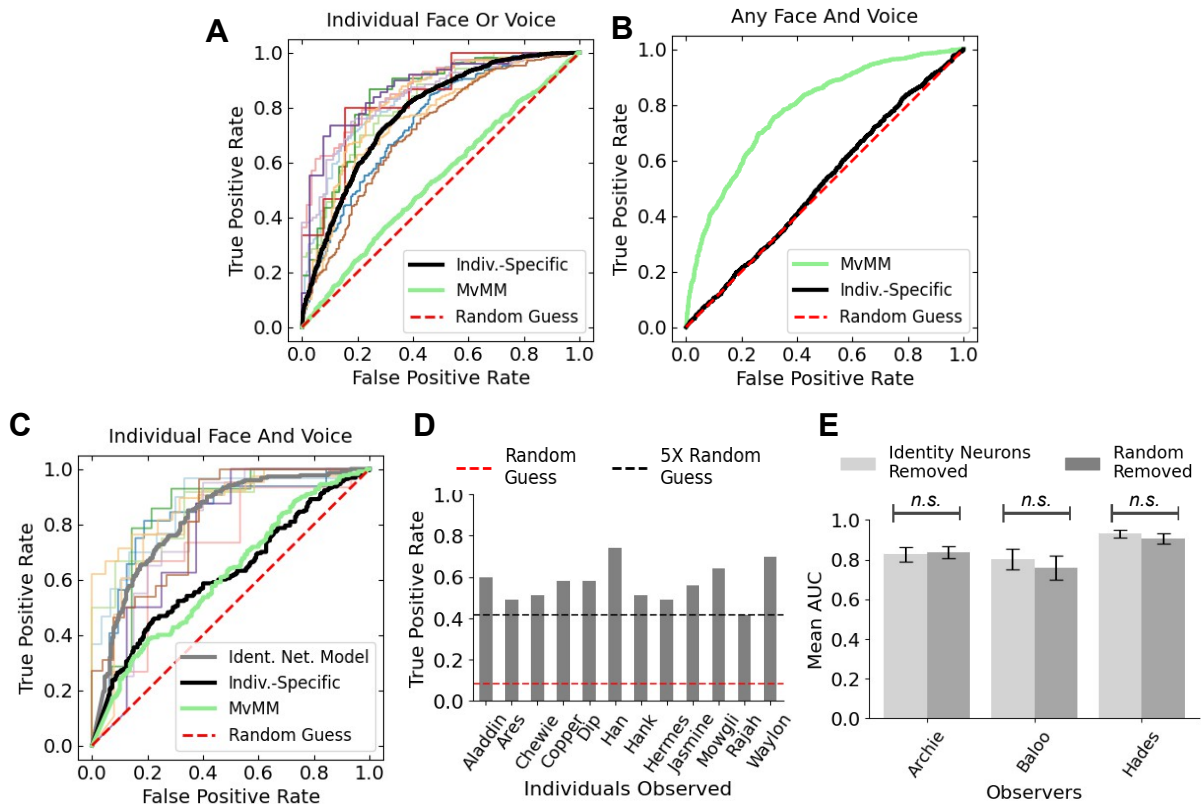


Figure 3.7. Cross-modal decoding of identity. [a] ROC curves for the detection of face or voice of individuals. Firing rates were considered from MvMM time bins (green, AUC=0.536) and identity-specific time bins (black, AUC=0.779) similarly averaged over individuals. Thinner colored lines indicate individuals as in Figure 3.4A. [b] ROC curves for the detection of match trials. Firing rates were considered from MvMM time bins (green, AUC=0.782) and from identity-specific time bins (black, AUC=0.516). [c] ROC curves for the detection of both face and voice of individuals from same 19 recording sessions as in [g,h]. Firing rates were considered from MvMM time bins (green, AUC=0.615), identity-specific time bins (black, AUC=0.622), and the INM (gray, AUC=0.818), similarly averaged over individuals. Results of the INM for individuals are shown by thin lines colored as in the legend of Figure 3.4A. Red dotted line indicates random guess as in [a,b]. [d] Bar plot showing true positive rates predicted by a winner-take-all model that considered predictions from the INM specific to twelve individuals. Indicated is the mean of the shuffled labels (red) and $5\times$ that value (black). Bar plots summarize the trials from the testing sets of 33 recording sessions ($N_{\text{trials}}=454$). [e] Bar plot showing mean AUC with identity neurons removed (light gray) versus the control randomly removing an equal number of bins from the remaining cells (dark gray). Uncertainty indicates 95% confidence of the mean. No significant difference was observed across recording sessions for any of the three qualifying subjects according to a paired Wilcoxon-Mann-Whitney test (Archie, $p=0.81$, $N_{\text{identities}}=14$; Baloo, $p=0.58$, $N_{\text{identities}}=9$; Hades, $p=0.50$, $N_{\text{identities}}=12$).

separating the stimulus categories at multiple probe locations along the anterior-posterior axis (Figure 3.21). We then replicated the findings of the INM using the same identity-specific predictive time bins for marmoset faces and voices drawn from the entire hippocampal population and showed that manifold projections similarly separated individuals (Figure 3.8A, 3.22), including for different subpopulations of neurons (Figure 3.22G).

To investigate whether representation of identity can be described by the relative timing of spikes, we computed manifold projections of spike times recorded during match trials (Figure 3.8B, left) using parameterless signed connection rate features. The signed connection rate from one neuron to another describes how it interacts with other neurons, revealing statistical distributions specific to any given pair of neurons (Figure 3.8B, right); a facet of neural activity separate from the firing rate of any single neuron. Results using this event-coded measure again revealed excellent separability for identity-match trials (Figure 3.8C), thereby replicating the effect observed with the INM using an independent facet of neural activity and further supporting cross-modal representations of identity as encoded in population-level activity in marmoset hippocampus.

Given this result, we next asked whether social categories other than identity may likewise be represented in event-coded hippocampal activity. Specifically, we tested whether representations of other marmosets' family members were distinct from non-family members for the two marmosets whose families were not included in the stimulus sets using two distinct quantifications of manifold projections, though the pattern was consistent for all subjects. First, results revealed a significant difference in the mean square range (MSR) of the manifold projections along this category boundary (Figure 3.8D, 3.23A), suggesting a larger event-coded state-space was occupied while observing family members (Figure 3.23B). Notably, while these projections were supervised, the clustering that emerged based on respective social relatedness was unsupervised. Second, we computed the unsupervised latent firing rate as the manifold projection of the absolute value of signed connection rate. Although individual identities did not separate (Figure 3.24A), we found trajectories that appeared stable in time and comparable across trials

(Figure 3.24B). The motion of mean latent firing rate significantly separated social categories at multiple time points for all subjects (Figure 3.8E; Figure 3.24C,D). Together, these results demonstrate that neural representations of social identity in primate hippocampus are not only invariant to the sensory modality and comparable over time (Figure 3.25) but low-dimensional manifolds (Figure 3.8F) can describe relationships between different social categories (e.g. individual identity, family groups, etc.) learned by observing interactions between individuals [189].

Here we showed that the cross-modal identity of multiple conspecifics is represented in the primate hippocampus. Although we identified putative ‘concept cells’ similarly to humans [169, 170], we discovered that this population of highly selective neurons is not the only mechanism for representing concepts of individuals. Rather, both single neurons and the broader population in hippocampus encode cross-modal identity of multiple conspecifics, similar to what has been reported for objects [176], suggesting that the sparse representations of ‘concept cells’ may not be the only mechanism to represent semantic memory in hippocampus. Furthermore, analyses revealed that a population-level code represents not only the cross-modal identity of multiple familiar individuals but information pertinent to social categories, as well. Similar to the role of hippocampus in other contexts [10] (Figure 3.26), these representations may support a learned schema that here applies to social identity [193, 2]. The presence of unimodal representations of identity in the primate frontal and temporal cortex [204, 156], amygdala [184, 79] and the medial temporal lobe [115] and representations of social dominance in amygdala [143] may reflect an integrative social recognition circuit in which substrates in the broader network play distinct but complementary roles that collectively govern natural primate social brain functions [67].

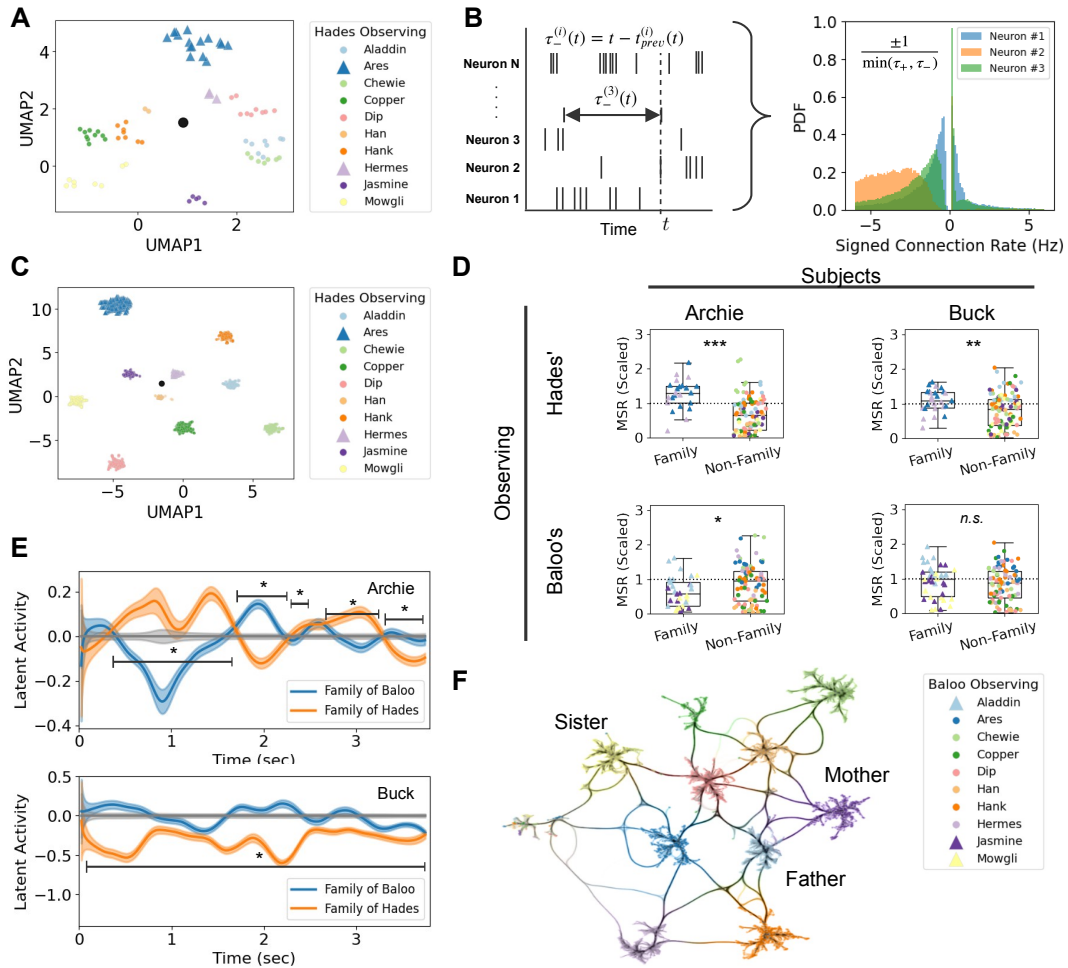


Figure 3.8. Cross-modal representation of identity using rate and event codes. [a] Two-dimensional manifold projection of our rate-coded representation computed from firing rates of identity-specific time bins. One symbol represents one identity match trial. Indicated is the mean (black). Colors in legend correspond to individuals. [b] Schematic illustrating the hindsight delay to a given neuron (left), used to generate histograms of signed connection rates to three neurons (right). [c] Two-dimensional manifold projection of our event-coded representation of identity computed as the manifold projection of signed connection rates of all neurons in the same exemplar recording session. One symbol represents one spike. Indicated is the mean (black). [d] Boxplots of MSR showing significantly different values when subjects observed family of other subjects. Shown is Archie observing family of Hades (top left, $p < 0.001$, $N_{identities} \geq 23$) and Buck observing family of Hades (top right, $p = 0.003$, $N_{identities} \geq 26$), Archie observing family of Baloo (bottom left, $p = 0.017$, $N_{identities} \geq 30$), and Buck observing family of Baloo (bottom right, $p = 0.828$, $N_{identities} \geq 37$). Significance was computed according to Student's t-test. [e] Latent activity averaged over all recording sessions from subjects Archie (left) and Buck (right). Colors indicate average over the family of Baloo (blue) and Hades (orange) relative to all conspecifics (gray). Shaded regions indicate 95% confidence of the mean estimated via bootstrap. [f] Graph of connections bundled between individuals. Triangles in legend indicate family members.

3.1 Supplementary Information

Subjects.

Four adult marmosets (2 male, 2 female) served as subjects in these experiments. All animals are socially housed with 2-8 conspecifics in the Cortical Systems and Behavior Laboratory at the University of California San Diego (UCSD). All animals housed in a cage are family members, as each cage comprises a pair-bonded adult male and female and 1-3 generations of offspring. The UCSD marmoset colony in the Miller Lab houses ~70 animals in 15 family groups in a single room with visual and acoustic access between cages. All procedures were approved by the Institutional Animal Care and Use Committee at the University of California San Diego and follow National Institutes of Health guidelines. A total of 47 recording sessions were performed with these subjects over the course of the experiment and analyzed here.

The total number of single units recorded from marmoset hippocampus totaled N=714 in Archie, N=822 in Baloo, N=212 in Buck, and N=610 in Hades (Figure 3.11B). All four subjects were considered equally in the identity neuron analysis and the MvMM neuron analysis (Figures 3.1-3.4). All subjects were considered in the predictive time bin analysis (Figure 3.5-3.7) except for Buck due to his low count of single units across his 13 recording sessions. For the manifold projection analysis (Figure 3.8), all subjects were considered while they observed families that had at least two family members from amongst the cohort of individuals shown.

Experiment design.

Neurophysiological recordings were performed while subjects were head and body restrained in our standard marmoset chair [139]. Visual stimuli were presented on an LED screen from a BenQ monitor 1080 positioned 24 cm in front of the animal. Acoustic stimuli were presented at 70-80 dB SPL from a speaker positioned below the monitor (Figure 3.27). All behavior was collected in an anechoic chamber illuminated only by the screen, which had a dynamic range from 0.5 to 230 cd/m², with luminance linearity verified by photometer. Stimulus

presentation was controlled using custom software and eye position was monitored by infrared camera tracking of the pupil. For hardware, calibration, and validation see previous work in the lab [139].

Subjects initiated trials by holding fixation of gaze for 100ms at a center fixation dot on the screen, at which point stimulus presentation was initiated. The 150ms period immediately post-stimulus was discarded to account for the time for visual signals to propagate from the retina to the hippocampus. This latency has been measured to be in the range 100-200ms [97]. This biophysical argument supports our estimate of the stimulus onset $t=0$ occurring 150ms after stimulus was presented. Unless otherwise specified, baseline firing rates were estimated from 500ms preceding $t=0$ excluding 300ms for anticipatory firing. Stimulus responses were initially measured by comparing the peristimulus baseline firing rate to firing rates averaged from the max of a 500ms sliding window from $t=300$ ms to 3.5s.

Stimuli were divided amongst unimodal– face-only and voice-only– and cross-modal– identity match and identity mismatch– on a trial-by-trial basis. Up to twelve conspecifics were represented per stimulus set (min 10, max 12). Face stimuli comprised multiple examples of each individual marmoset from different head orientation.

All face and voice stimuli were pictures or audio recordings from animals housed in the same colony room as the subjects. Because the colony is housed in a single room in which all animals have visual and acoustic interactions with each other, we assumed that all animals have sufficient experience observing each other to be familiar with their respective individual identities. Each individual marmoset was represented in multiple distinct stimuli ($N_{\text{stimuli}}=36.0\pm 15.3$) for each individual in each recording session across each of the three stimulus classes: face forward, face profile and vocalization. No single stimulus was presented to subjects more than two times in a single test session. Monkeys with fewer than 10 presentations per individual in a recording session were not considered in any analysis. The stimulus duration of trials involving vocalizations (i.e. voice-only and cross-modal) necessarily varied because each “phee” call differed in duration (mean: 3.02 ± 0.74 s). The median face stimulus duration was 3.50 seconds

(IQR: 2.78-3.51 seconds). The minimum face stimulus duration was 2.05 seconds and the maximum face stimulus duration was 4.46 seconds. Stimuli were presented in 10-trial blocks, with an inter-block active forage trial with juice reward to maintain attention. Each recording set was composed of 400 face and/or voice stimuli, split into 2 subsets.

All stimuli were composed of faces and/or voices of conspecific monkeys in our colony familiar to each subject. A total of 16 individual monkeys were represented overall (9 male, 7 female). Test subjects were not included in their own stimulus sets. Because our goal was to test for representations of individual identity rather than cross-modal perceptual integration of face/voice biomechanical movements (i.e. McGurk Effect) we presented subjects with static face stimuli so as not to introduce confounds that may emerge due to temporal misalignments of the face and vocalizations during the identity mismatch trials.

All face stimuli were photographs of monkeys from our colony taken while animals were in our standard marmoset chair with a light background behind them. The animals are trained to sit comfortably while a neck guard restricted their mobility. While seated, subjects could freely change head direction. Photographs of each subject were visually inspected and selected based on image quality and suitable representation of multiple head orientations (Figures 3.1, 3.9). Photos used as stimuli were cropped to only show the neck guard and the face/head, so as to eliminate views of the rest of the body and chair.

All voice stimuli were marmoset “phee” calls comprising two pulses, the species-typical long-distance contact calls. Previous work has shown that marmosets are able to recognize the caller’s identity when hearing “phee” calls [137]. Recordings were made at 44.1kHz sampling rate while a monkey engaged in natural vocal interactions with a visually occluded conspecific in a soundproof chamber and hand-selected using custom code. Only examples with high SNR and minimal background noise were selected for stimuli.

All analyses were performed in Python unless otherwise indicated.

Surgical and neural recording details.

The surgical procedure employed here has been described previously [46]. Briefly, we performed an initial surgery to affix a post to the skull on each animal to restrain subjects' head during experiment preparation. Following recovery, a second procedure was performed to embed the drive housing and the electrode array for stable chronic electrophysiological recording. We implanted a 64-channel microwire brush array (MBA, Microprobes) either unilaterally or bilaterally into the hippocampus using preoperative MRI stereotaxic coordinates. Electrode locations were confirmed by postoperative MRI and histology. All surgeries were performed under sterile and anesthetized conditions. The implants were inserted 7-13 degrees of angle off the vertical using the medial sulcus as reference before the operation has taken place. Neural recordings were performed with an Intan 512ch Recording Controller system via an RHD2164 64-channel amplifier chip, sampled at 30kHz. Neurophysiology data was analyzed using Spyking Circus yielding across all recording sessions 2,358 isolated units, referred to as neurons in the main text and in the remainder of Methods and Materials. Standard procedures were employed to remove obvious recording errors, which resulted in less than 1% of trials being removed from the analysis a priori.

Identifying identity neurons.

Hippocampal neurons were tested for an invariant response to individuals in the face-only and voice-only trials using an ROC analysis identical to that described in human hippocampus [169]. For each isolated single neuron we performed the analysis for all identities where at least 4 unimodal stimuli (either face or voice but not both) were presented for each of the following three unimodal stimulus categories: face forward, face profile and voice. The response of a neuron to a trial was taken to be the maximum spike count in a 500 millisecond continuous sliding time window from $t=0.3$ seconds to $t=3.5$ seconds following stimulus onset at time $t=0$. As in [169], the response of a neuron to a stimulus was the median response averaged over all

presentations of the stimulus.

A neuron was considered responsive to a stimulus if its response to the stimulus was above the responsiveness threshold, which was determined as the sum of the mean baseline plus two standard deviations (s.d.) of the baseline, where the baseline was the number of spikes averaged over the times $t=-0.8$ seconds to $t=-0.3$ seconds. This differs from the original study in humans [169], which used five s.d. instead of two, which was not practical in this study due to marmoset hippocampal neurons typically exhibiting larger baseline firing rates (Figure 3.10), for which five s.d. would have resulted in responsiveness thresholds that would only be evident in $N=166$ out of the 2,358 single units involved in this study (7.0%).

A neuron was considered cross-modal invariant to an individual if it was responsive to all three unimodal stimulus categories for that individual. If a neuron instead responded only to the voice of an individual, then it was considered voice-invariant. If a neuron instead responded to an individual for both the front facing and profile facing stimulus categories, then it was considered face-invariant.

As in [169], stimuli were considered in ROC selectivity analyses only if at least one neuron responded to it. Also as in [169], an above-threshold response to a stimulus of the preferred subject was considered a positive test. Significance of an ROC for a given subject was determined by comparison to 99 surrogate ROC curves, which resulted from randomly and independently shuffling the labels. An area under the curve (AUC) that surpassed that of all surrogates was considered significant ($p<0.01$). Neurons that met or exceeded these thresholds were necessary to determine selectivity for individual identity in marmosets. If a neuron was determined to be invariant to an individual within a given mode or modes, then selectivity was determined using the same mode or modes for that same individual. That is, cross-modal invariant neurons were tested for selectivity using all three unimodal stimulus categories, face-only invariant neurons were tested for selectivity using only front facing and profile facing unimodal stimuli, and voice-only invariant neurons were tested for selectivity using only the voice.

Cross-modal invariant neurons that passed the ROC selectivity test of [169] were considered selective for the identity and were thus labeled as putative “concept cells”. Because all voice-only unimodal stimuli were combined into a single stimulus category, voice-invariance would imply voice-selectivity for one identity if not for an additional statistical test that compared the median trial response to the voice stimuli of the preferred individual to that of all other individuals according to a one-sided Wilcoxon-Mann-Whitney test ($p < 0.01$) with an above-threshold response constituting a positive prediction of the preferred individual. The comparable test was used to determine selectivity for the face-invariant neurons. The invariant neurons demonstrating selectivity were considered identity neurons.

Identifying MvMM Neurons.

Determination of MvMM neurons was achieved by comparing the median response of a neuron to identity match trials to the median response of that same neuron to identity mismatch trials. If a neuron was responsive to either match or mismatch trials, then a statistically significant difference computed according to a Wilcoxon-Mann-Whitney test qualified a neuron as a MvMM neuron ($p < 0.05$). Preference of a MvMM neuron to match or mismatch trials was subsequently determined by a one-tailed Wilcoxon-Mann-Whitney test ($p < 0.05$). Importantly, we did not preselect for neurons that were broadly stimulus driven, but focused analysis only during the median stimulus and compared activity between match and mismatch trials. This is reflected in the exemplar neurons selected for Figure 3.3. The match preferent neuron (Figure 3.3A) shows a difference in firing rate during presentation of the stimuli but is not broadly stimulus driven. By contrast, the mismatch preferent neuron (Figure 3.3B) exhibits stimulus driven activity as well as differential firing rate between the stimulus types.

Identifying predictive time bins.

Hippocampal neurons were analyzed in terms of their firing rate response during time bins that we identified as candidate time bins. For each neuron, our procedure consisted of three

stages. The first stage was to generate a large list of time bins of varying duration using an extension of a sliding window approach. The second stage identified a subset of time bins as having a general ability to distinguish trials. We required this subset to be mutually disjoint. Candidate time bins resulted from the third stage, which varied each time bin independently according to our refining procedure.

The first stage extended the sliding window approach by using 200ms time bins evenly distributed between 0 and 3.6 sec, the maximum stimulus duration (Figure 3.12A). Time bins of duration greater than 200ms were constructed by joining adjacent time bins, leading to a maximum allowed time bin duration of 3.6 seconds. A general ability to weakly distinguish trials was determined by splitting the training trials according to three-fold stratified cross-validation and then computing the training AUC of each fold (Figure 3.12B). Training AUC was initially computed from the ROC curve that resulted from an above-threshold firing rate response determining a positive trial. Separately, training AUC was computed from a below-threshold firing rate response as determining a positive trial. In either case, if the training AUC was greater than chance ($AUC > 0.5$) for all three folds, then the time bin was retained for stage two. The same convention for above versus below firing rate response as determining a positive trial was used for stage two and for stage three. All population-level decoders were blind to this convention of sign.

The second stage selected a disjoint set of candidate time bins, optimizing for their ability to distinguish trials by maximizing the mean AUC averaged over the same three folds. To achieve this, time bins were selected in decreasing order of their mean AUC and included only if doing so maintained the disjointness of time bins.

To reduce the effect of discretizing the trial into time bins, the third stage refined the resulting disjoint set by considering a number of random perturbations of each remaining candidate time bin and keeping only the optimal perturbation. The random perturbations shifted the start times and the end times independently by a random amount identically sampled from the normal distribution with zero mean and standard deviation equal to the duration of the

unperturbed time bin. We generated a sample of $N=100$ perturbed time bins and removed those with a duration $<10\text{ms}$. Perturbations were additionally removed if they exhibited a start time before stimulus onset $t=0$ or if they exhibited an end time after $t=3.6$ seconds. A worsening AUC in any of the folds resulted in rejection of the given candidate time bin.

If any of the resulting training AUC values were smaller than that of the unperturbed time bin, then that perturbation was removed from consideration. The overall training AUC was computed for each perturbation using all training trials together. The perturbed time bin with the largest overall training AUC was kept instead of the unperturbed time bin. Perturbed time bins were allowed to overlap with other remaining time bins, thereby relaxing the condition of disjointness for the sake of parallelizability, which is statistically valid because zero spike times in the training set appear in the testing set and the decoder makes no assumption of independence of features. A flowchart summarizes the time bin refinement procedure (Figure 3.12C). If no perturbations remained under consideration, then the unperturbed time bin was kept from stage two. Any remaining candidate time bins were considered predictive only if they presented a statistically significant difference in median firing rate for the true (e.g. identity match) training trials compared to the false (e.g. identity mismatch) training trials. Significance was determined according to $p < 0.05$, where p was the statistic computed as the mean p-value resulting from a Wilcoxon–Mann–Whitney test conducted over the training trials averaged over five stratified cross-validation folds over training, which was a sufficient statistic in the sense that all time bins with $p < 0.05$ also exhibited a statistically significant difference in median value at the same level of significance according to a Wilcoxon-Mann-Whitney test conducted over all MvMM trials. This procedure provided the features used in our population-level decoders.

Training the population-level neural decoders.

Population-level decoders were trained on the training trials before computing predictions for the separate testing trials. Decoders were trained and tested on a Quadro RTX 5000 GPU typically in less than five seconds of runtime. The population-level decoders trained using firing

rates directly as inputs. Neither translating nor scaling of the firing rates was performed, as the decoders were both location and scale invariant [35]. The prediction was estimated by the weighted average of values returned by an ensemble of gradient-boosted decision trees relative to a default value of one half (controlled by `base_score` in Table 3.1). For each training epoch, at least 25 decision trees were trained (controlled by `num_parallel_tree`). While a unique solution exists for a given decision tree, a heuristic algorithm was used to approximate the unique solution using the quantile method of [105].

Decision trees were trained to minimize the binary cross-entropy loss function (equivalently, to maximize likelihood) at the ensemble-level by considering only a fraction of the training trials (controlled by `subsample`). Decision node rules considered only a fraction of the input firing rates (controlled by `colsample_bynode`) to determine placement of its weight. The weight of a node was limited to a certain amount (controlled by `max_delta_step`). The complexity of the decision node rules was further limited using linear and quadratic regularization (controlled by `reg_alpha` and `reg_lambda` in Table 3.1, respectively).

Each decision tree was gradient boosted in the sense that nodes were recursively added in accordance with an estimate of the gradient of a training loss computed at the ensemble-level. If inserting a decision node failed to improve the loss by a sufficiently large amount (controlled by `gamma`), then that decision node was removed from the tree. To further limit structural complexity, the maximum tree depth was set to no more than five decisions (controlled by `max_depth`). The weight for a new decision tree was scaled down by a factor (controlled by `learning_rate`). Training terminated for a given decision tree when the total weight for the next decision node was smaller than a certain amount (controlled by `min_child_weight`). After all decision trees terminated training, the training epoch was complete. After a fixed, predetermined number of training epochs, the ensemble terminated training. Then, predictions were computed for the testing trials (Figure 3.16A). Predictions were used to evaluate the predictive ability of a given set of one or more predictive time bins in terms of AUC.

Determining hyperparameter settings for the population-level neural decoders.

The parameter settings for our population-level neural decoders resulted from a series of coarse grid searches each conducted over a wide range of settings for one pair of hyperparameters at a time. Each parameter setting considered five-fold stratified cross-validation involving the training trials only with the goal of maximizing mean testing AUC. Early stopping was used during this tuning procedure, which supported a minimum 60 training epochs for the match vs mismatch (MvMM) predictive population and a minimum 67 training epochs for the identity-specific predictive population as sufficient according to early stopping. By increasing the number of training epochs, stability of performance became immediately apparent for up to 500 epochs for both MvMM and identity-specific decoders. We made no use of early stopping anywhere else apart from the hyperparameter tuning procedure described here. This hyperparameter tuning procedure was conducted only on the training trials for Archie observing Waylon in one recording session from subject, Archie (session #8). Archie (male) and Waylon (female) were not family members— though they likely knew each other in the colony. These training trials (from session #8) were complementary to testing trials from no more than one of the multiple recording sessions summarized in Figure 3.7. The hyperparameter settings that resulted are reported in Table 3.1.

Summarizing testing performance from multiple predictors.

Population-level decoders were trained as MvMM or identity-specific predictors for each individual identity in each recording session involved in Figure 3.7. To account for variations in prediction magnitude between decoders, predictions were scaled linearly to a maximum value of unity before combining ROC traces in the multiple recording sessions summarized in Figures 3.7A-C,E and 3.19-3.20. No such scaling was involved with the multiclass predictions reported in Figures 3.7D and 3.17. Sampling trials for multiple predictive populations from the same recording session. For a given recording session, the following criteria were respected

Table 3.1. Neural decoder hyperparameter settings. Numerical values were passed as keyword arguments to the constructor of `xgboost.XGBClassifier` instances [35]. Columns correspond to the two types of predictive populations reported in this study.

	MvMM	Identity-Specific
<code>base_score</code>	0.5	0.5
<code>num_parallel_tree</code>	25	50
<code>subsample</code>	0.2	0.2
<code>colsample_bynode</code>	0.1	0.1
<code>max_delta_step</code>	0.5	1
<code>reg_alpha</code>	0.4	0.3
<code>reg_lambda</code>	0.4	0.3
<code>gamma</code>	0.1	37
<code>max_depth</code>	5	2
<code>learning_rate</code>	0.9	0.6
<code>min_child_weight</code>	0.5	1

while partitioning testing trials from training trials involving the identity network model (INM) discussed in the main text. Testing trials for the INM were also testing trials for both the MvMM decoder and the identity-specific decoders. Because stimuli involving individuals were sampled uniformly, the frequency of a given individual could be small for a given recording session. To account for this, individuals were considered only if they exhibited at least forty appearances in a given recording session.

Because of the uniform nature of our uniform random sampling of trials over the larger space of cross-modal stimuli, each recording session had relatively few trials involving both the face and the voice of a particular individual. This resulted in far more negative trials being presented to the observer relative to the number of true trials for the INM. This was also the case for both the MvMM decoders and the identity-specific decoders reported in Figures 3.7 and 3.17-3.20. All three binary classification tasks had balanced samples randomly selected, which were then randomly shuffled before 30% were randomly selected to be testing trials. The remaining 70% of trials were considered for training. Unbalanced sampling in the training set was accounted for by scaling the positive weights by a factor of 5 for the MvMM decoders and 100 for the identity-specific decoders. Decoders involved in Figure 3.7 used 200 training

epochs, all of which were used in testing decoder performance except the first training epoch. The only exception was the identity-specific decoders involved in evaluating the INM for the winner-take-all model in Figures 3.7D and 3.17, which considered all 500 training epochs.

Decoding multiple identities using a winner-take-all model.

We used the winner-take-all model to predict the identities of multiple individuals shown during identity match and face-only trials. The twelve individuals summarized (Figure 3.7E) have their detailed testing performance reported (Figure 3.17). The winner-take-all model predicted the correct identity with an overall testing accuracy of 91.0% ($N_{trials} = 454$). For a given recording session, the following procedure was performed to generate the predictions for the winner-take-all model. First, we identified all identities involved in a sufficient number of identity match trials ($N_{trials} \geq 12$). All identity match trials involving the identities identified were shuffled and 30% were randomly selected as testing trials to be withheld from training with the remaining 70% of trials.

We considered predictions of our INM to approximate a predicted probability that a given trial from the testing set involved the given identity. The presence of the individual was modeled using the decoder outputs in the winner-take-all model if the INM had the sufficient number of predictive time bins available. After repeating this procedure for all individuals in the recording session, the predicted identity of the winner-take-all model corresponded to that of the maximum predicted value (Figure 3.16B).

Quantifying relative contribution of identity neurons in decoders of preferred identities.

To investigate the possibility of identity neurons exhibiting any clearly observable significance in the INM at the population-level, we removed all identity neurons from consideration and recomputed the testing predictions of Figure 3.7C for each individual that was statistically preferred by an identity neuron. After recording the testing AUC, we repeated a comparable

procedure as a control that randomly removed an equivalent number of predictive time bins from any neuron that was not found to be an identity neuron. This control procedure was repeated many times ($N_{samples} = 200$) and then averaged to estimate the mean control testing AUC, which was not significantly different from a normal distribution according to D'Agostino-Pearson's omnibus test ($p > 0.05$, $N_{samples} = 200$). The aforementioned control and test procedures were conducted using independent randomized samples.

ROC curves were computed with above-threshold values indicating a positive trial for the three observers with at least two family members amongst the identities presented. The INM appeared successful despite the removal of identity neurons independently for multiple observers (Figure 3.20). Removing identity neurons from the INM for all recording sessions involving one observer resulted in a mean testing AUC that was not significantly smaller than that of the control according to a one-tailed paired student's t-test that supposed identity neurons contributed more to decoding than other neurons. We independently replicated this same statistical insignificance of identity neurons at the population-level for multiple observer subjects ($p > 0.05$, $N_{observers} = 3$). This insignificance was consistent with a comparable analysis that made no assumption of normality, which suggested the median testing AUC was also not significantly smaller when all identity neurons were removed relative to the control ($p > 0.05$, $N_{observers} = 3$). It is uncertain whether this insignificance can be attributed to these identity neurons being observed in nonhuman primates, as no comparable predictive time bin analysis has ever been performed in humans to the knowledge of the authors.

Generating random time bins from the non-predictive population.

Time bins were randomly selected for neurons uniformly drawn from the population that exhibited zero predictive time bins (the 'non-predictive population'). Time bins possessed start and end times drawn from a uniform random sample from $t=0$ to 3.5 seconds, the latter of which was the median stimulus offset time. Time bins with a duration briefer than 0.2 seconds were immediately removed from consideration. The number of random time bins involved in

Figure 3.18A was equal to the number of predictive time bins involved.

Quantifying of the effect of restricting the abundance of predictive time bins.

To systematically vary the relative abundance of predictive time bins, we randomly sampled time bins from the non-predictive population. Their firing rates were concatenated with those of all predictive time bins with at least 75 match trials and 75 mismatch trials. We took a random sample of predictive time bins in addition to a statistically independent random sample of time bins from the non-predictive population. The relative sizes of the samples were chosen to reflect a given relative abundance of predictive time bins. Testing accuracy was computed at the same relative abundance over many statistically independent samples ($N=100$) in order to estimate the mean testing accuracy conditioned on the relative abundance of predictive time bins considered by the decoder. Uncertainty in mean testing accuracy was estimated by bootstrapping that same sample of testing accuracies, resulting in 95% confidence intervals less than 1% for both traces reported in Figure 3.18A. Many random time bins ($N_i=105$) were independently generated for this analysis in order to estimate the mean testing accuracy at the 1% minimum relative abundance reported in the main text while simultaneously involving the entire aggregated predictive population. The fold with the median testing performance ($AUC=0.9911$) provided the predictive time bins ($N=347$) and the aggregated trials ($N=150$) that were used to quantify the effect of restricting the number of predictive time bins in Figure 3.18B.

Computing signed connection rate.

Our event-coded representation relied on our signed connection rate measure, which we computed using our two primitive event measures. The first we referred to as the hindsight delay, $\tau_- > 0$, which is the amount of time since a given neuron has spiked. The second we refer to as the foresight delay, $\tau_+ > 0$ which is the amount of time until a given neuron will spike. A schematic illustrating the computation of the hindsight delay is shown (Figure 3.8B, left). A

similar computation is found for the foresight delay by time inversion. If the given neuron has not yet spiked, then we take the hindsight delay to approach infinity. Similarly, if the given neuron was not observed to spike again, then we take the foresight delay to approach infinity. Note that our primitive event measures do not evaluate to non-positive real numbers.

The magnitude of our signed connection rate is the multiplicative inverse of the minimum of the hindsight delay and the foresight delay. Finally, we set the sign of our signed connection rate to be negative if the hindsight delay was used. Using the standard conventions of real analysis, our signed connection rate is now well-defined at all times for all neurons that exhibited at least two spikes. Equivalently, our signed connection rate was computed according to a real function of two variables

$$c(\tau_+, \tau_-) = \frac{\Theta(\tau_- - \tau_+)}{\tau_+} - \frac{\Theta(\tau_- + \tau_+)}{\tau_-},$$

where $\Theta(x) = 1$ if x is nonnegative, otherwise, $\Theta(x) = 0$. We evaluated our signed connection rate for every neuron at the spike times of the neuron that spikes the most over the recording session (i.e. the reference neuron). This was our attempt to measure how a single neuron “connects” with any other neuron. In doing this, we observed statistical distributions that appeared specific to a given neuron pair (Figure 3.8B, right). We considered a given neuron to have an approximately symmetric signed connection rate if it exhibited no more than twice as many negative values as positive values in these statistical distributions.

Estimating manifold projections.

We used uniform manifold approximation and projection (UMAP) to compute our manifold projections in Figure 3.8 of the main text, which presents descriptive manifold projections computed from predictive firing rate features and separately from our signed connection rate measure of spiking events. The same parameter settings on the same optimization algorithm was used for both rate and event-coded manifold projections. We used the identity-specific predictive

time bins in the rate-coded representation. The rate-coded manifold projections considered neuron spikes from $t=0$ to 2 seconds after the stimulus onset. Similarly, the event-coded manifold projections considered neuron spikes from $t=0$ to 2 seconds after the stimulus onset. The average predictive time bin from the MvMM predictive population reported in Figure 3.4 was centered from $t=0$ to 2 seconds after the stimulus onset, with approximately half of predictive time bins ending earlier, which supports 2 seconds as a reasonable choice for the max time considered by the rate and event-coded manifold projections.

The UMAP algorithm was composed of two steps that can fruitfully be described as graph construction and graph projection [133]. The graph was constructed from a given set of comparable observations. The graph was projected to a low-dimensional space of real numbers. The output was embedded in twenty-four-dimensional real space for statistical analyses and two to three dimensions for visualizations. In the optimization procedure, five negative samples were selected for each positive sample. The minimum distance between two observations was set to 0.1Hz. The number of nearest neighbors was initialized to 50 for rate-coded representations and 1000 for our event-coded representations. Repulsion strength was initialized to unity. Local connectivity was set to 1Hz in estimating probability distances. We trained for 200 epochs at a learning rate initialized to unity. The resulting function was equipped with a learned graph of the data, which projected to the manifolds visualized in Figures 3.8, 3.22, 3.25 and 3.26. An example of connections from such a learned graph were visualized (Figure 3.8F).

For our rate-coded manifold projections, the inclusion of predictive time bins ($p < 0.05$) appeared sufficient for the separation of individuals (Figure 3.22A), which was supported by computing the minimum distance between the centroid of any individual and then comparing across multiple recording sessions. Minimum distances that were computed from predictive time bins exhibited a significantly smaller median value when compared to candidate time bins that were not predictive ($p > 0.85$) according to a Wilcoxon-Mann-Whitney test ($p < 0.001$, $N_{sessions} = 29$), suggesting predictive activity leads to better separation of individuals in comparable rate-coded representations (Figure 3.22B). Shown are examples of rate-coded manifold projections that

used predictive firing rates as trial-by-trial observations. Event-coded manifold projections used signed connection rates as spike-by-spike observations for Hades (Figure 3.22C,D) and for Baloo (Figure 3.22E,F) in addition to Archie (Figure 3.25A-C) and Buck (Figure 3.25D-F).

Estimating latent firing rate.

Our latent firing rate was computed using unsupervised nonlinear dimensionality reduction of the absolute value of the signed connection rate for all neurons that had no less than one third of its computed signed connection rate values as positive (i.e. approximately symmetric). In computing the latent firing rate, we used a method of nonlinear dimensionality reduction that made no assumption of uniformity, which was achieved by passing the keyword argument, `densmap=True` to the manifold projection constructor, `umap.UMAP`, in the Python programming language. The output metric and the input metric were both Euclidean (flat), which supports the output having the same units as the input. The output was embedded in six-dimensional real space and the first three dimensions are visualized in Figure 3.24A for an exemplar recording session. After this output was computed at the spike times of all neurons involved, it was analyzed as a time series by time ordering the data according to evaluation time.

By considering latent firing rates evaluated at the times $t=0$ to 4 seconds after a stimulus onset, we observed relatively stable trajectories for multiple recording sessions conducted over multiple observers. Shown are three exemplar identity match trials, where Baloo observed the face and voice of her mother, her father, and her sister as shown in Figure 3.24B. We performed a median filter with a sliding window of 50 neuron spikes before plotting our estimates of the latent firing rates.

Generating the hammer bundle plot.

The graph of connections bundled between individuals in Figure 3.8F represents the learned graph associated with an event-coded representation of identity analogous to Figure 3.8C. The procedure for generating the shape of Figure 3.8F was achieved using the Python function,

umap.plot.connectivity with the keyword argument, `edge_bundling='hammer'`. Coloration was achieved by multiplying the resulting image with a color mask. The color mask resulted from passing the colored scatter plot of the event-coded representation through a Gaussian filter using the GNU Image Manipulation Program, which was also used for the image multiplication.

Determining anatomical positions of implants.

All implants were followed by at least one postoperative MRI (Figure 3.28). The scans were aligned to anatomical features with RadiAnt Dicom viewer and the position along the anterior-posterior axis was determined by measurement from the center of the array to the ear canal. Because implants were stereotactically performed coronally, all recordings for a given array were assigned the same anterior-posterior (AP) position.

Because of the 1mm spread of the microwire brush arrays, it was difficult to precisely estimate the position of any given electrode, or indeed the entire bundle on a particular day. We used the position of the tip of the electrode from each MRI and extrapolated the trajectory by estimating position along the drive axis by cross-referencing with contemporaneous notes made of the date and distance of every movement of the drive. Based on a centroid at each estimated position, we chose particular sessions for we had the greatest confidence that the majority of the array was located predominantly in one or two hippocampal fields. Because the relative positioning of individual electrodes was not clearly observable, all reported analyses were developed to be agnostic to neuron location.

Confirming implant location by MRI.

MRI was performed at the UCSD Center for Functional Magnetic Resonance Imaging in a 7.0T Bruker 20cm small animal imaging system using Advance II software. Preoperative images were analyzed in Osirix DICOM Viewer and stereotactic coordinates were established using a pair of saline-filled barrels affixed above the putative posterior end of temporal sulcus (marked on the skull during headcap surgery). Array positioning and tract trajectory was verified

by post-operative MRI. Follow-up scans were performed occasionally to update array position.

Determination of anatomical positioning was performed using RadiAnt DICOM Viewer (Medixant, n.d.). Stereotactic alignment was performed using a number of clearly defined and readily identifiable anatomical landmarks. 2D coronal slices were made vertical by rotating to align the medial longitudinal fissure with a vertical line. Yaw was corrected by re-slicing the coronal plane to align both interaural canals. Pitch correction was performed by re-slicing MRI so that the 4th ventricle was aligned vertically with the isthmus of the corpus callosum.

Position on the anterior-posterior axis was calculated relative to the interaural canal. Measurement was taken from the coronal slice at which the array first entered the hippocampal complex (Figures 3.2A, 3.4C). Arrays were implanted with as little pitch as possible, so AP position variability is negligible along the electrode trajectory.

Electrode positions are not precisely determinable with our brush arrays, as microwires are not visible at the resolution of the scans and individual tips are not individually distinguishable by any practical means available. Electrode splay of the 64-ch MBA in tissue was measured at approximately 1mm, so we approximated electrode position by use of a 1mm spherical voxel centered at the tip of the array.

We used a Microdrive with a $500\mu\text{m}$ thread pitch that could reliably make controlled movements with a precision of $30\text{-}40\mu\text{m}$. An array tip was identified for every MRI in each subject and position was extrapolated based on contemporaneous notes regarding electrode movement. Once putative array centroids have been hand-tagged they were assigned to one of the hippocampal subfields. Centroids were deemed to be in a hippocampal subfield if more than 70% of their volume fell within that area, as assessed by hand-traced MRI. Recording sessions where the centroid fell significantly between two subregions were not counted in anatomical analyses. CA2 and CA3 were combined due to insufficient granularity in this methodology and resolution in our scans to effectively differentiate them. Figure 3.15 shows the estimated position of each electrode array in the hippocampus for all subjects.

Acknowledgements.

Chapter 3, in full, is a reprint of the material as it appears in Science. 2023. Tyree, TJ; Metke M; Miller CT. American Association for the Advancement of Science (United States), 2023. The dissertation author was the primary investigator and author of this paper.

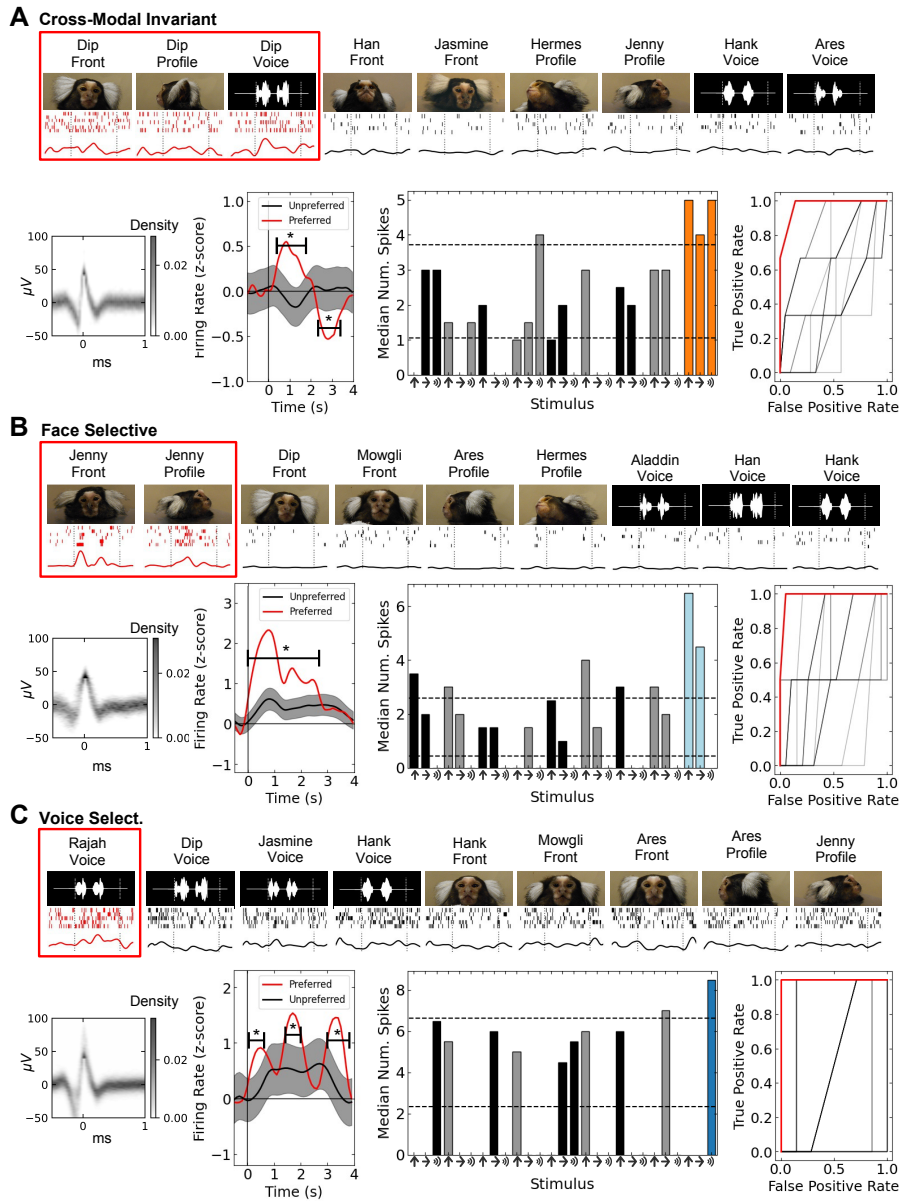


Figure 3.9. Additional Identity Neurons in Primate Hippocampus. Shown are exemplar identity neurons that are [a] cross-modal invariant, [b] face-selective, and [c] voice-selective comparable to Figure 3.1. [a-c] Top row: subset of stimuli shown above raster and peristimulus time histogram (PSTH). Bottom row: spike waveform; normalized PSTH to all stimuli (preferred: red, nonpreferred: black), indicated are time points that show significant difference ($p < 0.05$); median number of spikes for unimodal stimuli (grey/black indicate non-preferred individuals); ROC curve (shuffled controls shown in black). PSTH was normalized by the pre-stimulus baseline, and shaded regions indicate 95% confidence intervals. Indicated are time points that show a statistically significant difference in mean ($p < 0.05$). Horizontal dotted lines indicate mean background firing rate and responsiveness threshold.

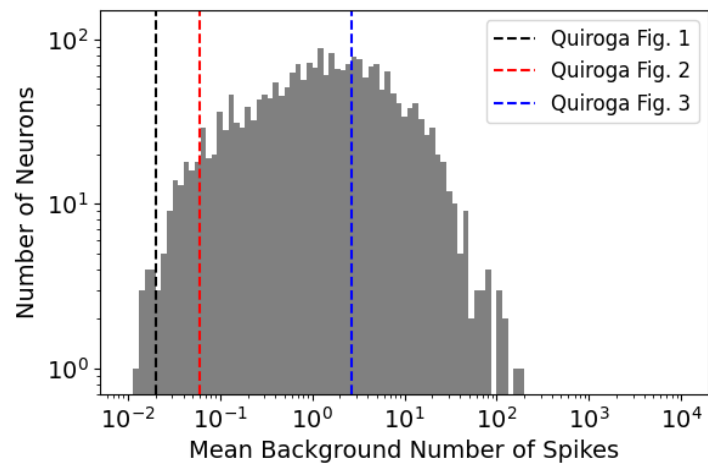


Figure 3.10. Marmoset hippocampus neurons have high baseline firing rates. Shown is a histogram of the mean background spike counts computed for all neurons involved in this study. The dotted lines come from the mean baselines reported in the main figures from Quian Quiroga et al., Nature (2005), which summed over 700ms instead of 500ms. We confirm all recorded neurons are considered in this histogram.

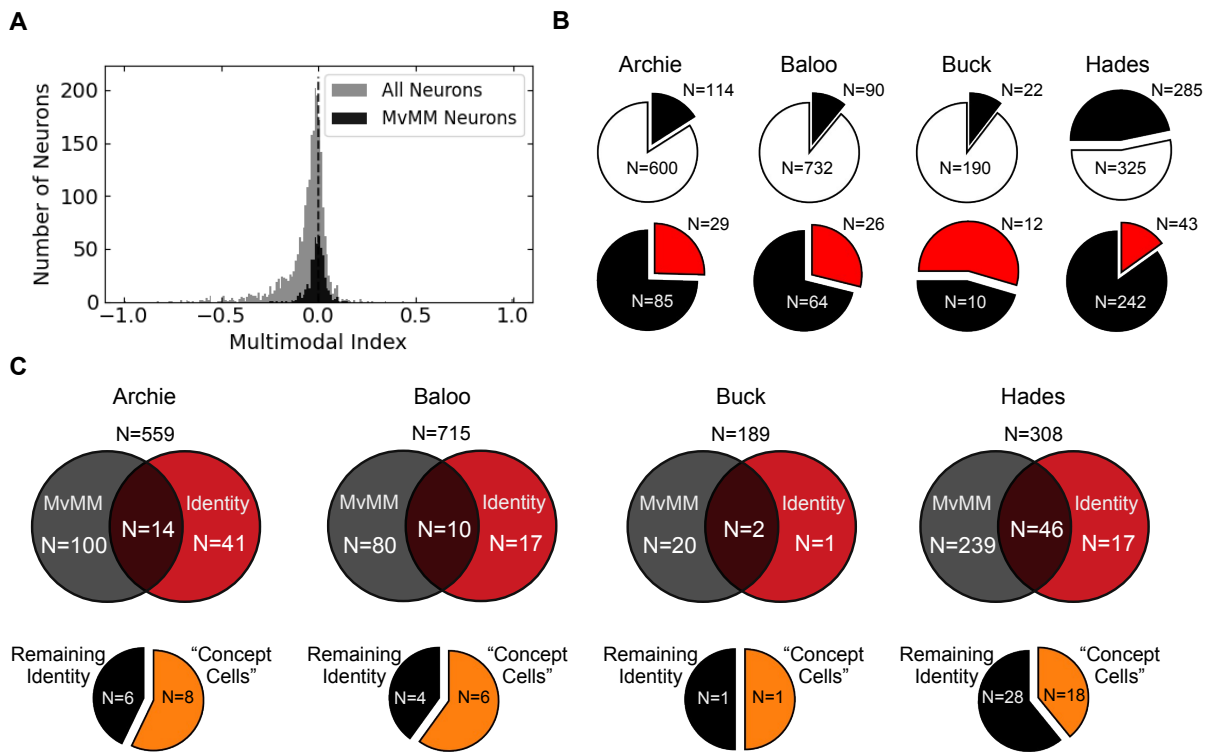


Figure 3.11. Match versus Mismatch Neurons [a] Histogram showing the multimodal index of MvMM neurons (black) and all recorded neurons (gray). Neither the mean nor median multimodal index was significantly greater than zero for either population ($p > 0.05$, $N \geq 499$). The multimodal index was not well defined for $N=12$ out of 511 MvMM neurons due to small response. Zero is indicated by the black dotted line. Bin width is 0.01. [b] Pie charts showing the abundance of MvMM neurons averaged over all recording sessions for each observer involved in this study. Shown is the number of MvMM neurons (black, top) amongst all other recorded neurons (white, top) and the number of identity-match preferring MvMM neurons (black, bottom) amongst the identity-mismatch preferring MvMM neurons (red, bottom). The CA1 region was only confirmed in $N_{sessions} = 4$ out of 8 of the recording sessions from Hades. [c] Shown are (top) Venn diagrams and (bottom) pie charts that show the composition of populations investigated in the main text. (top) Venn diagram overlaps represent the abundance of (black) MvMM neurons in common with (red) identity-selective neurons, which exhibited a relative abundance of putative ‘concept cells’ as represented by the orange color in (bottom) the pie charts. Results are shown for each subject involved in this study. Furthermore, the number of MvMM neurons in common with MvMM predictive neurons was 359, while the number of MvMM neurons in common with the identity-specific predictive neurons was 388.

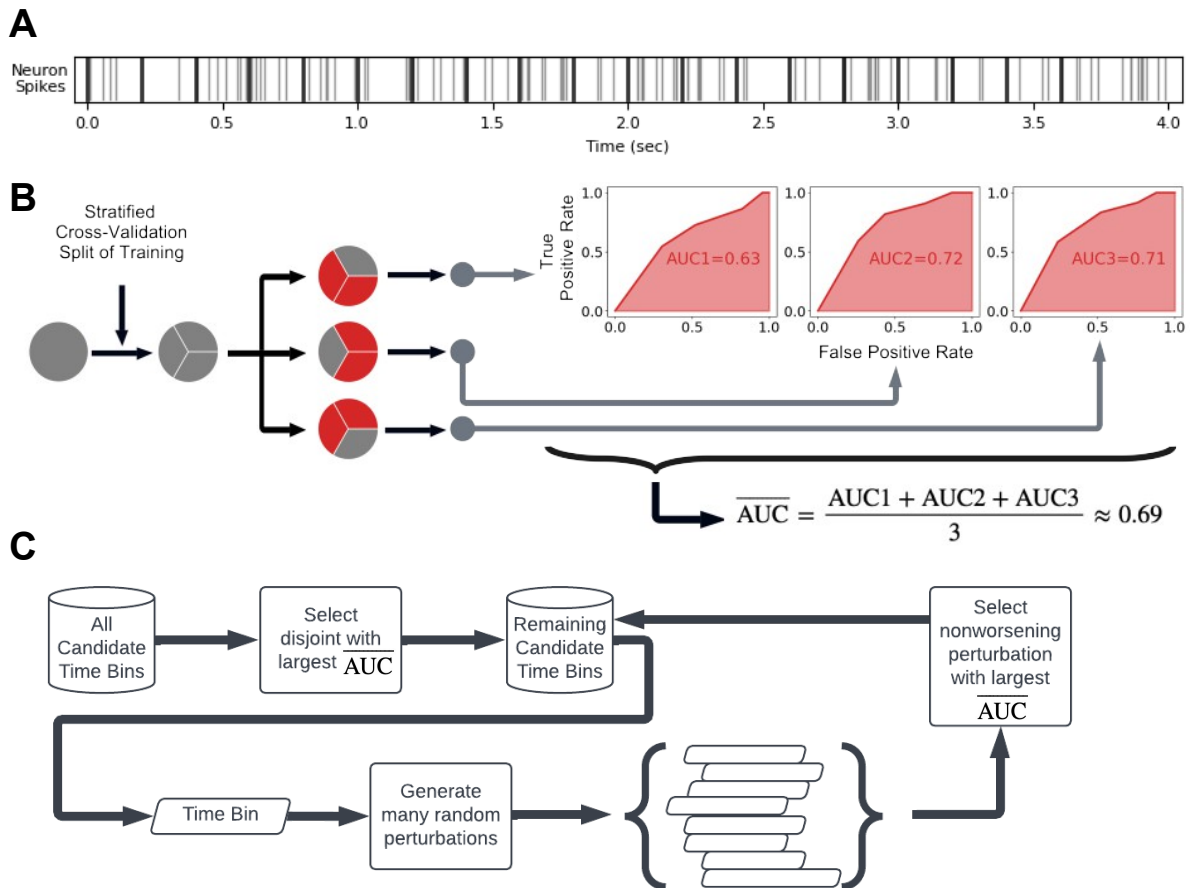


Figure 3.12. Identification of predictive time bins. [a] Schematic showing (gray) the spike times of an example neuron firing versus time after the stimulus onset at $t=0$. Indicated are (black) start and end times of time bins before the refinement procedure. [b] Flow chart showing training trials being split by stratified cross-validation to result in multiple receiver operator characteristic (ROC) traces. Each training fold resulted in an area under the curve (AUC), which were then averaged to produce the mean training AUC as an estimator of the general ability of a time bin to distinguish true trials from false trials. Time bins satisfying a list of properties were considered as candidate time bins (described in Methods). [c] Flow chart showing the procedure that resulted in all predictive time bins (described in Methods).

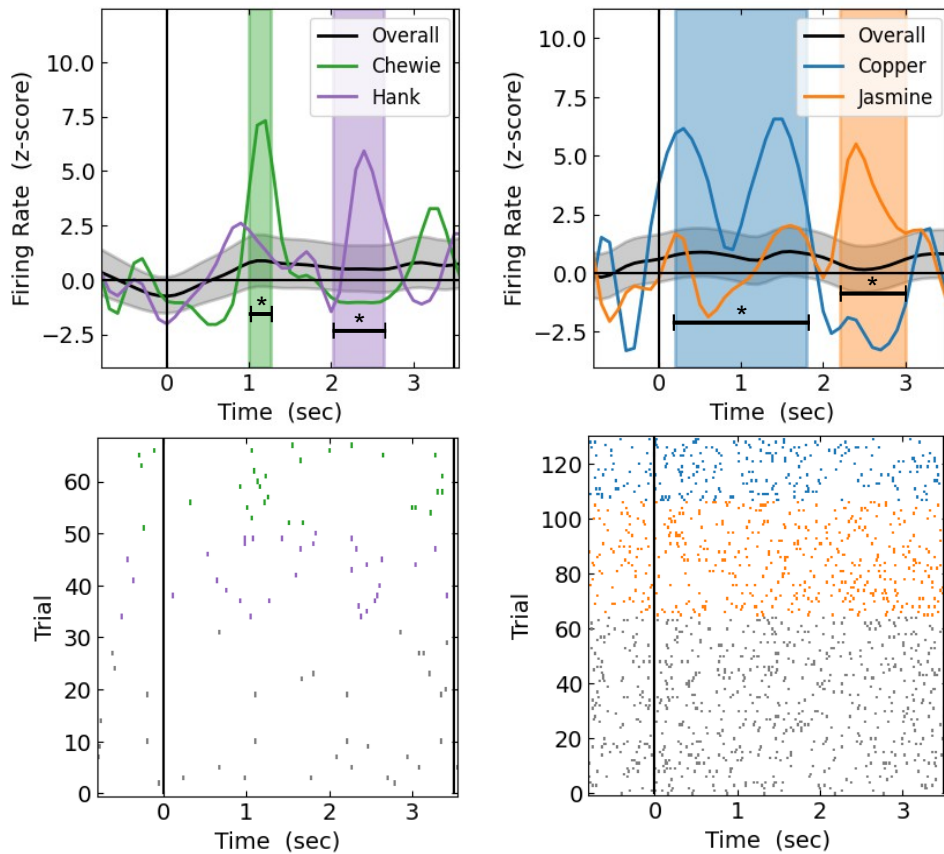


Figure 3.13. Exemplar predictive neurons. Shown are (top) PSTH traces and (bottom) spike rasters for two predictive neurons that each prefer at least two individuals. Shaded regions indicate predictive time bins, which exhibited a significantly different median firing rate for their preferred identity ($p < 0.05$). Colors correspond to legends. The number of trials shown for Overall is matched in the plot to the number of trials for the two selective individuals.

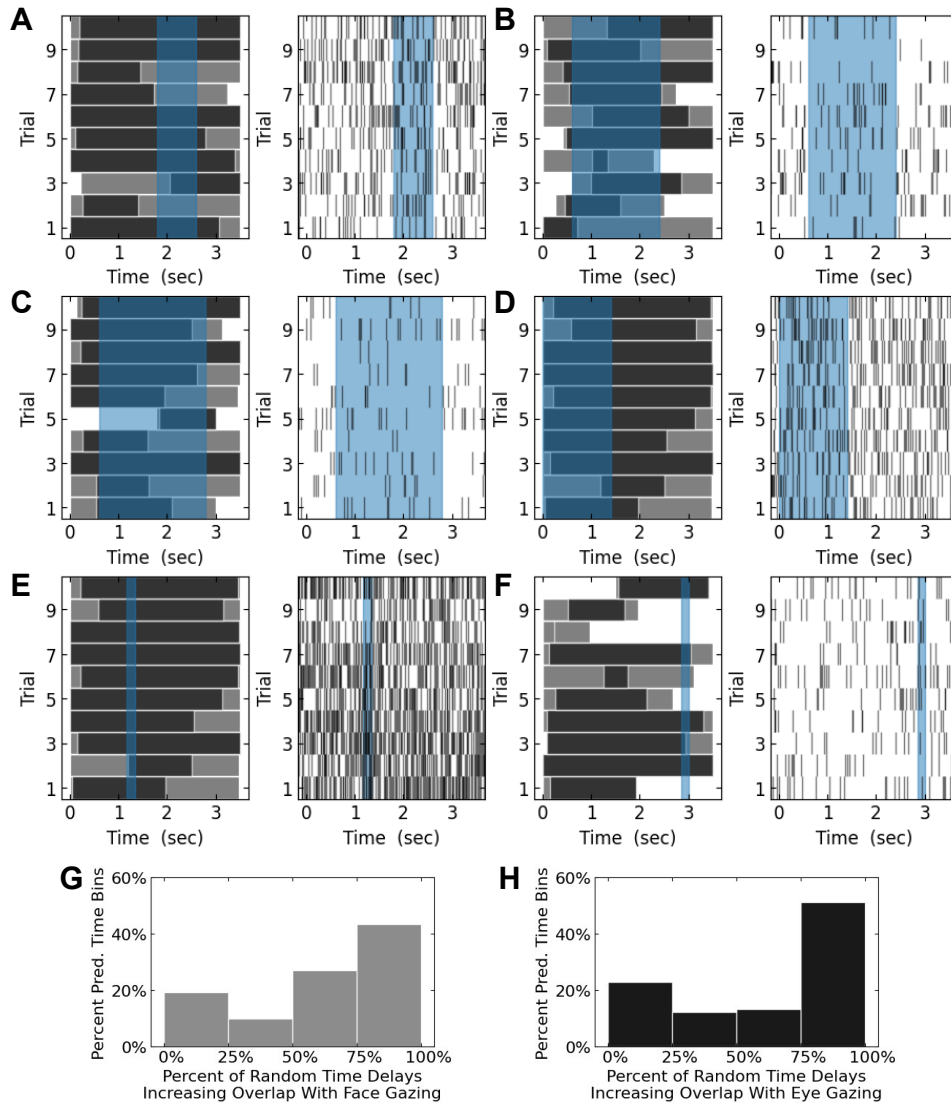


Figure 3.14. Variability of visual behavior relative to identity-specific predictive time bins. [a-f] Shown are visual behavior rasters (left) and spike rasters (right) for six predictive time bins. Blue shaded regions indicate the identity-specific predictive time bin. Gray indicates face gazing while black indicates eye gazing in the visual behavior rasters. Trials represent repeated presentations of the same front-facing unimodal stimulus. Unimodal stimuli were chosen to agree with the identity preference of the predictive time bin. [g-h] Histograms showing the relative abundance of random delays that increased the amount time in common between the time bin and time spent gazing at preferred faces (g, gray) and time spent gazing at preferred eyes (h, black). Bar height shows the percent of identity-specific predictive time bins, where each time bin had at least 10 presentations of at the same unimodal face-only stimulus where both eyes of the preferred individual were clearly visible ($N_{bins}218$). More area in the right two bars indicates perturbing the time bins typically decreased overlap with visual behavior.

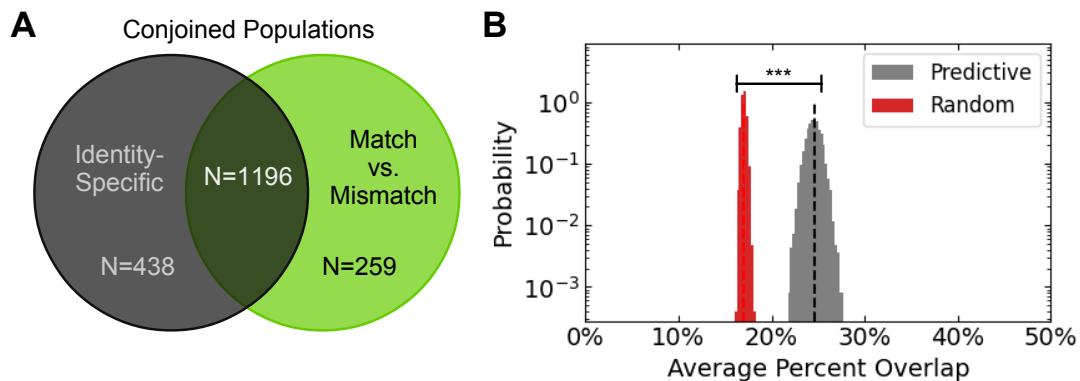


Figure 3.15. Conjoined predictive populations. [a] Venn diagram showing the abundance of predictive neurons in common between the identity-specific predictive neurons (black) and the MvMM predictive neurons (green). [b] Histograms showing the probability density of the average percent overlap of the identity-specific predictive time bins with the MvMM predictive time bins from the same neurons (gray) and of an equal number of uniformly distributed pairs of random time bins as control (red). Indicated is the total duration of overlap divided by the total duration of identity-specific predictive time bins, $(612.3\text{s}/2493.7\text{s})=24.6\%\pm 1.5\%$ (black dashed line), which was significantly greater than control ($17.0\%\pm 0.5\%$; red dashed line) according to Student's t-test ($p<0.001$, $N_{\text{samples}}=10,000$). Control uniformly sampled pairs of time bins on the interval from $t=0$ to $t=3.5$ seconds following stimulus onset. The bin width is 0.25%.

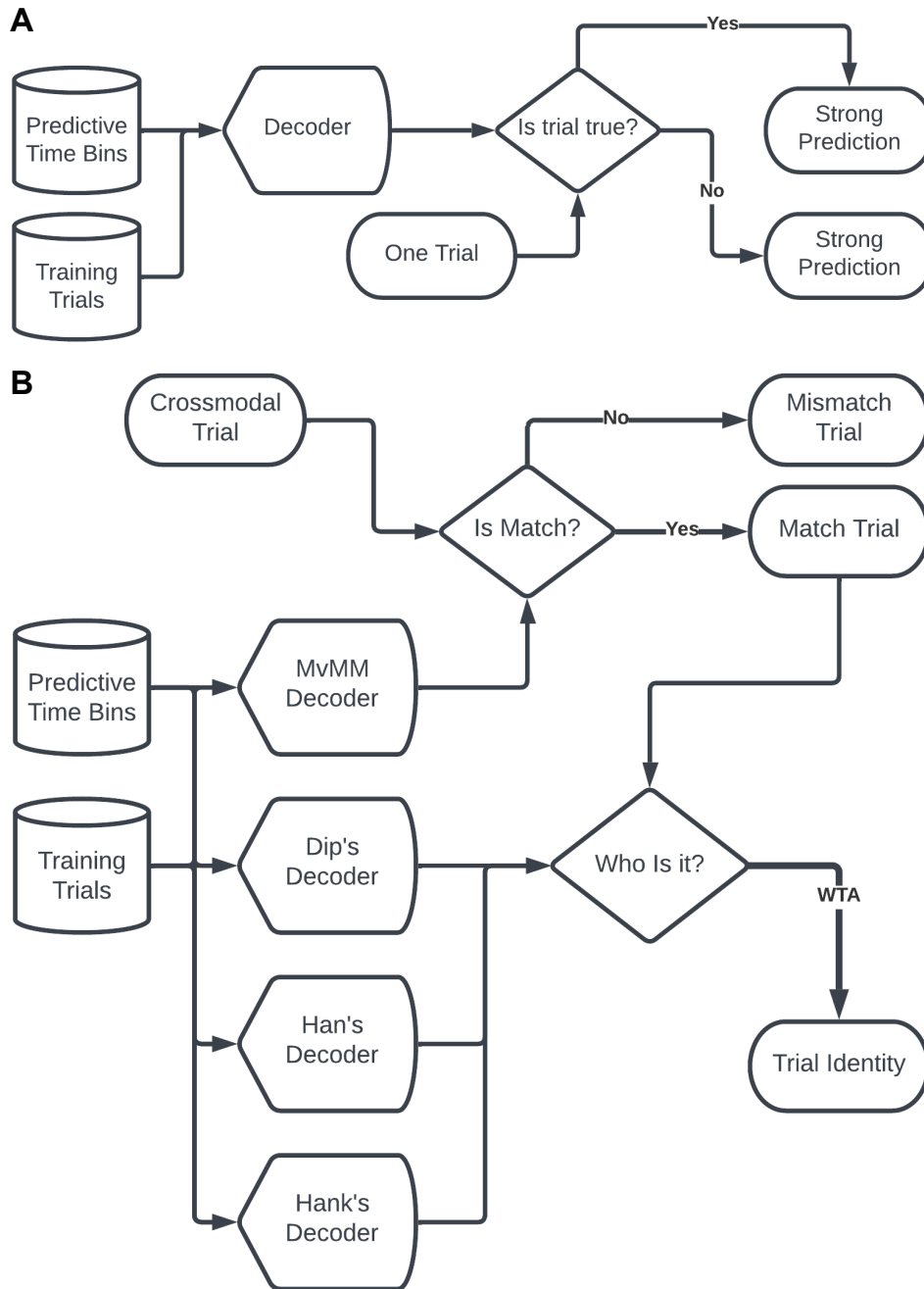


Figure 3.16. Decoder Schematics. [a] Flow chart showing predictive time bins were combined with the training trials that were used to determine the predictive time bins to train a decoder for classifying trials as either true or false. The decoder then produced remarkably strong predictions on novel trials. [b] Flow chart showing the winner-take-all model resulting from a MvMM decoder and one identity-specific decoder for each individual. Cross-modal trials were categorized as either match or mismatch trials. The identity of the match trial was then predicted as that of the decoder with the largest output via winner-take-all (WTA).

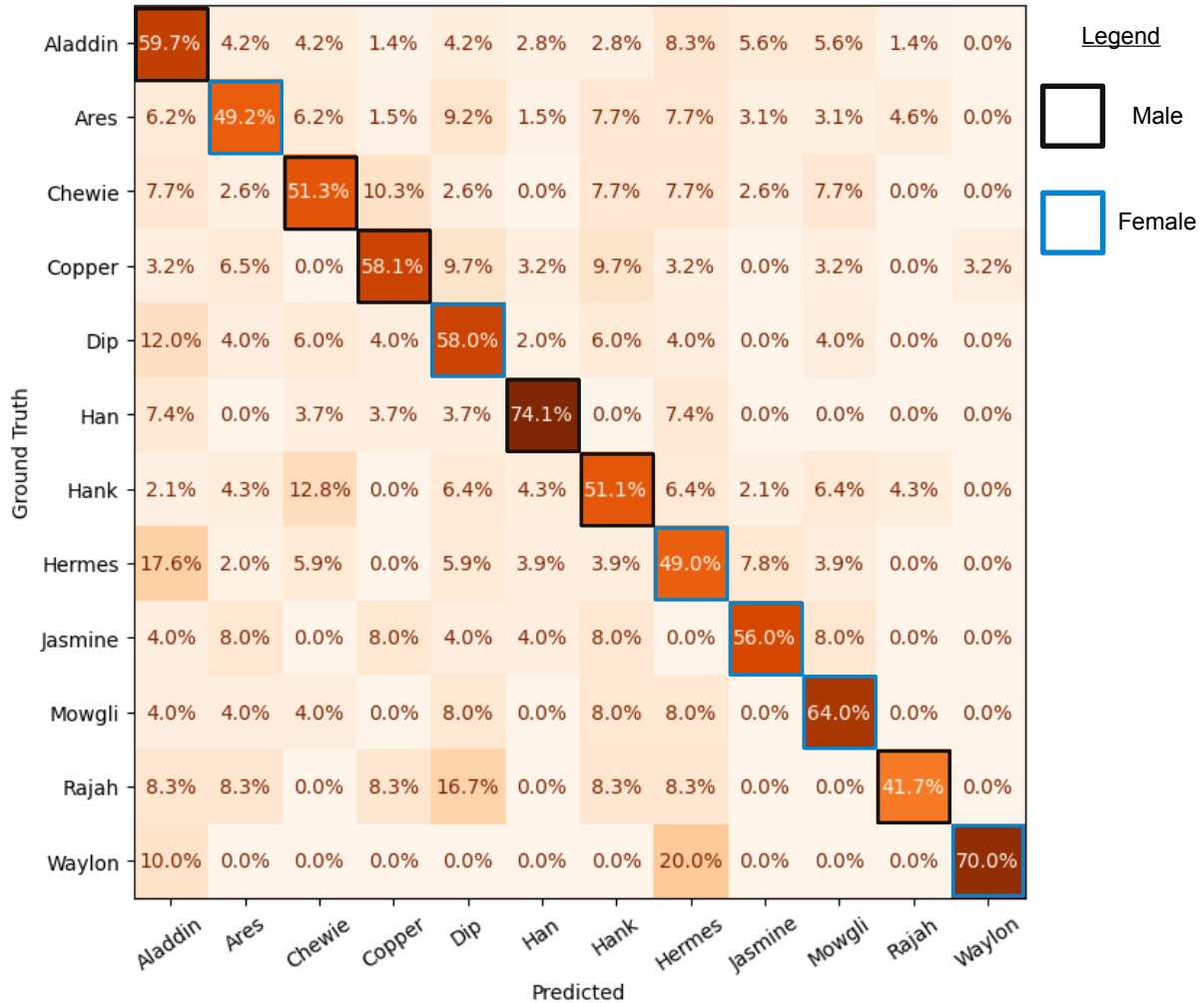


Figure 3.17. Multiple individuals classified by winner-take-all model. Confusion matrix reporting the winner-take-all predictions of the INM on twelve individuals shown to three observers over 34 recording sessions (testing accuracy=0.91, sensitivity=0.91, specificity=0.91, precision=0.88, negative predictive value=0.93, N_{trials} =454 match trials). The biological sex of the observed conspecifics is indicated by on the diagonal with blue indicating female and black indicating male. The following conspecifics were family members with a subject: Aladdin, Jasmine, Mowgli, Ares, Hermes. Percentages indicate true positive rates of the testing set of trials. All individuals decoded testing trials with a true positive rate at least $5\times$ random chance, as is indicated by the black dashed line in Figure 3.7D of the main text.

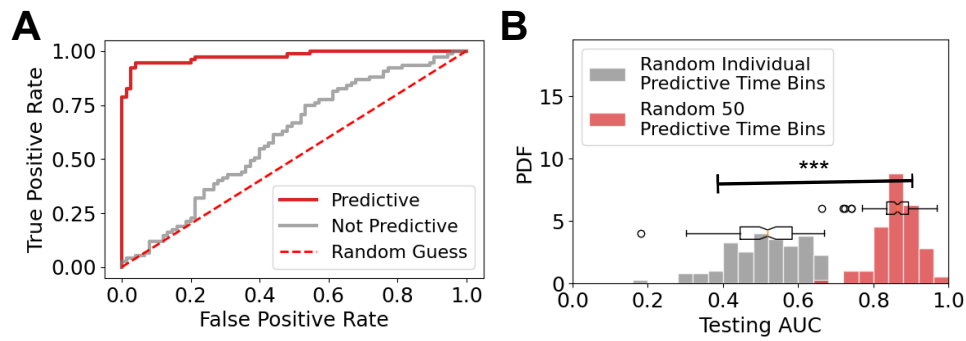


Figure 3.18. Decoding improved by melding multiple recording sessions. [a] ROC curves showing the MvMM decoding performance of (red) MvMM predictive time bins and (gray) randomly selected time bins. Indicated is (red dotted) random chance. Predictive time bins were selected from multiple recording sessions ($N_{sessions} = 14$). [b] Histograms of testing AUC values are shown for (gray) random individual predictive time bins and (red) 50 randomly selected predictive time bins, exhibiting a statistically significant difference of median value according to a Wilcoxon-Mann-Whitney test ($p < 0.001$, $N = 100$). Predictive time bins for the MvMM binary classification task were randomly considered from multiple recording sessions ($N_{sessions} = 14$).

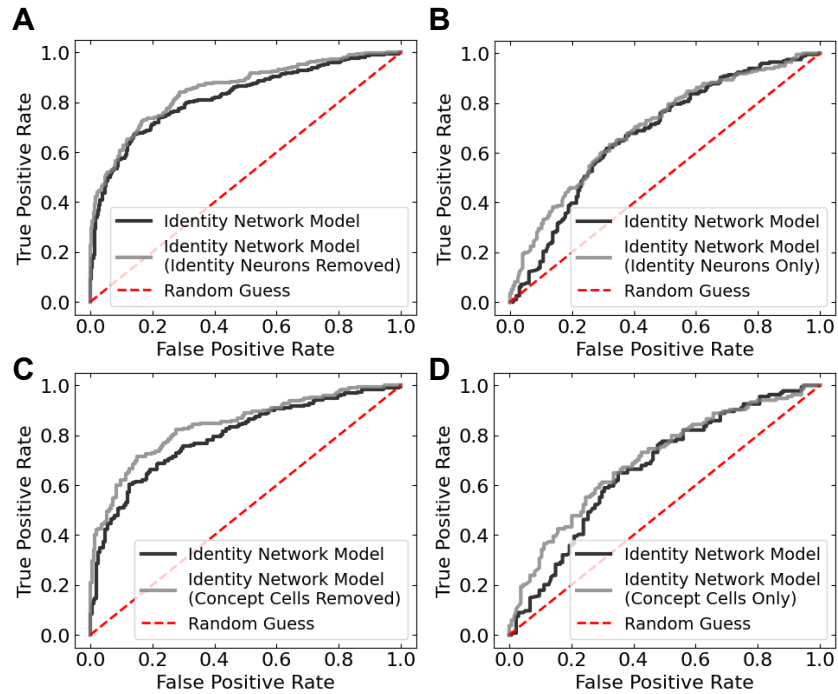


Figure 3.19. Decoding performance with and without identity selective neurons averaged over preferred individuals. [a] Shown are the ROC traces of the INM with all identity neurons removed (gray; AUC=0.850) and an equal number of random neurons removed from the remaining predictive population (black; AUC=0.820). [b] Shown are the ROC traces of the INM with only identity neurons considered (gray; AUC=0.700) and an equal number of neurons randomly selected from the remaining predictive population as control (black; AUC=0.677). Indicated is random chance (red dotted; AUC=0.500). [c] Shown are the ROC traces of the INM with all putative “concept cells” removed (gray; AUC=0.841) and an equal number of random neurons removed from the remaining predictive population (black; AUC=0.795). [d] Shown are the ROC traces of the INM with only putative “concept cells” considered (gray; AUC=0.700) and an equal number of neurons randomly selected from the remaining predictive population as control (black; AUC=0.666). Indicated is random chance (red dotted; AUC=0.500).

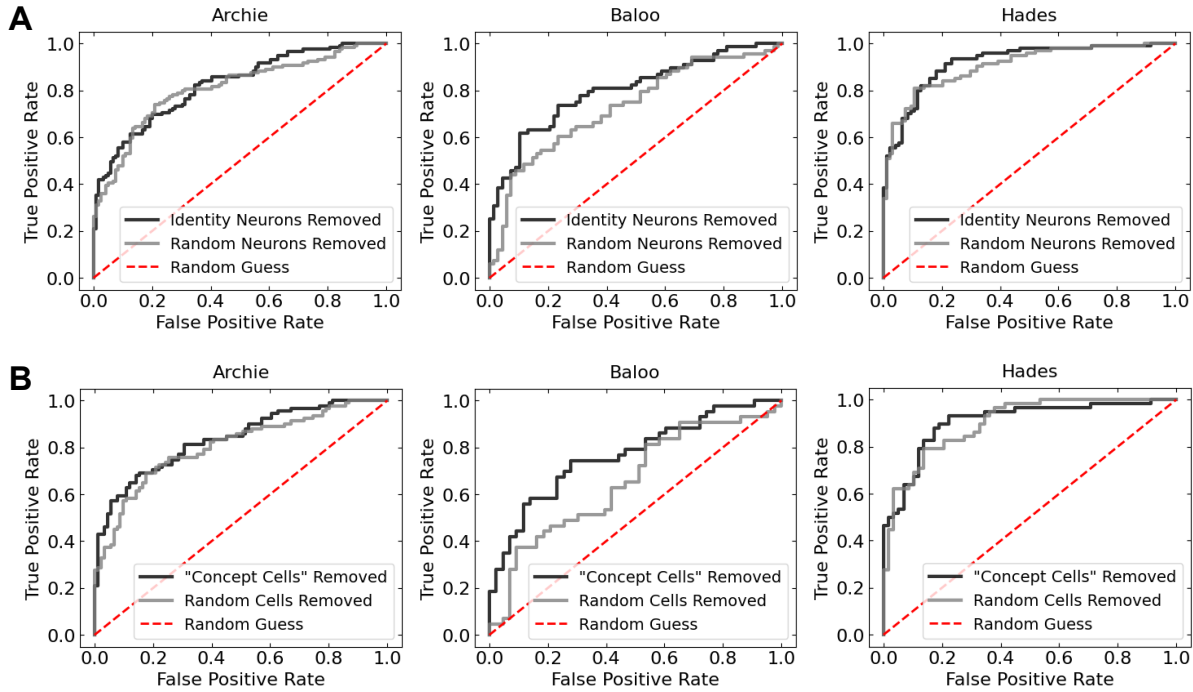


Figure 3.20. Identity network model for individual subjects. ROC curves were computed by averaging over all recording sessions for each of three observers: Archie (left, $N_{sessions} = 14$), Baloo (middle, $N_{sessions} = 12$), and Hades (right, $N_{sessions} = 8$). **[a]** ROC curves of our INM with only identity neurons (black) and an equal number of cells from the remaining predictive population (gray). Individual identities were averaged over if they were preferred by at least one identity neuron. **[b]** ROC curves demonstrating the predictive power of our INM with all “concept cells” removed (black) and an equal number of cells removed from the remaining predictive population (gray). Individual identities were averaged over if they were preferred by at least one “concept cell”. We controlled for network size by using the same number of features for both ROC curves in each panel. We did this for both the MvMM predictive population and the identity-specific predictive population in evaluating the INM.

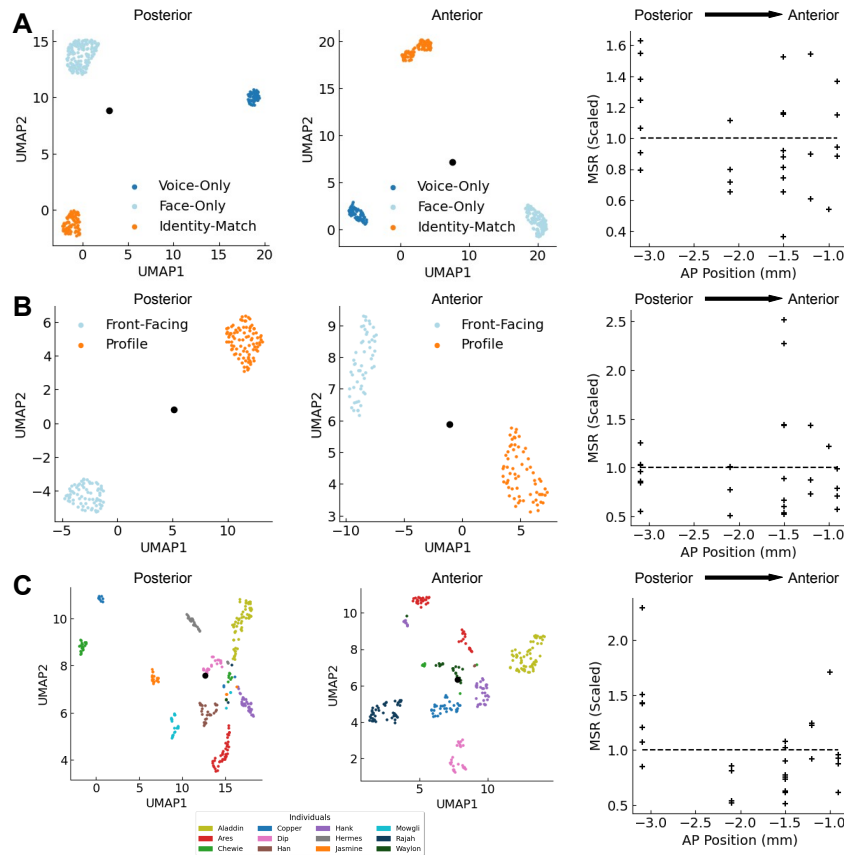


Figure 3.21. Separating stimulus categories at multiple probe locations. [a-c] Shown are manifold projections from a recording session conducted on (left) the most posterior and (middle) the most anterior probe location (anterior-posterior (AP) positions: -3.1mm, -0.9mm, respectively). (right) Shows AP positions versus mean-squared range (MSR) from (black dot in left,middle) the mean projected trial location. MSR was scaled across recording sessions to have a mean value of unity, as is shown by the black dashed line in the scatter plot to the right. One symbol represents one recording session in the scatter plot to the right. Indicated is the direction from posterior to anterior hippocampus. [a] Shown are stimulus categories of mode (dark blue) voice- only trials, (light blue) face-only trials, and (orange) identity-match trials. [b] Shown are face-only trials categorized by orientation as either (light blue) front-facing or (orange) profile. [c] Shown are unimodal and identity match trials categorized by identity as is indicated by the legend. Large MSR values suggest excellent separation at the indicated probe location. In the majority of recording sessions conducted on the most posterior electrode array (AP position: -3.1 mm), MSR was greater than the mean, suggesting excellent separability of identity in the most posterior probe location. Input features were mean firing rates averaged over the stimulus from $t=0$ to 3.5 seconds for each recorded neuron. The most posterior probe at -3.1 mm was implanted in Hades, who generated all recording sessions confirmed to be in CA1. Recording sessions were omitted if their AP position was not confirmed to be the same within a 95% confidence of no more than ± 0.1 mm, which resulted in 28 recording sessions being considered.

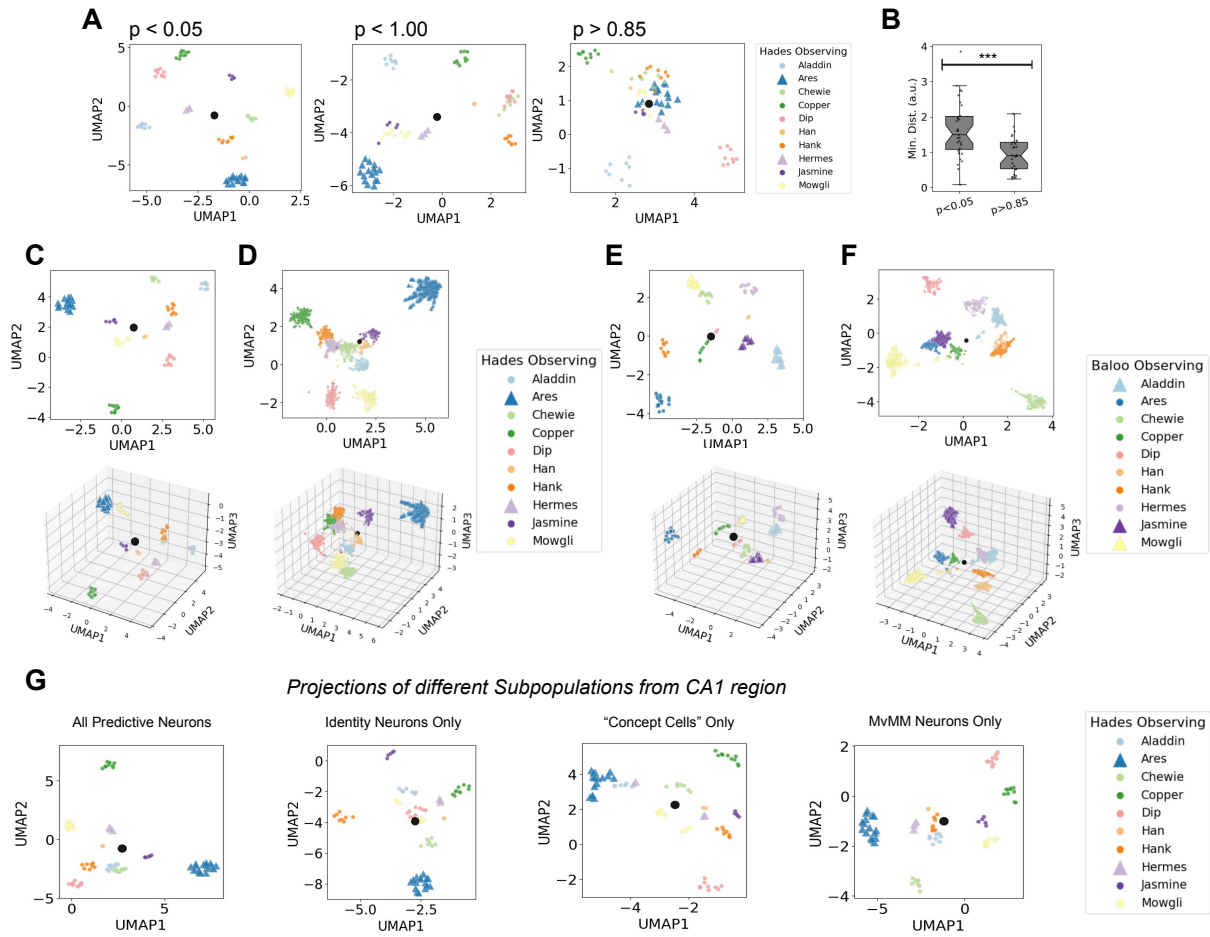


Figure 3.22. Low-dimensional projections of our rate code and event code. [a] Scatter plot showing an exemplar recording session as two-dimensional rate-coded representations of individual identity, where the firing rates were computed from all candidate time bins exhibiting (left) $p < 0.05$, (middle) $p < 1.00$, and (right) $p > 0.85$. [b] Box-and-whisker plots showing the minimum distance between any individual in our rate-coded representation of individual identity. The median minimum distance of (left) $p < 0.05$ was significantly smaller than the median minimum distance of (right) $p > 0.85$ according to a Wilcoxon-Mann-Whitney test ($p < 0.001$, $N_{sessions} = 29$). [c-f] Shown are the (top) first two axes and (bottom) first three axes of our representations of individual identity for two distinct observers: [c,d] Hades and [e,f] Baloo. [c,e] Shown are manifold projections of our predictive time bins and [d,f] our signed connection rate. Colors indicate individuals, and triangles indicate family members. The signed connection rate was evaluated no more than two seconds after stimulus onset, which was evaluated whenever the neuron with the largest overall spike count fired. [g] Rate-coded manifold projections comparing the same recording session restricted to four subpopulations of identity-specific predictive neurons. Subpopulations are shown (from left to right): all identity-specific predictive neurons, all identity neurons, all cross-modal invariant “concept cells”, and all MvMM neurons. Colors indicate individual identities listed in legends.

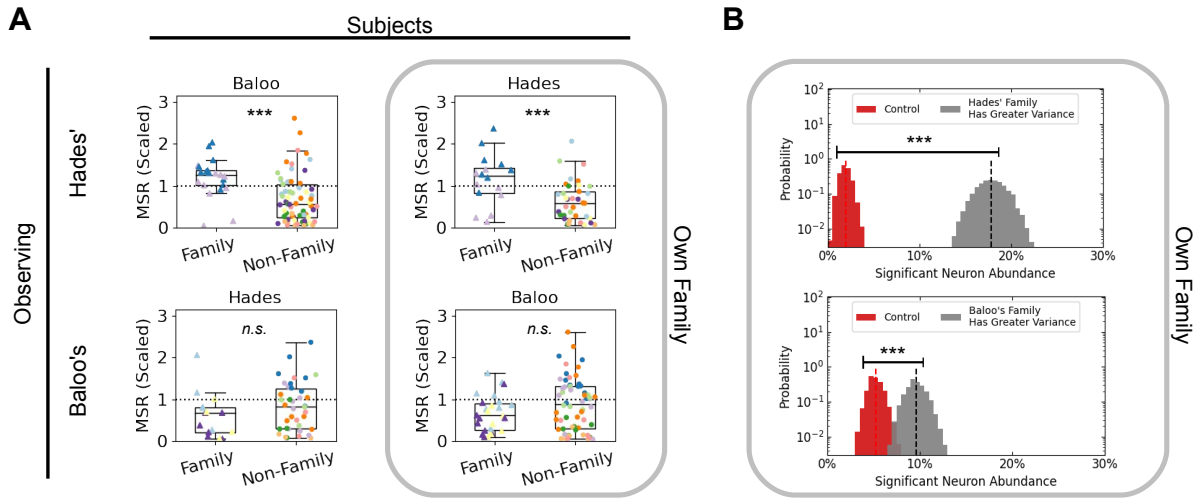


Figure 3.23. Separability of social categories. Significantly different values when subjects were observing the family of (top) Hades and (bottom) Baloo. **[a]** Shown are boxplots of MSR of subjects observing families of other subjects. Significance was computed according to a one-sided Student's t-test consistent with the other subjects viewing the same family, resulting in (top left, $N_{identities} \geq 20$) $p < 0.001$, (top right, $N_{identities} \geq 16$) $p < 0.001$, (bottom left, $N_{identities} \geq 14$) $p = 0.102$, and (bottom right, $N_{identities} \geq 26$) $p = 0.055$. Gray box indicates subjects were observing their own families. **[b]** Histograms showing the relative abundance of neurons with significantly larger variance of signed connection rate for the subject's own family relative to other conspecifics according to Fligner-Killeen's test ($p < 0.01$). Variance of signed connection rate was computed from the reference neuron to each neuron. Control was a random shuffle of the labels for each neuron. Distributions were determined via bootstrap. Dotted lines indicate the mean values for Hades viewing her own family (left, $18 \pm 3\%$ out of $N = 610$) and Baloo viewing her own family (right, $10 \pm 2\%$ out of $N = 822$), which both exhibited significantly more significant neurons than control (left, $2.0 \pm 1.1\%$ out of $N = 610$; right, $5.2 \pm 1.5\%$ out of $N = 822$) according to Student's t-test ($p < 0.001$, $N_{bootstrap} = 10,000$). Uncertainty indicates 95% confidence intervals of the mean. Gray box indicates subjects were observing their own families. Bin width is 0.5%.

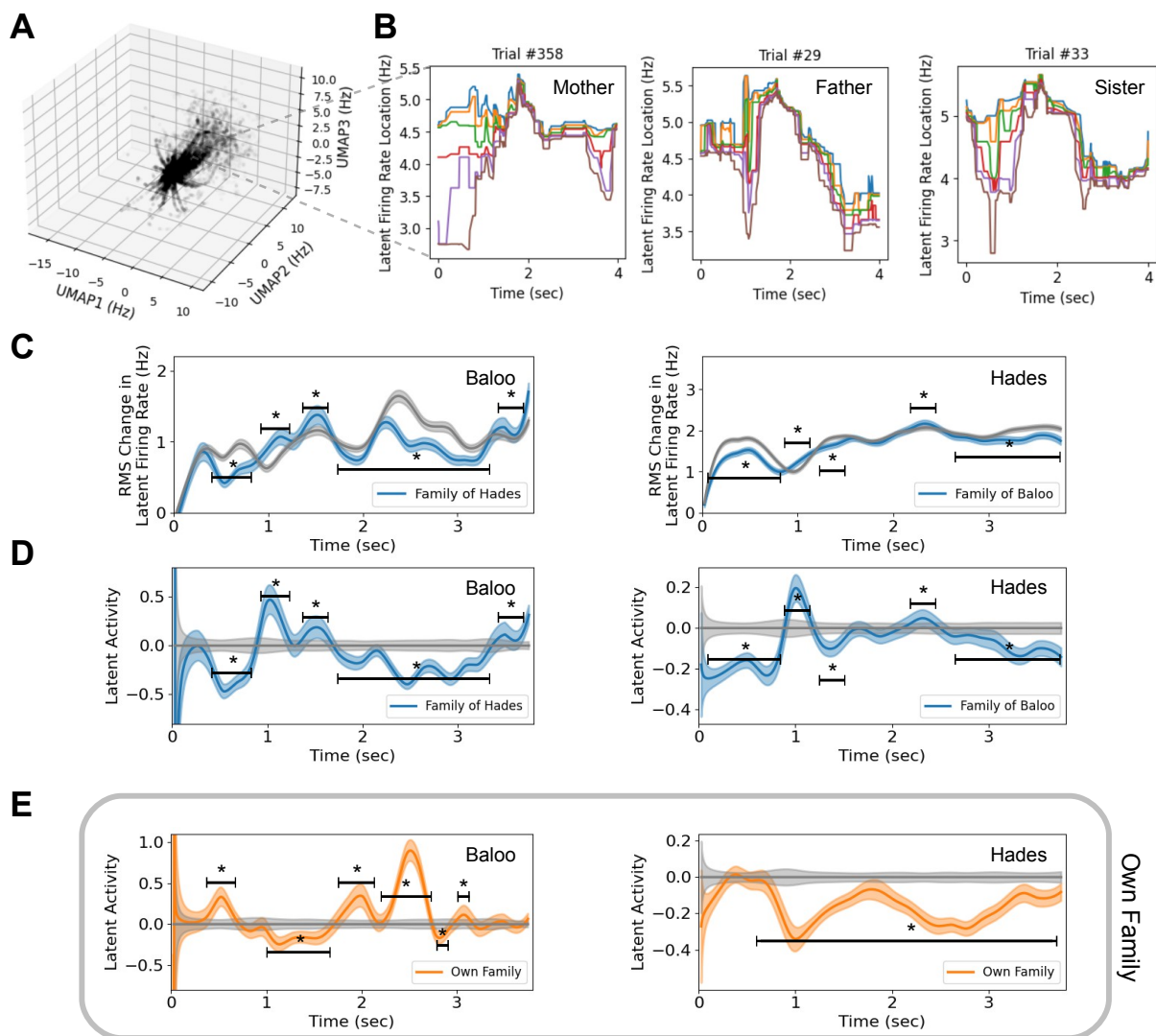


Figure 3.24. Quantification of latent activity. [a] Shown are the first three axes of the six dimensional latent firing rate, which was an unsupervised manifold projection of the absolute value of the signed connection rate from the same neuron with the largest overall spike count (i.e. the reference neuron) to all neurons that appeared approximately symmetric (defined in Methods). [b] Shown are time traces of our latent firing rate for an exemplary trial from each of three family members of Baloo. Each color represents one dimension. The order of dimensions is consistent between panels. [c] Root mean squared (RMS) change in latent firing rate versus time averaged over all recording sessions from subjects (left) Baloo and (right) Hades. Traces average over identity-match trials showing (blue) the family members of the subject and (gray) all conspecifics. [d] Latent activity versus time for (left) Baloo and (right) Hades. Latent activity traces were computed as the ratio of the RMS change in latent firing rate to control minus one. Control was RMS change in latent firing rate averaged over all identity-match trials. [e] Latent activity versus time for (left) Baloo and (right) Hades viewing their own family. Control was as in [d].

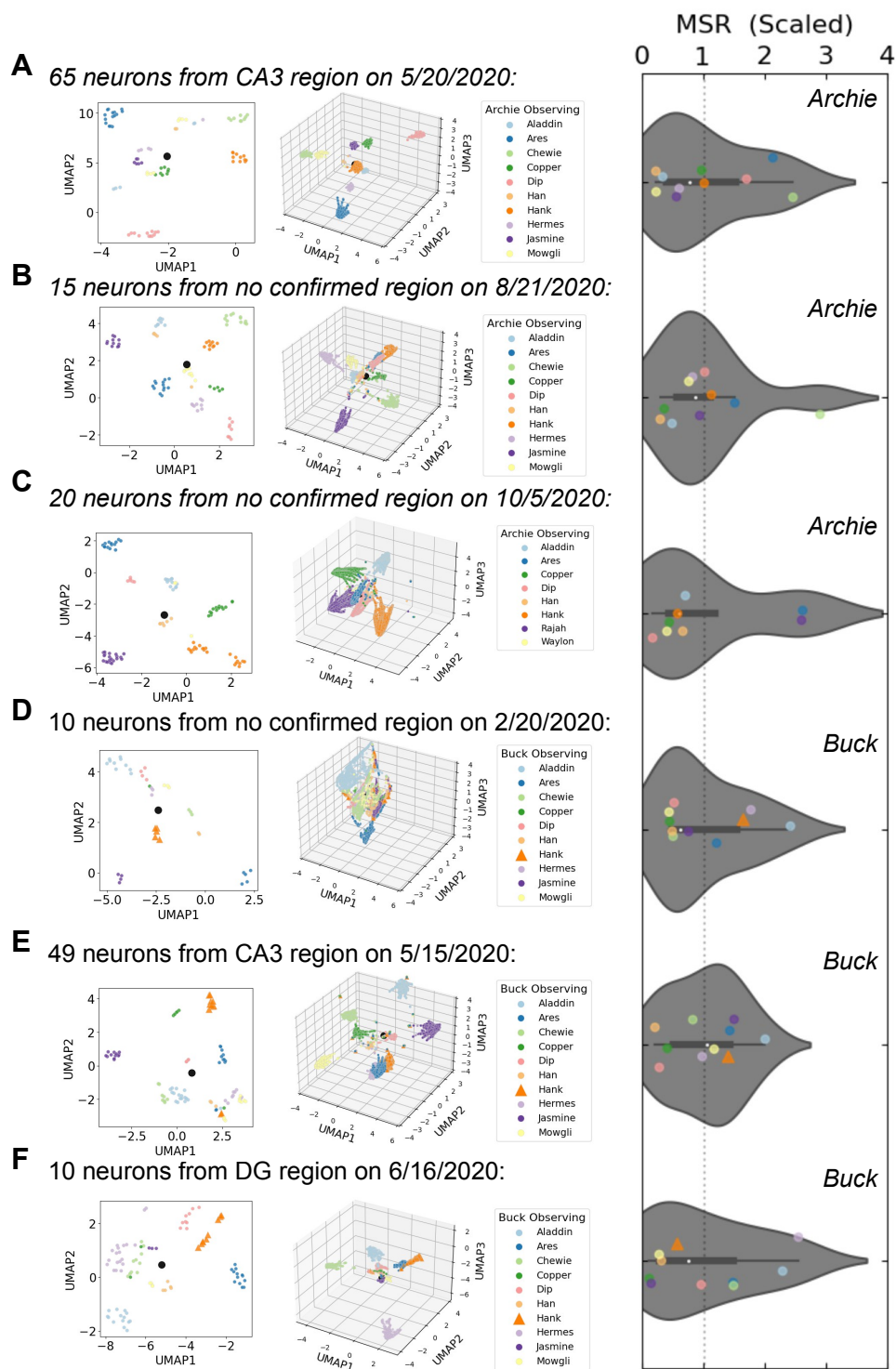


Figure 3.25. Stability of manifold projections. [a-f] Manifold projections comparing three different recording sessions conducted on different observers, Archie [a-c] and Buck [d-f]. Shown are rate-coded projections (left), event-coded projections (middle), and MSR computed from the event-coded projections (right). Colors indicate individual identities listed in legends.

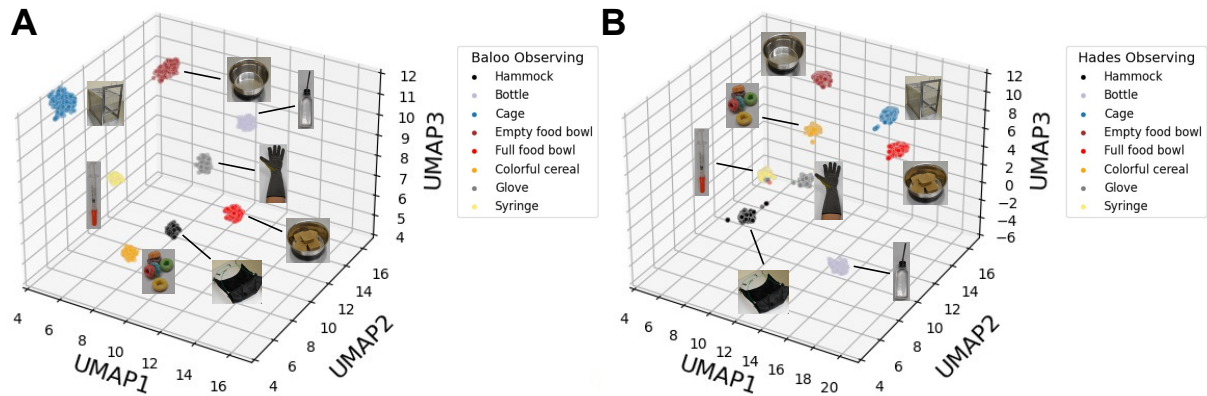


Figure 3.26. Separability of socially-agnostic categories. [a-b] Event-coded representations of inanimate objects from the laboratory setting. Separation of socially-agnostic categories are shown in marmoset hippocampus for two subjects, [a] Baloo and [b] Hades. Visual images from each of these object categories was presented to subjects using the same stimulus presentation protocol as for the unimodal stimuli while recording single neuron activity in marmoset hippocampus from two marmosets. Likewise, we performed the same signed-connection rate analysis and input those data into UMAP using the same data analysis pipeline as described for analyses presented in Figure 3.8.

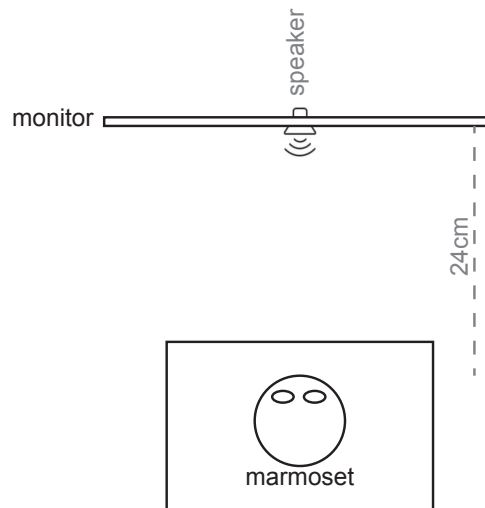


Figure 3.27. Schematic drawing of experimental setup. In an anechoic chamber, marmoset subjects were seated, positioned 24 centimeters away from a monitor and a speaker. The speaker was located just below the monitor.

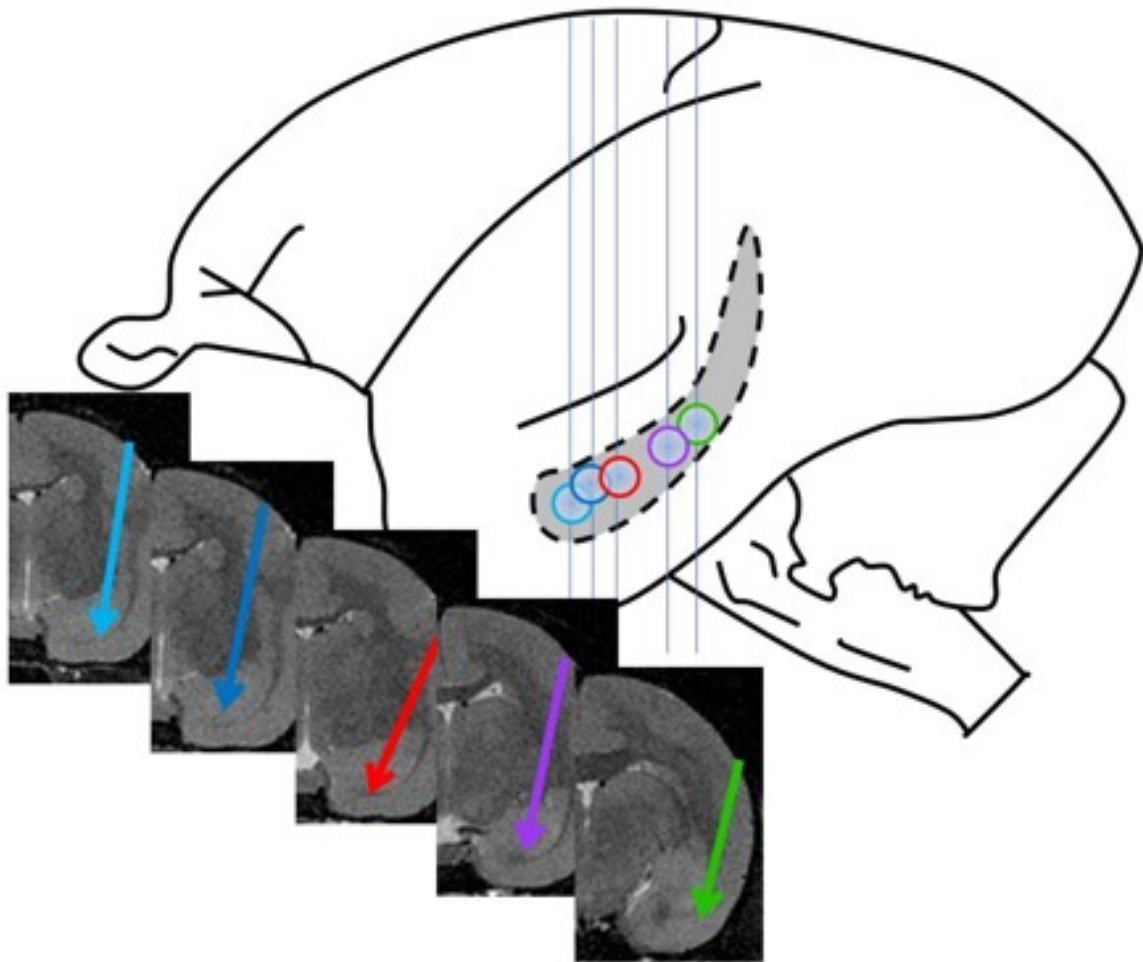


Figure 3.28. Anatomical locations of microwire bundles across animals. Arrows on MRI cross-sections indicate trajectory of each microwire brush array in marmoset hippocampus. Each color indicates a different animal's array. Circles correspond to anterior-posterior position.

Bibliography

- [1] Henry DI Abarbanel, Reggie Brown, and MB Kennel. Lyapunov exponents in chaotic systems: their importance and their evaluation using observed data. *International Journal of Modern Physics B*, 5(09):1347–1375, 1991.
- [2] Ikuma Adachi and Robert R Hampton. Rhesus monkeys see who they hear: spontaneous cross-modal memory for familiar conspecifics. *PLoS One*, 6(8):e23345, 2011.
- [3] Ikuma Adachi, Hiroko Kuwahata, and Kazuo Fujita. Dogs recall their owner’s face upon hearing the owner’s voice. *Animal cognition*, 10:17–21, 2007.
- [4] Philippe V Afonso, Mirkka Janka-Junttila, Young Jong Lee, Colin P McCann, Charlotte M Oliver, Khaled A Aamer, Wolfgang Losert, Marcus T Cicerone, and Carole A Parent. LTB4 is a signal-relay molecule during neutrophil chemotaxis. *Developmental cell*, 22(5):1079–1091, 2012.
- [5] Maria L Allende, Jennifer L Dreier, Suzanne Mandala, and Richard L Proia. Expression of the sphingosine 1-phosphate receptor, s1p1, on t-cells controls thymic emigration. *Journal of Biological Chemistry*, 279(15):15396–15401, 2004.
- [6] Ana F Almeida-Santos, Vinícius R Carvalho, Laura F Jaimes, Caio M de Castro, Hyorrana P Pinto, Tadeu PD Oliveira, Luciene B Vieira, Márcio FD Moraes, and Grace S Pereira. Social isolation impairs the persistence of social recognition memory by disturbing the glutamatergic tonus and the olfactory bulb-dorsal hippocampus coupling. *Scientific reports*, 9(1):473, 2019.
- [7] Jocelyne Bachevalier. Nonhuman primate models of hippocampal development and dysfunction. *Proceedings of the National Academy of Sciences*, 116(52):26210–26216, 2019.
- [8] Sonya Bader, Arjan Kortholt, and Peter JM Van Haastert. Seven Dictyostelium discoideum phosphodiesterases degrade three pools of cAMP and cGMP. *Biochemical Journal*, 402(1):153–161, 2007.
- [9] Deenadayalan Bakthavatsalam, Debra A Brock, N Neda Nikravan, Kevin D Houston, R Diane Hatton, and Richard H Gomer. The secreted Dictyostelium protein CfaD is a chalone. *Journal of cell science*, 121(15):2473–2480, 2008.

- [10] Pierre Baraduc, J-R Duhamel, and Sylvia Wirth. Schema cells in the macaque hippocampus. *Science*, 363(6427):635–639, 2019.
- [11] Clemens Bechinger, Roberto Di Leonardo, Hartmut Löwen, Charles Reichhardt, Giorgio Volpe, and Giovanni Volpe. Active particles in complex and crowded environments. *Reviews of Modern Physics*, 88(4):045006, 2016.
- [12] Pascal Belin, Clémentine Bodin, and Virginia Aglieri. A “voice patch” system in the primate brain for processing vocal information? *Hearing research*, 366:65–74, 2018.
- [13] Archana Belle, Amos Tanay, Ledion Bitincka, Ron Shamir, and Erin K O’Shea. Quantification of protein half-lives in the budding yeast proteome. *Proceedings of the National Academy of Sciences*, 103(35):13004–13009, 2006.
- [14] Juan Carlos Izpisua Belmonte, Edward M Callaway, Sarah J Caddick, Patricia Churchland, Guoping Feng, Gregg E Homanics, Kuo-Fen Lee, David A Leopold, Cory T Miller, Jude F Mitchell, et al. Brains, genes, and primates. *Neuron*, 86(3):617–631, 2015.
- [15] Daniel Bendor and Xiaoqin Wang. The neuronal representation of pitch in primate auditory cortex. *Nature*, 436(7054):1161–1165, 2005.
- [16] Sandy Bensoussan, Raphaëlle Tigeot, Alban Lemasson, Marie-Christine Meunier-Salaün, and Céline Tallet. Domestic piglets (*sus scrofa domestica*) are attentive to human voice and able to discriminate some prosodic features. *Applied Animal Behaviour Science*, 210:38–45, 2019.
- [17] Lorenzo Bertini and Nicoletta Cancrini. The stochastic heat equation: Feynman-kac formula and intermittence. *Journal of statistical Physics*, 78(5):1377–1401, 1995.
- [18] Carsten Beta, Alexander S Mikhailov, Harm H Rotermund, and Gerhard Ertl. Defect-mediated turbulence in a catalytic surface reaction. *EPL (Europhysics Letters)*, 75(6):868, 2006.
- [19] Brian O Bingen, Marc C Engels, Martin J Schaliij, Wanchana Jangsangthong, Zeinab Neshati, Iolanda Feola, Dirk L Ypey, Saïd FA Askar, Alexander V Panfilov, Daniël A Pijnappels, et al. Light-induced termination of spiral wave arrhythmias by optogenetic engineering of atrial cardiomyocytes. *Cardiovascular research*, 104(1):194–205, 2014.
- [20] Denis Boyer, William Mather, Octavio Mondragón-Palomino, Sirio Orozco-Fuentes, Tal Danino, Jeff Hasty, and Lev S Tsimring. Buckling instability in ordered bacterial colonies. *Physical biology*, 8(2):026008, 2011.
- [21] Debra A Brock and Richard H Gomer. A cell-counting factor regulating structure size in *Dictyostelium*. *Genes & development*, 13(15):1960–1969, 1999.
- [22] Debra A Brock and Richard H Gomer. A secreted factor represses cell proliferation in *Dictyostelium*. *Development*, 132(20):4553–4562, 2005.

- [23] Debra A Brock, R Diane Hatton, Dan-Victor Giurgiutiu, Brenton Scott, Wonhee Jang, Robin Ammann, and Richard H Gomer. CF45-1, a secreted protein which participates in Dictyostelium group size regulation. *Eukaryotic cell*, 2(4):788–797, 2003.
- [24] Debra A Brock, Wouter N Van Egmond, Yousif Shamoo, R Diane Hatton, and Richard H Gomer. A 60-kilodalton protein component of the counting factor complex regulates group size in Dictyostelium discoideum. *Eukaryotic cell*, 5(9):1532–1538, 2006.
- [25] THOMAS BUGNYAR and LUDWIG HUBER. Push or pull: an experimental study on imitation in marmosets. *Animal Behaviour*, 54(4):817–831, 1997.
- [26] Judith M Burkart, Andrea Strasser, and Maria Foglia. Trade-offs between social learning and individual innovativeness in common marmosets, callithrix jacchus. *Animal Behaviour*, 77(5):1291–1301, 2009.
- [27] David J Callans, Edward P Gerstenfeld, Sanjay Dixit, Erica Zado, Mark Vanderhoff, JIAN-FANG REN, and Francis E Marchlinski. Efficacy of repeat pulmonary vein isolation procedures in patients with recurrent atrial fibrillation. *Journal of cardiovascular electrophysiology*, 15(9):1050–1055, 2004.
- [28] Yuansheng Cao, Elisabeth Ghabache, Yuchuan Miao, Cassandra Niman, Hiroyuki Hakozaki, Samara L Reck-Peterson, Peter N Devreotes, and Wouter-Jan Rappel. A minimal computational model for three-dimensional cell migration. *Journal of the Royal Society Interface*, 16(161):20190619, 2019.
- [29] WJ Carr, Lily Yee, Diane Gable, and Elizabeth Marasco. Olfactory recognition of conspecifics by domestic norway rats. *Journal of Comparative and Physiological Psychology*, 90(9):821, 1976.
- [30] Stephen B Carter. Haptotaxis and the mechanism of cell motility. *Nature*, 213(5073):256–260, 1967.
- [31] Martin Casdagli. Nonlinear prediction of chaotic time series. *Physica D: Nonlinear Phenomena*, 35(3):335–356, 1989.
- [32] Christine L Chaffer and Robert A Weinberg. A perspective on cancer cell metastasis. *science*, 331(6024):1559–1564, 2011.
- [33] Le Chang and Doris Y Tsao. The code for facial identity in the primate brain. *Cell*, 169(6):1013–1028, 2017.
- [34] Tristan A Chaplin, Hsin-Hao Yu, Juliana GM Soares, Ricardo Gattass, and Marcello GP Rosa. A conserved pattern of differential expansion of cortical areas in simian primates. *Journal of Neuroscience*, 33(38):15120–15125, 2013.
- [35] T Chen and C Guestrin. Proc. 22nd acm sigkdd int. conf. knowl. discovery data min, 2016.

- [36] Rex L Chisholm and Richard A Firtel. Insights into morphogenesis from a simple developmental system. *Nature reviews Molecular cell biology*, 5(7):531–541, 2004.
- [37] Rex L Chisholm, Susan Hopkinson, and Harvey F Lodish. Superinduction of the dictyostelium discoideum cell surface camp receptor by pulses of camp. *Proceedings of the National Academy of Sciences*, 84(4):1030–1034, 1987.
- [38] Hyo Won Choi, Jose A Navia, and Ghassan S Kassab. Stroke propensity is increased under atrial fibrillation hemodynamics: a simulation study. *PloS one*, 8(9):e73485, 2013.
- [39] Sumeet S Chugh, Rasmus Havmoeller, Kumar Narayanan, David Singh, Michiel Rienstra, Emelia J Benjamin, Richard F Gillum, Young-Hoon Kim, John H McAnulty Jr, Zhi-Jie Zheng, et al. Worldwide epidemiology of atrial fibrillation: a global burden of disease 2010 study. *Circulation*, 129(8):837–847, 2014.
- [40] R. Clark. *The molecular and cellular biology of wound repair*. Plenum, New York, 1996.
- [41] RH Clayton, Olivier Bernus, EM Cherry, Hans Dierckx, Flavio H Fenton, Lucia Mirabella, Alexander V Panfilov, Frank B Sachse, Gunnar Seemann, and H Zhang. Models of cardiac tissue electrophysiology: progress, challenges and open questions. *Progress in biophysics and molecular biology*, 104(1-3):22–48, 2011.
- [42] J. Condeelis, R. H. Singer, and J. E. Segall. The great escape: When cancer cells hijack the genes for chemotaxis and motility. *Annu Rev Cell Dev Biol*, 21:695–718, 2005.
- [43] Katherine Copenhagen, Ricard Alert, Ned S Wingreen, and Joshua W Shaevitz. Topological defects promote layer formation in myxococcus xanthus colonies. *Nature Physics*, 17(2):211–215, 2021.
- [44] P Couillet, L Gil, and J Lega. Defect-mediated turbulence. *Physical Review Letters*, 62(14):1619, 1989.
- [45] Marjorie Coulon, Bertrand L Deputte, Yvan Heyman, and Claude Baudoin. Individual recognition in domestic cattle (bos taurus): evidence from 2d-images of heads from different breeds. *PLoS One*, 4(2):e4441, 2009.
- [46] Hristos S Courellis, Samuel U Nummela, Michael Metke, Geoffrey W Diehl, Robert Bussell, Gert Cauwenberghs, and Cory T Miller. Spatial encoding in primate hippocampus during free navigation. *PLoS biology*, 17(12):e3000546, 2019.
- [47] JH Crook and JS Gartlan. Evolution of primate societies. *Foundations of Tropical Forest Biology: Classic Papers with Commentaries*, 210:457, 2002.
- [48] John C Dallon and Hans G Othmer. A discrete cell model with adaptive signalling for aggregation of Dictyostelium discoideum. *Philosophical Transactions of the Royal Society of London. Series B: Biological Sciences*, 352(1351):391–417, 1997.

- [49] Karen E Daniels and Eberhard Bodenschatz. Defect turbulence in inclined layer convection. *Physical Review Letters*, 88(3):034501, 2002.
- [50] Dhani Dharmaprani, Madeline Schopp, Pawel Kuklik, Darius Chapman, Anandaroop Lahiri, Lukah Dykes, Feng Xiong, Martin Aguilar, Benjamin Strauss, Lewis Mitchell, et al. Renewal theory as a universal quantitative framework to characterize phase singularity regeneration in mammalian cardiac fibrillation. *Circulation: Arrhythmia and Electrophysiology*, 12(12):e007569, 2019.
- [51] Leslie J Digby and Claudio E Barreto. Social organization in a wild population of callithrix jacchus. *Folia primatologica*, 61(3):123–134, 1993.
- [52] Erika Donà, Joseph D Barry, Guillaume Valentin, Charlotte Quirin, Anton Khmelinskii, Andreas Kunze, Sevi Durdu, Lionel R Newton, Ana Fernandez-Minan, Wolfgang Huber, et al. Directional tissue migration through a self-generated chemokine gradient. *Nature*, 503(7475):285–289, 2013.
- [53] Amin Doostmohammadi, Jordi Ignés-Mullol, Julia M Yeomans, and Francesc Sagués. Active nematics. *Nature communications*, 9(1):1–13, 2018.
- [54] Sandra Döpjan, Armin Tuchscherer, Jan Langbein, Peter-Christian Schön, Gerhard Mantuffel, and Birger Puppe. Behavioural and cardiac responses towards conspecific distress calls in domestic pigs (*sus scrofa*). *Physiology & behavior*, 103(5):445–452, 2011.
- [55] Martin Dworkin and Kenneth H Keller. Solubility and diffusion coefficient of adenosine 3': 5'-monophosphate. *Journal of Biological Chemistry*, 252(3):864–865, 1977.
- [56] Blas Echebarria and Alain Karma. Instability and spatiotemporal dynamics of alternans in paced cardiac tissue. *Physical review letters*, 88(20):208101, 2002.
- [57] Robert E Ecke, Yuchou Hu, Ronnie Mainieri, and Guenter Ahlers. Excitation of spirals and chiral symmetry breaking in rayleigh-bénard convection. *Science*, 269(5231):1704–1707, 1995.
- [58] J-P Eckmann, S Oliffson Kamphorst, David Ruelle, and S Ciliberto. Liapunov exponents from time series. *Physical Review A*, 34(6):4971, 1986.
- [59] David A Egolf, Ilarion V Melnikov, Werner Pesch, and Robert E Ecke. Mechanisms of extensive spatiotemporal chaos in rayleigh-bénard convection. *Nature*, 404(6779):733–736, 2000.
- [60] Irving R Epstein and Kenneth Showalter. Nonlinear chemical dynamics: oscillations, patterns, and chaos. *The Journal of Physical Chemistry*, 100(31):13132–13147, 1996.
- [61] M Faure, J Franke, AL Hall, GJ Podgorski, and RH Kessin. The cyclic nucleotide phosphodiesterase gene of *Dictyostelium discoideum* contains three promoters specific for growth, aggregation, and late development. *Molecular and cellular biology*, 10(5):1921–1930, 1990.

- [62] Bryan A Félix. *Mathematical Modeling of Cell Migration: Mechanisms in Dictyostelium discoideum*. PhD thesis, University of Minnesota, 2023.
- [63] F. Fenton and A. Karma. Vortex dynamics in three-dimensional continuous myocardium with fiber rotation: Filament instability and fibrillation. *Chaos*, 8:20–47, 1998.
- [64] Flavio H Fenton, Elizabeth M Cherry, Alain Karma, and Wouter-Jan Rappel. Modeling wave propagation in realistic heart geometries using the phase-field method. *Chaos: An Interdisciplinary Journal of Nonlinear Science*, 15(1):013502, 2005.
- [65] Jennifer N Ferguson, Larry J Young, Elizabeth F Hearn, Martin M Matzuk, Thomas R Insel, and James T Winslow. Social amnesia in mice lacking the oxytocin gene. *Nature genetics*, 25(3):284–288, 2000.
- [66] Linnea C Franssen, Tommaso Lorenzi, Andrew EF Burgess, and Mark AJ Chaplain. A mathematical framework for modelling the metastatic spread of cancer. *Bulletin of mathematical biology*, 81:1965–2010, 2019.
- [67] Winrich A Freiwald. Social interaction networks in the primate brain. *Current opinion in neurobiology*, 65:49–58, 2020.
- [68] Winrich A Freiwald and Doris Y Tsao. Functional compartmentalization and viewpoint generalization within the macaque face-processing system. *Science*, 330(6005):845–851, 2010.
- [69] Kerstin A Fritsches and Marcello GP Rosa. Visuotopic organisation of striate cortex in the marmoset monkey (callithrix jacchus). *Journal of Comparative Neurology*, 372(2):264–282, 1996.
- [70] Danny Fuller, Wen Chen, Micha Adler, Alex Groisman, Herbert Levine, Wouter-Jan Rappel, and William F. Loomis. External and internal constraints on eukaryotic chemotaxis. *Proceedings of the National Academy of Sciences*, 107(21):9656–9659, 2010.
- [71] Bruce Furie and Barbara C Furie. Molecular and cellular biology of blood coagulation. *New England Journal of Medicine*, 326(12):800–806, 1992.
- [72] Marianne Fyhn, Sturla Molden, Stig Hollup, May-Britt Moser, and Edvard I Moser. Hippocampal neurons responding to first-time dislocation of a target object. *Neuron*, 35(3):555–566, 2002.
- [73] C. Gardiner. *Stochastic Methods: A Handbook for the Natural and Social Sciences*. Springer-Verlag, Berlin Heidelberg, 2009.
- [74] Alan Garfinkel, Peng-Sheng Chen, Donald O Walter, Hrayr S Karagueuzian, Boris Kogan, Steven J Evans, Mikhail Karpoukhin, Chun Hwang, Takumi Uchida, Masamichi Gotoh, et al. Quasiperiodicity and chaos in cardiac fibrillation. *The Journal of clinical investigation*, 99(2):305–314, 1997.

- [75] G Gerisch, D Malchow, V Riedel, E Müller, and M Every. Cyclic AMP phosphodiesterase and its inhibitor in slime mould development. *Nature New Biology*, 235(55):90–92, 1972.
- [76] G Gerisch and U Wick. Intracellular oscillations and release of cyclic AMP from *Dictyostelium* cells. *Biochemical and biophysical research communications*, 65(1):364–370, 1975.
- [77] Edward P Gerstenfeld, Peter Guerra, Paul B Sparks, Kyoko Hattori, and Michael D Lesh. Clinical outcome after radiofrequency catheter ablation of focal atrial fibrillation triggers. *Journal of Cardiovascular Electrophysiology*, 12(8):900–908, 2001.
- [78] Alan R Gingle. Critical density for relaying in *Dictyostelium discoideum* and its relation to phosphodiesterase secretion into the extracellular medium. *Journal of cell science*, 20(1):1–20, 1976.
- [79] Katalin M Gothard, Francesco P Battaglia, Cynthia A Erickson, Kevin M Spitler, and David G Amaral. Neural responses to facial expression and face identity in the monkey amygdala. *Journal of neurophysiology*, 97(2):1671–1683, 2007.
- [80] Katalin M Gothard, Kelly N Brooks, and Mary A Peterson. Multiple perceptual strategies used by macaque monkeys for face recognition. *Animal cognition*, 12:155–167, 2009.
- [81] Thomas Gregor, Koichi Fujimoto, Noritaka Masaki, and Satoshi Sawai. The onset of collective behavior in social amoebae. *Science*, 328(5981):1021–1025, 2010.
- [82] Pau Guillamat, Jordi Ignés-Mullol, and Francesc Sagués. Control of active liquid crystals with a magnetic field. *Proceedings of the National Academy of Sciences*, 113(20):5498–5502, 2016.
- [83] Michel Haissaguerre, Laurent Gencel, Bruno Fischer, Philippe Le Metayer, Franck Poquet, Frank I Marcus, and Jacques Clementy. Successful catheter ablation of atrial fibrillation. *Journal of cardiovascular electrophysiology*, 5(12):1045–1052, 1994.
- [84] Michel Haissaguerre, Pierre Jaïs, Dipen C Shah, Atsushi Takahashi, Mélèze Hocini, Gilles Quiniou, Stéphane Garrigue, Alain Le Mouroux, Philippe Le Métayer, and Jacques Clémenty. Spontaneous initiation of atrial fibrillation by ectopic beats originating in the pulmonary veins. *New England Journal of Medicine*, 339(10):659–666, 1998.
- [85] Hidenori Hashimura, Yusuke V Morimoto, Masato Yasui, and Masahiro Ueda. Collective cell migration of *Dictyostelium* without cAMP oscillations at multicellular stages. *Communications biology*, 2(1):34, 2019.
- [86] Simon Haykin and Xiao Bo Li. Detection of signals in chaos. *Proceedings of the IEEE*, 83(1):95–122, 1995.
- [87] Janis K Hesse and Doris Y Tsao. The macaque face patch system: a turtle’s underbelly for the brain. *Nature Reviews Neuroscience*, 21(12):695–716, 2020.

- [88] M Hildebrand, M Bär, and M Eiswirth. Statistics of topological defects and spatiotemporal chaos in a reaction-diffusion system. *Physical Review Letters*, 75(8):1503, 1995.
- [89] Heribert Hofer and Marion L East. The commuting system of serengeti spotted hyaenas: how a predator copes with migratory prey. i. social organization. *Animal Behaviour*, 46(3):547–557, 1993.
- [90] Thomas Höfer, Jonathan A Sherratt, and Philip Kumar Maini. Dictyostelium discoideum: cellular self-organization in an excitable biological medium. *Proceedings of the Royal Society of London. Series B: Biological Sciences*, 259(1356):249–257, 1995.
- [91] Takashi Hotta, Shun Satoh, Naoya Kosaka, and Masanori Kohda. Face recognition in the tanganyikan cichlid julidochromis transcriptus. *Animal Behaviour*, 127:1–5, 2017.
- [92] Anna Huttenlocher and Mark C Poznansky. Reverse leukocyte migration can be attractive or repulsive. *Trends in cell biology*, 18(6):298–306, 2008.
- [93] José Jalife. Ventricular fibrillation: mechanisms of initiation and maintenance. *Annual review of physiology*, 62(1):25–50, 2000.
- [94] Kieran D James, William E Jenkinson, and Graham Anderson. T-cell egress from the thymus: Should i stay or should i go? *Journal of leukocyte biology*, 104(2):275–284, 2018.
- [95] Amelia H Janeczek, WAYNE A Marasco, PIERSON J van Alten, and ROBERT J Walter. Autoradiographic analysis of formylpeptide chemoattractant binding, uptake and intracellular processing by neutrophils. *Journal of Cell Science*, 94(1):155–168, 1989.
- [96] Samantha Jones, Oliver Burman, and Michael Mendl. Social discrimination of cage-mates and non-cage-mates by rats. *Behavioural processes*, 106:130–140, 2014.
- [97] Michael J Jutras and Elizabeth A Buffalo. Recognition memory signals in the macaque hippocampus. *Proceedings of the National Academy of Sciences*, 107(1):401–406, 2010.
- [98] Mark Kac. On distributions of certain wiener functionals. *Transactions of the American Mathematical Society*, 65(1):1–13, 1949.
- [99] Alain Karma. Electrical alternans and spiral wave breakup in cardiac tissue. *Chaos: An Interdisciplinary Journal of Nonlinear Science*, 4(3):461–472, 1994.
- [100] Richa Karmakar, Aravind Rao Karanam, Man-Ho Tang, and Wouter-Jan Rappel. Eukaryotic chemotaxis under periodic stimulation shows temporal gradient dependence. *bioRxiv*, pages 2023–10, 2023.
- [101] Richa Karmakar, Man-Ho Tang, Haicen Yue, Daniel Lombardo, Aravind Karanam, Brian A Camley, Alex Groisman, and Wouter-Jan Rappel. Cellular memory in eukaryotic chemotaxis depends on the background chemoattractant concentration. *Physical Review E*, 103(1):012402, 2021.

- [102] Richa Karmakar, Timothy J Tyree, Richard H Gomer, and Wouter-Jan Rappel. Cell dispersal by localized degradation of a chemoattractant. *Proceedings of the National Academy of Sciences*, 118(6):e2008126118, 2021.
- [103] Kyogo Kawaguchi, Ryoichiro Kageyama, and Masaki Sano. Topological defects control collective dynamics in neural progenitor cell cultures. *Nature*, 545(7654):327–331, 2017.
- [104] Kento Kawasaka, Takashi Hotta, and Masanori Kohda. Does a cichlid fish process face holistically? evidence of the face inversion effect. *Animal Cognition*, 22:153–162, 2019.
- [105] Guolin Ke, Qi Meng, Thomas Finley, Taifeng Wang, Wei Chen, Weidong Ma, Qiwei Ye, and Tie-Yan Liu. Lightgbm: A highly efficient gradient boosting decision tree. *Advances in neural information processing systems*, 30, 2017.
- [106] Keith M Kendrick, Khia Atkins, Michael R Hinton, Paul Heavens, and Barry Keverne. Are faces special for sheep? evidence from facial and object discrimination learning tests showing effects of inversion and social familiarity. *Behavioural processes*, 38(1):19–35, 1996.
- [107] Richard H Kessin. *Dictyostelium: evolution, cell biology, and the development of multicellularity*, volume 38. Cambridge University Press, 2001.
- [108] J. Kockelkoren, H. Levine, and W. J. Rappel. Computational approach for modeling intra- and extracellular dynamics. *Phys Rev E*, 68(3):037702, 2003.
- [109] Noriko Kondo, Ei-Ichi Izawa, and Shigeru Watanabe. Crows cross-modally recognize group members but not non-group members. *Proceedings of the Royal Society B: Biological Sciences*, 279(1735):1937–1942, 2012.
- [110] Till Kroeger, Radu Timofte, Dengxin Dai, and Luc Van Gool. Fast optical flow using dense inverse search. In *European Conference on Computer Vision*, pages 471–488. Springer, 2016.
- [111] Ashok Kumar, Jesus Zamora-Pineda, Emilie Degagné, Julie D Saba, et al. S1p lyase regulation of thymic egress and oncogenic inflammatory signaling. *Mediators of Inflammation*, 2017, 2017.
- [112] Dharshan Kumaran and Eleanor A Maguire. Match–mismatch processes underlie human hippocampal responses to associative novelty. *Journal of Neuroscience*, 27(32):8517–8524, 2007.
- [113] Tim Lämmermann, Philippe V Afonso, Bastian R Angermann, Ji Ming Wang, Wolfgang Kastentmüller, Carole A Parent, and Ronald N Germain. Neutrophil swarms require LTB4 and integrins at sites of cell death in vivo. *Nature*, 498(7454):371–375, 2013.
- [114] Jessica Frances Lampe and Jeffrey Andre. Cross-modal recognition of human individuals in domestic horses (*equus caballus*). *Animal cognition*, 15:623–630, 2012.

- [115] Sofia M Landi, Pooja Viswanathan, Stephen Serene, and Winrich A Freiwald. A fast link between face perception and memory in the temporal pole. *Science*, 373(6554):581–585, 2021.
- [116] Deirdre A Lane, Flemming Skjøth, Gregory YH Lip, Torben B Larsen, and Dipak Kotecha. Temporal trends in incidence, prevalence, and mortality of atrial fibrillation in primary care. *Journal of the American Heart Association*, 6(5):e005155, 2017.
- [117] Herbert Levine and Wouter-Jan Rappel. Membrane-bound Turing patterns. *Physical Review E*, 72(6):061912, 2005.
- [118] Teng-Chao Li, Wei Zhong, Bao-quan Ai, Alexander V Panfilov, and Hans Dierckx. Control of the chirality of spiral waves and recreation of spatial excitation patterns through optogenetics. *Physical Review E*, 105(1):014214, 2022.
- [119] Thomas Lilienkamp and Ulrich Parlitz. Terminal transient phase of chaotic transients. *Physical review letters*, 120(9):094101, 2018.
- [120] Thomas Lilienkamp and Ulrich Parlitz. Terminating transient chaos in spatially extended systems. *Chaos: An Interdisciplinary Journal of Nonlinear Science*, 30(5):051108, 2020.
- [121] Lance A Liotta. Cancer cell invasion and metastasis. *Scientific American*, 266(2):54–63, 1992.
- [122] John E Lisman. Relating hippocampal circuitry to function: recall of memory sequences by reciprocal dentate–ca3 interactions. *Neuron*, 22(2):233–242, 1999.
- [123] Chun Liu, Jie Shen, and Xiaofeng Yang. Dynamics of defect motion in nematic liquid crystal flow: modeling and numerical simulation. *Commun. Comput. Phys*, 2:1184–1198, 2007.
- [124] Massimo Locati, Yeny Martinez De La Torre, Emanuela Galliera, Raffaella Bonocchi, Haribabu Bodduluri, Gianluca Vago, Annunciata Vecchi, and Alberto Mantovani. Silent chemoattractant receptors: D6 as a decoy and scavenger receptor for inflammatory CC chemokines. *Cytokine & growth factor reviews*, 16(6):679–686, 2005.
- [125] Daniel M Lombardo and Wouter-Jan Rappel. Chaotic tip trajectories of a single spiral wave in the presence of heterogeneities. *Physical Review E*, 99(6):062409, 2019.
- [126] William Loomis. *The development of Dictyostelium discoideum*. Elsevier, 2012.
- [127] C. H. Luo and Y. Rudy. A model of the ventricular cardiac action potential. Depolarization, repolarization, and their interaction. *Circ Res*, 68:1501–1526, 1991.
- [128] Rupamanjari Majumder, Iolanda Feola, Alexander S Teplenin, Antoine AF de Vries, Alexander V Panfilov, and Daniel A Pijnappels. Optogenetics enables real-time spatiotemporal control over spiral wave dynamics in an excitable cardiac system. *Elife*, 7:e41076, 2018.

- [129] Janet Mann. *Cetacean societies: field studies of dolphins and whales*. University of Chicago Press, 2000.
- [130] M Cristina Marchetti, Jean-François Joanny, Sriram Ramaswamy, Tanniemola B Liverpool, Jacques Prost, Madan Rao, and R Aditi Simha. Hydrodynamics of soft active matter. *Reviews of modern physics*, 85(3):1143, 2013.
- [131] Jean-Louis Martiel and Albert Goldbeter. A model based on receptor desensitization for cyclic AMP signaling in Dictyostelium cells. *Biophysical journal*, 52(5):807–828, 1987.
- [132] Noritaka Masaki, Koichi Fujimoto, Mai Honda-Kitahara, Emi Hada, and Satoshi Sawai. Robustness of self-organizing chemoattractant field arising from precise pulse induction of its breakdown enzyme: A single-cell level analysis of pde expression in Dictyostelium. *Biophysical journal*, 104(5):1191–1202, 2013.
- [133] Leland McInnes, John Healy, and James Melville. Umap: Uniform manifold approximation and projection for dimension reduction. *arXiv preprint arXiv:1802.03426*, 2018.
- [134] N David Mermin. The topological theory of defects in ordered media. *Reviews of Modern Physics*, 51(3):591, 1979.
- [135] Cory T Miller, Winrich A Freiwald, David A Leopold, Jude F Mitchell, Afonso C Silva, and Xiaoqin Wang. Marmosets: a neuroscientific model of human social behavior. *Neuron*, 90(2):219–233, 2016.
- [136] Cory T Miller, David Gire, Kim Hoke, Alexander C Huk, Darcy Kelley, David A Leopold, Matthew C Smear, Frederic Theunissen, Michael Yartsev, and Cristopher M Niell. Natural behavior is the language of the brain. *Current Biology*, 32(10):R482–R493, 2022.
- [137] Cory T Miller and A Wren Thomas. Individual recognition during bouts of antiphonal calling in common marmosets. *Journal of Comparative Physiology A*, 198:337–346, 2012.
- [138] Juri Minxha, Clayton Mosher, Jeremiah K Morrow, Adam N Mamelak, Ralph Adolphs, Katalin M Gothard, and Ueli Rutishauser. Fixations gate species-specific responses to free viewing of faces in the human and macaque amygdala. *Cell reports*, 18(4):878–891, 2017.
- [139] Jude F Mitchell, John H Reynolds, and Cory T Miller. Active vision in marmosets: a model system for visual neuroscience. *Journal of Neuroscience*, 34(4):1183–1194, 2014.
- [140] Yoko Miyasaka, Marion E Barnes, Kent R Bailey, Stephen S Cha, Bernard J Gersh, James B Seward, and Teresa SM Tsang. Mortality trends in patients diagnosed with first atrial fibrillation: a 21-year community-based study. *Journal of the American College of Cardiology*, 49(9):986–992, 2007.
- [141] Denise J Montell. Border-cell migration: the race is on. *Nature Reviews Molecular Cell Biology*, 4(1):13–24, 2003.

- [142] Andrew J Muinonen-Martin, Olivia Susanto, Qifeng Zhang, Elizabeth Smethurst, William J Faller, Douwe M Veltman, Gabriela Kalna, Colin Lindsay, Dorothy C Bennett, Owen J Sansom, et al. Melanoma cells break down LPA to establish local gradients that drive chemotactic dispersal. *PLoS Biol*, 12(10):e1001966, 2014.
- [143] Jérôme Munuera, Mattia Rigotti, and C Daniel Salzman. Shared neural coding for social hierarchy and reward value in primate amygdala. *Nature neuroscience*, 21(3):415–423, 2018.
- [144] G. V. Naccarelli, H. Varker, J. Lin, and K. L. Schulman. Increasing prevalence of atrial fibrillation and flutter in the United States. *Am. J. Cardiol.*, 104(11):1534–1539, 2009.
- [145] Akihiko Nakajima, Shuji Ishihara, Daisuke Imoto, and Satoshi Sawai. Rectified directional sensing in long-range cell migration. *Nature communications*, 5:5367, 2014.
- [146] M. Newman. *Networks; an introduction*. Oxford University, Oxford, 2010.
- [147] Edward H Nieh, Manuel Schottdorf, Nicolas W Freeman, Ryan J Low, Sam Lewallen, Sue Ann Koay, Lucas Pinto, Jeffrey L Gauthier, Carlos D Brody, and David W Tank. Geometry of abstract learned knowledge in the hippocampus. *Nature*, 595(7865):80–84, 2021.
- [148] Haruki Odaka, Satoshi Arai, Takafumi Inoue, and Tetsuya Kitaguchi. Genetically-encoded yellow fluorescent cAMP indicator with an expanded dynamic range for dual-color imaging. *PloS one*, 9(6):e100252, 2014.
- [149] Yusaku Ohta, Toshiaki Furuta, Takeharu Nagai, and Kazuki Horikawa. Red fluorescent cAMP indicator with increased affinity and expanded dynamic range. *Scientific reports*, 8(1):1866, 2018.
- [150] Hakan Oral, Bradley P Knight, Hiroshi Tada, Mehmet Ozaydin, Aman Chugh, Sohail Hassan, Christoph Scharf, Steve WK Lai, Radmira Greenstein, Frank Pelosi Jr, et al. Pulmonary vein isolation for paroxysmal and persistent atrial fibrillation. *Circulation*, 105(9):1077–1081, 2002.
- [151] Tim Otto and Howard Eichenbaum. Neuronal activity in the hippocampus during delayed non-match to sample performance in rats: Evidence for hippocampal processing in recognition memory. *Hippocampus*, 2(3):323–334, 1992.
- [152] Q Ouyang and J-M Flesselles. Transition from spirals to defect turbulence driven by a convective instability. *Nature*, 379(6561):143, 1996.
- [153] Eiríkur Pálsson. A cAMP signaling model explains the benefit of maintaining two forms of phosphodiesterase in *Dictyostelium*. *Biophysical journal*, 97(9):2388–2398, 2009.
- [154] Pauline Pan, Ellen M Hall, and JT Bonner. Determination of the active portion of the folic acid molecule in cellular slime mold chemotaxis. *Journal of bacteriology*, 122(1):185–191, 1975.

- [155] Rajita Pappu, Susan R Schwab, Ivo Cornelissen, João P Pereira, Jean B Regard, Ying Xu, Eric Camerer, Yao-Wu Zheng, Yong Huang, Jason G Cyster, et al. Promotion of lymphocyte egress into blood and lymph by distinct sources of sphingosine-1-phosphate. *Science*, 316(5822):295–298, 2007.
- [156] Catherine Perrodin, Christoph Kayser, Nikos K Logothetis, and Christopher I Petkov. Voice cells in the primate temporal lobe. *Current Biology*, 21(16):1408–1415, 2011.
- [157] Benjamin J Pitcher, Elodie F Briefer, Luigi Baciadonna, and Alan G McElligott. Cross-modal recognition of familiar conspecifics in goats. *Royal Society open science*, 4(2):160346, 2017.
- [158] Ruth Pordes, Don Petravick, Bill Kramer, Doug Olson, Miron Livny, Alain Roy, Paul Avery, Kent Blackburn, Torre Wenaus, Frank Würthwein, Ian Foster, Rob Gardner, Mike Wilde, Alan Blatecky, John McGee, and Rob Quick. The open science grid. In *J. Phys. Conf. Ser.*, volume 78 of 78, page 012057, 2007.
- [159] Janet E Price. Metastasis from human breast cancer cell lines. *Breast cancer research and treatment*, 39:93–102, 1996.
- [160] Leanne Proops and Karen McComb. Cross-modal individual recognition in domestic horses (*equus caballus*) extends to familiar humans. *Proceedings of the Royal Society B: Biological Sciences*, 279(1741):3131–3138, 2012.
- [161] Leanne Proops, Karen McComb, and David Reby. Cross-modal individual recognition in domestic horses (*equus caballus*). *Proceedings of the National Academy of Sciences*, 106(3):947–951, 2009.
- [162] Krishna Pundi, Tina Baykaner, Mellanie True Hills, Bryant Lin, Daniel P Morin, Samuel F Sears, Paul J Wang, and Randall S Stafford. Blood thinners for atrial fibrillation stroke prevention. *Circulation: Arrhythmia and Electrophysiology*, 14(6):e009389, 2021.
- [163] Hong Qian, Michael P Sheetz, and Elliot L Elson. Single particle tracking. analysis of diffusion and flow in two-dimensional systems. *Biophysical journal*, 60(4):910–921, 1991.
- [164] Zhilin Qu. Critical mass hypothesis revisited: role of dynamical wave stability in spontaneous termination of cardiac fibrillation. *American Journal of Physiology-Heart and Circulatory Physiology*, 290(1):H255–H263, 2006.
- [165] Zhilin Qu, Alan Garfinkel, Peng-Sheng Chen, and James N Weiss. Mechanisms of discordant alternans and induction of reentry in simulated cardiac tissue. *Circulation*, 102(14):1664–1670, 2000.
- [166] Zhilin Qu, James N Weiss, and Alan Garfinkel. From local to global spatiotemporal chaos in a cardiac tissue model. *Physical Review E*, 61(1):727, 2000.

- [167] Angelo Quaranta, Serenella d’Ingeo, Rosaria Amoruso, and Marcello Siniscalchi. Emotion recognition in cats. *Animals*, 10(7):1107, 2020.
- [168] Rodrigo Quian Quiroga. An integrative view of human hippocampal function: Differences with other species and capacity considerations. *Hippocampus*, 2023.
- [169] R Quian Quiroga, Leila Reddy, Gabriel Kreiman, Christof Koch, and Itzhak Fried. Invariant visual representation by single neurons in the human brain. *Nature*, 435(7045):1102–1107, 2005.
- [170] Rodrigo Quian Quiroga. Concept cells: the building blocks of declarative memory functions. *Nature Reviews Neuroscience*, 13(8):587–597, 2012.
- [171] Rodrigo Quian Quiroga, Alexander Kraskov, Christof Koch, and Itzhak Fried. Explicit encoding of multimodal percepts by single neurons in the human brain. *Current Biology*, 19(15):1308–1313, 2009.
- [172] Anaïs Racca, Eleonora Amadei, Séverine Ligout, Kun Guo, Kerstin Meints, and Daniel Mills. Discrimination of human and dog faces and inversion responses in domestic dogs (*canis familiaris*). *Animal cognition*, 13:525–533, 2010.
- [173] Sriram Ramaswamy. The mechanics and statistics of active matter. *Annu. Rev. Condens. Matter Phys.*, 1(1):323–345, 2010.
- [174] Wouter-Jan Rappel. The physics of heart rhythm disorders. *Physics Reports*, 978:1–45, 2022.
- [175] Wouter-Jan Rappel, David Edward Krummen, Tina Baykaner, Junaid Zaman, Alan Donsky, Vijay Swarup, John M Miller, and Sanjiv M Narayan. Stochastic termination of spiral wave dynamics in cardiac tissue. *Frontiers in Network Physiology*, page 2, 2022.
- [176] Thomas P Reber, Marcel Bausch, Sina Mackay, Jan Boström, Christian E Elger, and Florian Mormann. Representation of abstract semantic knowledge in populations of human single neurons in the medial temporal lobe. *PLoS Biology*, 17(6):e3000290, 2019.
- [177] Ingo Rehberg, Steffen Rasenat, and Victor Steinberg. Traveling waves and defect-initiated turbulence in electroconvecting nematics. *Physical Review Letters*, 62(7):756, 1989.
- [178] Anne J Ridley, Martin A Schwartz, Keith Burridge, Richard A Firtel, Mark H Ginsberg, Gary Borisy, J Thomas Parsons, and Alan Rick Horwitz. Cell migration: integrating signals from front to back. *Science*, 302(5651):1704–1709, 2003.
- [179] Mattia Rigotti, Omri Barak, Melissa R Warden, Xiao-Jing Wang, Nathaniel D Daw, Earl K Miller, and Stefano Fusi. The importance of mixed selectivity in complex cognitive tasks. *Nature*, 497(7451):585–590, 2013.
- [180] AC Roberts and JD Wallis. Inhibitory control and affective processing in the prefrontal cortex: neuropsychological studies in the common marmoset. *Cerebral cortex*, 10(3):252–262, 2000.

- [181] Angela C Roberts, Maria Antonietta De Salvia, Lawrence Stephen Wilkinson, P Collins, JL Muir, BJ Everitt, and TW Robbins. 6-hydroxydopamine lesions of the prefrontal cortex in monkeys enhance performance on an analog of the wisconsin card sort test: possible interactions with subcortical dopamine. *Journal of Neuroscience*, 14(5):2531–2544, 1994.
- [182] Maimon C Rose, Boaz Styr, Tobias A Schmid, Julie E Elie, and Michael M Yartsev. Cortical representation of group social communication in bats. *Science*, 374(6566):eaba9584, 2021.
- [183] Steven T Rutherford and Bonnie L Bassler. Bacterial quorum sensing: its role in virulence and possibilities for its control. *Cold Spring Harbor perspectives in medicine*, 2(11):a012427, 2012.
- [184] Ueli Rutishauser, Oana Tudusciuc, Dirk Neumann, Adam N Mamelak, A Christopher Heller, Ian B Ross, Linda Philpott, William W Sutherling, and Ralph Adolphs. Single-unit responses selective for whole faces in the human amygdala. *Current Biology*, 21(19):1654–1660, 2011.
- [185] Atsuko Saito. The marmoset as a model for the study of primate parental behavior. *Neuroscience Research*, 93:99–109, 2015.
- [186] Atsuko Saito and Kazutaka Shinozuka. Vocal recognition of owners by domestic cats (*felis catus*). *Animal cognition*, 16:685–690, 2013.
- [187] Tim Sanchez, Daniel TN Chen, Stephen J DeCamp, Michael Heymann, and Zvonimir Dogic. Spontaneous motion in hierarchically assembled active matter. *Nature*, 491(7424):431–434, 2012.
- [188] Hanno Schar. Optimale operatoren in der digitalen bildverarbeitung. *PhD Thesis*, 2000.
- [189] RM Seyfarth and DL Cheney. The evolution of primate societies. pages 629–642, 2012.
- [190] Thomas N Seyfried and Leanne C Huysentruyt. On the origin of cancer metastasis. *Critical Reviews™ in Oncogenesis*, 18(1-2), 2013.
- [191] Igor Sfiligoi, Daniel C Bradley, Burt Holzman, Parag Mhashilkar, Sanjay Padhi, and Frank Würthwein. The pilot way to grid resources using glideinwms. In *2009 WRI World Congress on Computer Science and Information Engineering*, volume 2 of 2, pages 428–432, 2009.
- [192] Monica Skoge, Haicen Yue, Michael Erickstad, Albert Bae, Herbert Levine, Alex Groisman, William F Loomis, and Wouter-Jan Rappel. Cellular memory in eukaryotic chemotaxis. *Proceedings of the National Academy of Sciences*, 111(40):14448–14453, 2014.
- [193] Julia Sliwa, Jean-René Duhamel, Olivier Pascalis, and Sylvia Wirth. Spontaneous voice-face identity matching by rhesus monkeys for familiar conspecifics and humans. *Proceedings of the National Academy of Sciences*, 108(4):1735–1740, 2011.

- [194] Julia Sliwa, Aurélie Planté, Jean-René Duhamel, and Sylvia Wirth. Independent neuronal representation of facial and vocal identity in the monkey hippocampus and inferotemporal cortex. *Cerebral cortex*, 26(3):950–966, 2016.
- [195] Loling Song, Sharvari M Nadkarni, Hendrik U Bödeker, Carsten Beta, Albert Bae, Carl Franck, Wouter-Jan Rappel, William F Loomis, and Eberhard Bodenschatz. Dictyostelium discoideum chemotaxis: threshold for directed motion. *European journal of cell biology*, 85(9-10):981–989, 2006.
- [196] Hallan Souza-e Silva, Wilson Savino, Raúl A Feijóo, and Ana Tereza Ribeiro Vasconcelos. A cellular automata-based mathematical model for thymocyte development. *PLoS One*, 4(12):e8233, 2009.
- [197] Richard Suggang, Cornelis J Weijer, Florian Siegert, Jakob Franke, and Richard H Kessin. Null mutations of the Dictyostelium cyclic nucleotide phosphodiesterase gene block chemotactic cell movement in developing aggregates. *Developmental biology*, 192(1):181–192, 1997.
- [198] Olivia Susanto, Yvette WH Koh, Nick Morrice, Sergey Tumanov, Peter A Thomason, Matthew Nielson, Luke Tweedy, Andrew J Muinonen-Martin, Jurre J Kamphorst, Gillian M Mackay, et al. LPP3 mediates self-generation of chemotactic LPA gradients by melanoma cells. *J Cell Sci*, 130(20):3455–3466, 2017.
- [199] Maurice Sussman. Cultivation and synchronous morphogenesis of Dictyostelium under controlled experimental conditions. In *Methods in cell biology*, volume 28, pages 9–29. Elsevier, 1987.
- [200] Kristen F Swaney, Chuan-Hsiang Huang, and Peter N Devreotes. Eukaryotic chemotaxis: a network of signaling pathways controls motility, directional sensing, and polarity. *Annual review of biophysics*, 39:265–289, 2010.
- [201] Saho Takagi, Minori Arahori, Hitomi Chijiwa, Atsuko Saito, Hika Kuroshima, and Kazuo Fujita. Cats match voice and face: cross-modal representation of humans in cats (*felis catus*). *Animal cognition*, 22:901–906, 2019.
- [202] KHWJ Ten Tusscher, D Noble, PJ Noble, and AV Panfilov. A model for human ventricular tissue. *American Journal of Physiology-Heart and Circulatory Physiology*, 286(4):H1573–H1589, 2004.
- [203] KJ Tomchik and Peter N Devreotes. Adenosine 3', 5'-monophosphate waves in Dictyostelium discoideum: a demonstration by isotope dilution–fluorography. *Science*, 212(4493):443–446, 1981.
- [204] Doris Y. Tsao and Margaret S. Livingstone. Mechanisms of face perception. *Annual Review of Neuroscience*, 31(1):411–437, 2008.

- [205] Luke Tweedy, David A Knecht, Gillian M Mackay, and Robert H Insall. Self-generated chemoattractant gradients: attractant depletion extends the range and robustness of chemotaxis. *PLoS biology*, 14(3), 2016.
- [206] Luke Tweedy, Peter A Thomason, Peggy I Paschke, Kirsty Martin, Laura M Machesky, Michele Zagnoni, and Robert H Insall. Seeing around corners: Cells solve mazes and respond at a distance using attractant breakdown. *Science*, 369(6507), 2020.
- [207] Timothy J Tyree, Michael Metke, and Cory T Miller. Cross-modal representation of identity in the primate hippocampus. *Science*, 382(6669):417–423, 2023.
- [208] Elif Derya Übeyli. Recurrent neural networks employing lyapunov exponents for analysis of ecg signals. *Expert systems with applications*, 37(2):1192–1199, 2010.
- [209] Hamilton Varela, Carsten Beta, Antoine Bonnefont, and Katharina Krischer. Transitions to electrochemical turbulence. *Physical Review Letters*, 94(17):174104, 2005.
- [210] Gayatri Venkiteswaran, Stephen W Lewellis, John Wang, Eric Reynolds, Charles Nicholson, and Holger Knaut. Generation and dynamics of an endogenous, self-generated signaling gradient across a migrating tissue. *Cell*, 155(3):674–687, 2013.
- [211] Atul Verma, Chen-yang Jiang, Timothy R Betts, Jian Chen, Isabel Deisenhofer, Roberto Mantovan, Laurent Macle, Carlos A Morillo, Wilhelm Haverkamp, Rukshen Weerasooriya, et al. Approaches to catheter ablation for persistent atrial fibrillation. *New England Journal of Medicine*, 372(19):1812–1822, 2015.
- [212] David Vidmar and Wouter-Jan Rappel. Extinction dynamics of spiral defect chaos. *Physical Review E*, 99(1):012407, 2019.
- [213] Indre V Viskontas, Rodrigo Quian Quiroga, and Itzhak Fried. Human medial temporal lobe neurons respond preferentially to personally relevant images. *Proceedings of the National Academy of Sciences*, 106(50):21329–21334, 2009.
- [214] Bernhard Voelkl and Ludwig Huber. True imitation in marmosets. *Animal Behaviour*, 60(2):195–202, 2000.
- [215] Dmitri Volfson, Scott Cookson, Jeff Hasty, and Lev S Tsimring. Biomechanical ordering of dense cell populations. *Proceedings of the National Academy of Sciences*, 105(40):15346–15351, 2008.
- [216] Xiaoqin Wang, Thomas Lu, Ross K Snider, and Li Liang. Sustained firing in auditory cortex evoked by preferred stimuli. *Nature*, 435(7040):341–346, 2005.
- [217] Ashley JW Ward, Maud IA Kent, and Michael M Webster. Social recognition and social attraction in group-living fishes. *Frontiers in Ecology and Evolution*, 8:15, 2020.
- [218] Jen Wathan, Leanne Proops, Kate Grounds, and Karen McComb. Horses discriminate between facial expressions of conspecifics. *Scientific reports*, 6(1):38322, 2016.

- [219] Michael A Weinreich and Kristin A Hogquist. Thymic emigration: when and how t cells leave home. *The journal of immunology*, 181(4):2265–2270, 2008.
- [220] G Wittemyer and Wayne M Getz. Hierarchical dominance structure and social organization in african elephants, *loxodonta africana*. *Animal Behaviour*, 73(4):671–681, 2007.
- [221] Galit Yovel and Winrich A Freiwald. Face recognition systems in monkey and human: are they the same thing? *F1000prime reports*, 5, 2013.
- [222] Andrei Zala, Dan Dimitriu, Maricel Agop, Dan N Tesloianu, Maria L Cobzeanu, Bogdan M Cobzeanu, Marcela C Rusu, and Vlad Ghizdovat. Evaluating atrial fibrillations through strange attractors dynamics. *General Physiology & Biophysics*, 40(5), 2021.
- [223] Rui Zhang, Nitin Kumar, Jennifer L Ross, Margaret L Gardel, and Juan J De Pablo. Interplay of structure, elasticity, and dynamics in actin-based nematic materials. *Proceedings of the National Academy of Sciences*, 115(2):E124–E133, 2018.